ATMIRE

Title	Design and fabrication of asymmetric nanopores using pulsed PECVD
Item Type	Text
Authors	Kelkar, Sanket S.
Publisher	Colorado School of Mines. Arthur Lakes Library
Rights	Copyright of the original work is retained by the author.
Download date	2026-11-28 07:18:05
Link to Item	https://hdl.handle.net/11124/20173

DESIGN AND FABRICATION OF ASYMMETRIC NANOPORES USING PULSED PECVD

by

Sanket S. Kelkar

A thesis submitted to the Faculty and the Board of Trustees of the Colorado School of Mines in partial fulfillment of the requirements for the degree of Doctor of Philosophy (Chemical and Biological Engineering).

Golden, Colorado

Date: _____ Signed: _____

Sanket S. Kelkar

Approved: _____

Dr. Colin A. Wolden

Thesis Advisor

Golden, Colorado

Date: _____ _____

Dr. David Marr

Professor and Head

Department of Chemical and Biological Engineering

Colorado School of Mines

ABSTRACT

Manipulating matter at nanometric length scales is important for many electronic, chemical and biological applications. Structures such as nanopores demonstrate a phenomenon known as hindered transport which can be exploited in analytical applications such as DNA sequencing, ionic transistors, and molecular sieving. Precisely controlling the size, geometry and surface characteristics of the nanopores is important for realizing these applications. In this work, we employ relatively large template structures (~ 100 nm) produced by track-etching or electron beam lithography. The pore size is then reduced to the desired level by deposition of material using pulsed plasma enhanced chemical vapor deposition (PECVD). Pulsed PECVD has been developed as a high throughput alternative to atomic layer deposition (ALD) to deliver self-limiting growth of thin films. The goal of this thesis is to extend the application of pulsed PECVD to fabricate asymmetric nanopores.

In contrast to ALD, pulsed PECVD does not result in perfectly conformal deposition profiles, and predicting the final nanostructure is more complicated. A two dimensional feature scale model was developed to predict film profile evolution. The model was built in COMSOL, and is based on a diffusion reaction framework with a spatially varying Knudsen diffusion coefficient to account for the molecular transport inside the features. A scaling analysis was used to account for ALD exposure limitations that commonly occur when coating these extremely high aspect ratio features. The model was verified by cross-section microscopy of deposition profiles on patterned cylinders and trenches. The model shows that it is possible to obtain unique nanopore morphologies in pulsed PECVD that are distinct from either steady state deposition processes such as physical vapor deposition (PVD) or conventional ALD.

Polymeric track etched (TE) membrane supports with a nominal size of 100 nm were employed as model template structures to demonstrate the capability of pulsed PECVD for precise pore size reduction of model supports. The efficacy of pulsed PECVD for nanopore fabrication was compared to both ALD and PVD. Flux and solute rejection measurements demonstrate that the pulsed PECVD-modified TE membranes exhibit higher selectivity without compromising on the flux due to their asymmetric structure. For example, the TiO_2 modified supports were demonstrated to deliver high retention (~ 75%) of bovine serum albumin (BSA) protein while maintaining 70% of their initial pure water flux. PVD also forms asymmetric membranes that enable high flux. But due to morphological instabilities, reproducibility and control were poor in the PVD-modified membranes, and it was not possible to optimize the flux and the selectivity of the membranes simultaneously. Excellent agreement between measured flux and model predictions based on feature scale simulations provided further validation of the tool's fidelity.

Since surface energetics can often dominate hindered transport, the kinetics and thermodynamics of the octadecyltrichlorosilane (OTS) attachment was investigated in-depth as an approach to convert hydrophilic metal oxides into hydrophobic surfaces. It was shown that a simple ozone treatment was a satisfactory alternative to hazardous acids to create the highly hydroxylated surface required for OTS attachment, and that using heptane as the solvent enabled the process to be conducted under ambient conditions without the need of a glovebox. The kinetics of OTS self-assembled monolayer (SAM) formation and the saturation contact angle ($\sim 100^\circ$) on alumina are comparable to what has been observed for OTS attachment on silicon. The OTS SAMs also demonstrated excellent thermal stability, and the modified surface showed a critical surface tension of 21.4 dyne/cm.

TABLE OF CONTENTS

Abstract..... iii

List of Figures..... ix

List of Abbreviations and Symbols xiv

Acknowledgements xvi

Chapter 1. INTRODUCTION……..…….....1

1.1. Biological Nanopores.....2

1.2. Solid State Nanopores.....4

1.3. Template Strategy for Fabrication of Nanopores.....5

1.4. Pulsed PECVD: An Introduction.....9

1.5. Feature Scale Modeling of Nanopore Geometries.....12

1.6. Surface Functionalization of Nanopores.....15

1.7. Thesis Overview 16

Chapter 2. MODELING DETAILS……..…….....19

2.1. Feature Scale Modeling 19

2.1.1. Modeling of Steady State Deposition Processes.....20

2.1.2. Modeling of Unsteady State Pulsed PECVD Process 27

2.1.3. Modeling of Exposure-Limited ALD Case.....29

2.1.4. Model Validation 30

2.2. Modeling Flux of Nanoporous Membranes.....30

Chapter 3. EXPERIMENTAL DETAILS AND CHARACTERIZATION TECHNIQUES……..…….....32

3.1. Model Supports.....32

3.1.1. SOI Membrane Support 32

3.1.2. Track-etched Membrane Support 35

3.2. Pore Modification Techniques 36

3.2.1. Pulsed PECVD 36

3.2.2. Physical Vapor Deposition 38

3.2.3. Plasma-enhanced Atomic Layer Deposition 40

3.3. Membrane Testing and Characterization 41

3.3.1. Determination of Flux and Solute Rejection 41

3.3.2. Ellipsometry 42

3.3.3. Scanning Electron Microscopy 44

3.3.4. Contact Angle Measurement 45

Chapter 4. FEATURE SCALE MODELING OF STEADY STATE- AND TRANSIENT- DEPOSITION PROCESSES 47

4.1. Introduction 48

4.2. Modeling 51

4.2.1. Modeling of Steady State Processes 52

4.2.2. Modeling of Unsteady State Pulsed PECVD Process 57

4.3. Results and Discussion 59

4.4. Summary and Conclusions 68

4.5. Acknowledgements 69

Chapter 5. DESIGN AND FABRICATION OF ASYMMETRIC MEMBRANES FOR SIMULTANEOUS OPTIMIZATION OF FLUX AND SELECTIVITY 70

5.1. Introduction 71

5.2. Experimental 74

5.2.1. Materials 74

5.2.2. Membrane Fabrication 75

5.2.3. Membrane Characterization 76

5.3. Design and Analysis of Asymmetric Pores 77

5.4. Results and Discussion 81

5.5. Conclusions 89

5.6. Acknowledgements 89

Chapter 6. SURFACE FUNCTIONALIZATION OF AMORPHOUS ALUMINA SURFACES WITH OCTADECYLTRICHLOROSILANE SELF-ASSEMBLED MONOLAYERS 90

6.1. Introduction 91

6.2. Experimental Details 93

6.2.1. Materials 93

6.2.2. Deposition of Aluminum Oxide 93

6.2.3. Pretreatment of Substrates 93

6.2.4. Characterization of OTS SAM 94

6.3. Results and Discussion. 95

6.3.1. Preparation of Al_2O_3 Surfaces and their Stability 95

6.3.2. Kinetics of OTS attachment 97

6.3.3. Properties and Stability of OTS monolayers 102

6.4. Conclusions 104

6.5. Acknowledgements 104

Chapter 7. SUMMARY OF RESULTS AND RECOMMENDATIONS 105

7.1. Summary of Results 105

7.2. Recommendations for Future Work 108

7.2.1. Future Work: Investigation of Ion Transport through Asymmetric Nanopores 109

7.2.2. Future Work: Surface Functionalization of Nanopores.....111

REFERENCES 114

APPENDIX A: FABRICATION OF SILICON MODEL SUPPORTS.....125

APPENDIX B: MODELING OF STEADY STATE DEPOSITION PROCESSES.....130

APPENDIX C: HINDERED DIFFUSION STUDIES.....138

APPENDIX C: COPYRIGHT PERMISSIONS.....143

LIST OF FIGURES

Figure 1.1 (a) α-haemolysin protein (b) Differentiation of pyrimidine and purine bases by measuring ionic current fluctuations in a nanopore. Reprinted by permission from Macmillan Publishers Ltd: Nature Nanotechnology[8], copyright (2011)….2

Figure 1.2 (a) Apparatus employed for fabrication of nanopores using a feedback mechanism for precise control of pore size (b) A 61 nm prefabricated hole (c) 1.8 nm small nanopore formed by exposure to high energy ion beam. Figure 1.2 adapted by permission from Macmillan Publishers Ltd: Nature[1], copyright (2001). ……..…...5

Figure 1.3 (a) Pores ~ 70 nm in size fabricated by using electron beam lithography and reactive ion etching (b, c) TEM images of nanopores fabricated by controllably shrinking the model pores by ALD of TiO_2 after 1100 cycles. Adapted with permission from [6]. Copyright (2009) American Chemical Society..……....6

Figure 1.4 Representation of an ALD cycle. Reprinted by permission from John Wiley and Sons Publishers Ltd: Angewandte Chemie International Edition[21], copyright (2003)……..…7

Figure 1.5 (a) Gas flow and plasma sequence in PEALD (b) Gas flow and plasma sequence in pulsed PECVD. Reprinted with permission from [25]. Copyright (2008), American Vacuum Society…..…….....……10

Figure 1.6 Growth Mechanism in pulsed PECVD. Reprinted with permission from [25]. Copyright (2008), American Vacuum Society. …….....11

Figure 1.7 (a) Deposition profile in a perfectly conformal ALD process. (b) Deposition profile in pulsed PECVD (c) Deposition profile in a perfect sticking process like PVD.…….....14

Figure 2.1 Computational domain and governing boundary equations[23].…...……...….21

Figure 2.2 Deposition profiles as a function of ϕ. Deposited material is represented by white color, and the surrounding gas phase is represented by black color[23].....26

Figure 2.3 Modeling Scheme for pulsed PECVD[23]….…….... ……...28

Figure 2.4 ALD deposition profiles as a function of critical aspect ratio a*[23]…….....30

Figure 3.1 Model silicon supports comprise of active and window regions. The active region consists of an array of well-defined holes patterned using electron beam lithography and cryogenic etching. The window region is formed from the backside using KOH etch to create membrane..……..……...33

Figure 3.2 (a) Undercutting in the silicon layer due to inadequate passivation (b) Cracking of the active layer.……..……34

Figure 3.3 (a) Plan view SEM micrograph and (b) Cross-section image of a track-etched membrane support employed for pore modification study in this work…….…….....35

Figure 3.4 Schematic of the parallel plate capacitively coupled plasma (CCP) reactor employed for pulsed PECVD and PE-ALD depositions. Figure taken from [37].….……..….37

Figure 3.5 Schematic diagram of a resistive thermal evaporation system..…….....……..….39

Figure 3.6 PEALD growth rates as a function of precursor dose times...……....…….....….40

Figure 3.7 (a) Stirred ultrafiltration cell used for characterizing membrane flux and solute rejection (b) Absorbance plotted as a function of concentration of bovine serum albumin (BSA).....42

Figure 3.8 Typical ellipsometer configuration. Ellipsometer measures change in polarization of light to determine film thickness and optical properties. Figure adapted from J. A. Woollam Co [38].…….....43

Figure 3.9 Schematic of the contact angle measurement apparatus. Reprinted with permission from [39]. Copyright (2010) American Chemical Society. …...45

Figure 3.10 Liquid droplet on a (a) Surface cleaned with UV-Ozone treatment (b) Aluminum oxide surface coated with self-assembled monolayer (SAM) of octadecyltrichlorosilane (OTS).……46

Figure 4.1 Computational domain showing half of a cylindrical cross-section (Initial Radius = 50 nm, aspect ratio = 4) with governing equations and boundary conditions. Film growth occurs on the surface of the feature, highlighted in blue.…….... 52

Figure 4.2 Steady state profiles on a cylinder (Initial opening = 100 nm, aspect ratio = 4) simulated as a function of step coverage modulus (ϕ) for conditions characteristic of (a) ALD, ϕ = 0.022; (b) CVD, ϕ = 4.4; and(c) PVD, ϕ = 44.3...57

Figure 4.3 Block diagram of pulsed PECVD modeling approach. The model alternates between ALD and PVD modes till the desired planar thickness is achieved. '*R*' is the ratio of the two growth modes which is the adjustable parameter in the unsteady state pulsed PECVD model……...58

Figure 4.4 Comparison of pulsed PECVD profiles on a cylinder (Initial opening = 100 nm, aspect ratio = 4) as a function of PVD/ALD ratio for (a) *R* = 1; (b) *R*= 3; and (c) *R* = 5. '*R*' values employed for these simulations reflect the typical operating conditions in pulsed PECVD……60

Figure 4.5 Comparison of deposition profiles on a cylinder (Initial opening = 100 nm, aspect ratio = 4) obtained at *R* = 3 simulated using GPC values of 2.35 nm/pulse (left) and 4.7 nm/pulse (right). Model GPC values < 5 nm/pulse were found to be sufficiently small to significantly reduce the computation time without compromising on the integrity of the final deposition profile……60

Figure 4.6 Comparison of experimental (left) and simulated (right) profiles obtained from a cylindrical feature coated by pulsed PECVD of alumina under conditions where R = 1. The initial opening is around 125 nm and the height of the cylindrical feature is around 770 nm. Final pore opening ~ 10 nm is achieved by deposition of 80 nm aluminum oxide layer using PVD/ALD ratio of *R* =1. The left half of the simulated profile was obtained using the sufficient exposure assumption whereas the right half accounts for the exposure limitations present during the experiment. The two profiles are very similar with exception of the base of the feature. The black and red curves in the experimental SEM are provided to highlight the initial feature and the final deposition profile, respectively……..……..... 63

Figure 4.7 A plot of minimum reactant exposure required to conformally coat a feature as a function of aspect ratio. Horizontal lines indicate the experimental TMA exposure employed during the fabrication of the structures shown in Figures. 4.6 and 4.9, respectively.……..……... 65

Figure 4.8 Comparison of ALD profiles on a cylindrical feature (Initial opening = 100 nm, aspect ratio = 4) as a function of the critical aspect ratio (a^*). a^* is determined from the precursor exposure using scaling relationships developed by Gordon and coworkers. $a^* \to \infty$ case is a representation of the sufficient exposure assumption.…….. ……..…66

Figure 4.9 Comparison of experimental and simulated deposition profiles in a trench. The trench is 6 μm deep and shows a taper with top width ~ 700 nm and Bottom width ~ 450 nm. Aluminum oxide layer with a planar thickness of 240 nm was deposited during the filling process. The contributions of the PVD and ALD components were identical, and hence, PVD/ALD ratio of R =1 was employed during the simulation.…… ……...….....67

Figure 5.1 (a) Top view and (b) cross-section SEM micrographs of uncoated TE membrane supports...…….. ……75

Figure 5.2 (a) Top view SEM micrograph of nanopores fabricated using pulsed PECVD; (b) Cross-section SEM of a nanopore; (c) Model prediction of the nanopore geometry using the simulation procedure described in this work.……...…...78

Figure 5.3 Simulated deposition profiles on 100 nm features coated by (a) ALD, (b) pulsed PECVD, and (c) PVD for a final pore opening of 20 nm..……...….80

Figure 5.4 The left panel displays top view micrographs of TE membranes modified by PVD of aluminum (a-c), PEALD of TiO_2 (d-f), and pulsed PECVD of TiO_2 (g-i) as a function of planar film thickness. The right panel displays the corresponding feature scale simulation of the resulting geometries noting the minimum pore diameter for these 9 cases....……..……..……....82

Figure 5.5 Comparison of experimentally measured (points) and predicted flux (black lines) as a function of deposition thickness for TE membranes modified by (a) aluminum PVD, (b) PEALD of titania, and (c) pulsed PECVD of titania. The dashed red line is the prediction for perfectly conformal modification...…….....84

Figure 5.6 Solute rejection and predicted flux as a function of film thickness for (a) PVD-modified membranes; (b) PEALD-modified membranes and (c) Pulsed PECVD-modified membranes. Circled values indicate membranes that displayed the best combination of flux and selectivity for each technique as discussed in the text....…….....87

Figure 6.1 Photographs of water droplets used to quantify contact angles: (a) as-received aluminum oxide coated substrates; (b) Al_2O_3 after standard UV-Ozone treatment; (c) Al_2O_3 coated with an OTS monolayer.…….....….95

Figure 6.2 Evolution of water contact angle on alumina: (a) as a function of UV-Ozone exposure time; and (b) as a function of time after UV-ozone exposure. 96

Figure 6.3 Plot of water contact angle vs. immersion time for 3 different OTS concentrations…….....98

Figure 6.4 FTIR spectra of Al_2O_3 substrates as a function of immersion time in a 250 µM OTS solution.……. ……...98

Figure 6.5 Thickness of saturated monolayers as a function of OTS concentration……...99

Figure 6.6 The rate constants for adsorption (squares, left axis) and desorption (circles, right axis) as a function of OTS concentration……...……101

Figure 6.7 The Gibbs free energy of OTS SAMs as a function of OTS concentration…....101

Figure 6.8 Zisman plot obtained from saturated OTS SAMs on Al_2O_3……..…..102

Figure 6.9 The water contact angle on a saturated monolayer as a function of annealing temperature.…….……103

Figure 7.1 (a) Ion current rectification in an asymmetric nanopore (b) An asymmetric nanopore with a pore opening ~ 6 nm fabricated using pulsed PECVD. Figure 7.1 (a) adapted by permission from John Wiley and Sons Publishers Ltd: Advanced Functional Materials[5], copyright (2006)..…….....109

Figure 7.2 (a) Estimated electrostatic potential as a function of normalized pore length in a conical track-etched pore[5] and an asymmetric nanopore fabricated using pulsed PECVD…….....……..111

Figure A.1 Processes involved in fabrication of model supports in a SOI wafer……..126

Figure A.2 Etch profiles as a function of CCP power and oxygen flowrate. Best profile is obtained at conditions of high CCP power and oxygen flowrate.……....127

Figure A.3 Etch rate (nm/min) as a function of design aspect ratio. Etch rate decreases As the aspect ratio of the feature increases.…… ……...…...128

Figure A.4 Cross-section micrographs of etch profiles illustrating ARDE phenomenon.....129

Figure B.1 Feature boundaries highlighted in blue……134

Figure B.2 Initial mesh structure employed in the model.……..…...135

Figure B.3 Geometry employed in model 2. Pore1d is defined in this 1D domain, and is subsequently ‘extruded’ to the 2D model……..……..…136

Figure C.1 Schematic of diffusion cell.……..……..…….138

Figure C.2 Absorption spectra for various dye concentrations……..……141

Figure C.3 Plot of absorbance as a function of dye concentration.……..…….....…142

LIST OF ABBREVIATIONS AND SYMBOLS

Abbreviations

DNA	Deoxyribonucleic acid
PECVD	Plasma enhanced chemical vapor deposition
ALD	Atomic layer deposition
PE-ALD	Plasma enhanced atomic layer deposition
TMA	Trimethylaluminum
PVD	Physical vapor deposition
GPC	Growth per cycle
BTRM	Ballistic transport reaction model
DRM	Diffusion reaction model
OTS	Octadecyltrichlorosilane
SAM	Self-assembled monolayer
PEG	Polyethylene glycol
CVD	Chemical vapor deposition
TE	Track-etched
CCP	Capacitively coupled plasma
RF	Radio frequency
SEM	Scanning electron microscopy
BSA	Bovine serum albumin
ALE	Arbitrary lagrangian eularian
PWF	Pure water flux
FTIR	Fourier transform infrared

Symbols

γ	Sticking coefficient
R	Ratio of contribution of the PVD-like mode to the contribution of the ALD-like mode
C	Concentration of reactive species
pp	Partial pressure of the reactive species
C_0	Concentration of the reactive species at the top of computational domain
J	Flux of reactive species
D_B	Diffusion coefficient in the bulk domain
D_k	Knudsen diffusion coefficient
v_m	Mean molecular speed of gas molecules
R_s	Rate of heterogeneous surface reaction
V_M	Molar volume
v	Mesh extension velocity
ϕ	Step coverage modulus
a	Aspect ratio
a^*	Critical aspect ratio
ΔG_{ads}	Free energy of adsorption
θ	Fractional surface coverage
k_a	Adsorption rate constant
k_d	Desorption rate constant

ACKNOWLEDGEMENTS

PhD has been a long journey and it wouldn't be possible to complete it on my own. I would like to use this opportunity to acknowledge all the people who have contributed to this thesis.

My sincerest thanks to my advisor Professor Wolden for his constant guidance and immense patience with my (many) mistakes. Throughout my research I have been helped by many members of my research group. I would specially like to thank Sterling Parks for being a good friend and a microscopist par excellence. I would also like to thank David Chiavetta, Sirichat Rojnirun and Amanda Fankell for assisting me at different stages of my research. Also I am grateful to Christopher Lange for teaching me the joy in fixing (and occasionally breaking) equipment in the laboratory. I am also grateful to Dr Scott Retterer and Darrell Thomas of the Center for Nanophase Materials and Science at the Oak Ridge National Laboratory for training me on different nanofabrication tools and procedures.

I am eternally grateful to my parents for all their love, care and sacrifices. I owe all the successes in my life to them. Special thanks to my brother Pranav for always being the person I can look up to for advice and inspiration. I would also like to thank my friends Naveed and Zafar for being part of many spur of the moment road trips. I am thankful to my research group member Daniel Meysing for being a loyal tennis partner and hiking buddy for last 4 years. My thanks to all my friends especially Rohan, Aditya, Steven, Ali and Hani for their support.

Last but not the least I am grateful for the financial support by the National Science Foundation (NSF) through award CBET-1033203 during my research work.

CHAPTER 1

INTRODUCTION

Manipulating matter at the nanometric length scale is important for many electronic, chemical and biological applications[1-3]. Structures such as nanopores, with pore openings around 1-20 nm, have potential applications in DNA and RNA sequencing[4], ionic transistors[5, 6] and single molecule binding assays[7]. In particular, nanopores are expected to revolutionize human genome sequencing which is predicted to have an important role in personal medicine and therapeutics[8]. Central to all these nanopore-based applications is a phenomenon known as hindered transport. Due to constricted environment of the nanopore, transport of solutes such as proteins, DNA and RNA is considerably hindered since their size is comparable to the pore diameter. Moreover, in contrast to a bulk solution, surface interactions between solute and pore walls based on hydrophobicity[9], charge[10] and chirality[11] can dominate transport of these solutes inside nanopore channels. These phenomena can be exploited to enhance selectivity and to make single molecule detectors. For instance, one can use information like attenuation in ionic current inside the nanopore to detect and sequence an entire macromolecule[12].

Nanopores occur in nature[12, 13] and they can also be fabricated in laboratory[1, 2] using top-down or bottom-up approaches. A popular example of a naturally occurring nanopore is alpha-haemolysin protein pore found in staphylococcus aureus[12]. Although these biological nanopores occur in abundance in nature, they are characterized by very high degree of precision while maintaining near perfect repeatability of nanopore structure. Inspite of their many advantages, widespread use of biological nanopores for sequencing applications is limited because of their lack of stability in diverse experimental conditions. It is also difficult to integrate these nanopores in a nanofluidic device due to their limited mechanical stability. An effective

alternative for fabricating nanopores employs interaction of matter with high energy electron or ion beams[2, 3]. A feedback mechanism is employed to track the pore size continuously, and it is possible to terminate the beam as soon as the desired pore size is reached[14]. The expensive top-down approaches are usually employed to fabricate a single or a small array of nanopores in one batch[1, 2]. While useful for proof of concept experiments, problems like beam scattering, low throughput and high energy input are other factors which limit the applicability of this approach[6]. An alternative route for fabrication of nanopores is desired which can deliver high precision of top-down approaches without compromising the throughput and with a lower energy imprint.

1.1 Biological Nanopores

Biological nanopores embedded in a lipid bilayer offer many advantages for single molecule detection and identification. A biological nanopore called α-haemolysin (33 kDa) was

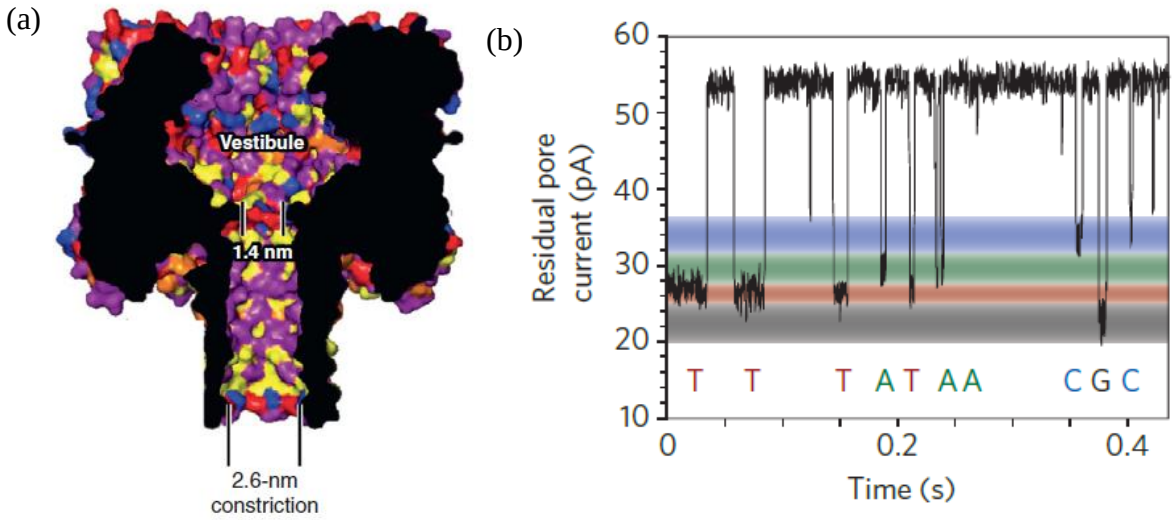


Figure 1.1: (a) α-haemolysin protein (b) Differentiation of pyrimidine and purine bases by measuring ionic current fluctuations in a nanopore. Reprinted by permission from Macmillan Publishers Ltd: Nature Nanotechnology[8], copyright (2011).

first isolated by Kasianowicz and coworkers from staphylococcus aureus bacteria[12]. Unlike many other biological nanopores, α-haemolysin pore allows a steady ionic current of 100 pA to flow through it under an applied voltage of 100 mV. Figure 1.1 (a) shows important structural features of this protein[8] which include the mouth of the channel with a pore opening ~ 2.6 nm, and a region called vestibule which has a much larger opening ~ 4.6 nm. This protein self-assembles in a lipid bilayer to form a channel with a relatively large pore. The narrowest dimension of this protein structure is 1.4 nm, and this opening allows only a single stranded DNA molecule to pass through it in a strictly linear fashion.

Macromolecules such as DNA and RNA move towards the nanopore under the influence of an applied electric field[12]. During their passage, the macromolecules block most of the channel, and this leads to rapid attenuation in the ionic current signal. This blockade event has two important components. First, the magnitude of the ionic current blockade can be used to decode information regarding the chemical nature of the macromolecule. As seen in Figure 1.1 (b), every base (A, T, C and G) causes a characteristic drop in the ionic current, and using this information it is possible to decode an entire DNA molecule. The second important piece of information is contained in the duration of the blockade event. The duration for which the ionic current is attenuated is directly proportional to length of the polymeric chain, and can be correlated to the molecular weight of the macromolecule.

This label-free approach for DNA sequencing offers many advantages. The alpha haemolysin protein nanopore does not have any moving parts, and thus a steady ionic current signal can be obtained inside a nanopore. Although these nanopores occur abundantly in the nature, the structure of the nanopore is remarkably same. Also, the nanopore does not exhibit any specific binding with macromolecules such as DNA and RNA, and hence clogging can be

avoided[15]. Lastly, the chemical structure of the nanopore can be manipulated by genetic mutation[16] to tailor the nanopore for different applications. Inspite of these advantages there are few limitations which limit the application of biological nanopores. For example, these nanopores are usually embedded in a lipid bilayer which renders the membrane mechanically fragile. Also it is very difficult to integrate these nanopores into nanofluidic devices because these nanopores are intrinsically unstable, and cannot tolerate any fluctuation in pH, temperature and ionic strength. A more robust nanopore is desired for research and clinical applications which can survive long periods of testing in different chemical and physiological environments.

1.2 Solid State Nanopores

High energy electron and ion beams have been commonly used to sculpt nanopores within a thin membrane[1, 14, 17]. These techniques are very precise as a feedback mechanism is employed to monitor the pore size continuously. Figure 1.2 (a) shows a schematic of the feedback-controlled ion beam sculpting apparatus developed by the Harvard Nanopore group[1, 14]. Fabrication of nanopores is done by bombarding the surface of a thin membrane with high energy argon (Ar) ions using a differentially pumped ion gun. There are two mechanisms which lead to the formation of nanopores. In one case, a pre-fabricated bowl-shaped cavity can be opened up to create a nano-sized hole. In another variation of this process seen in Figures 1.2 (b) and (c), a big hole can be shrunk in size to form a nanopore. This is due to filling up of the hole by surface transport of adatoms created during ion bombardment[1]. The final pore size is controlled by monitoring the ion flux passing unimpeded through the nanopore, and once the ion flux crosses the threshold, the ion beam sculpting process is halted.

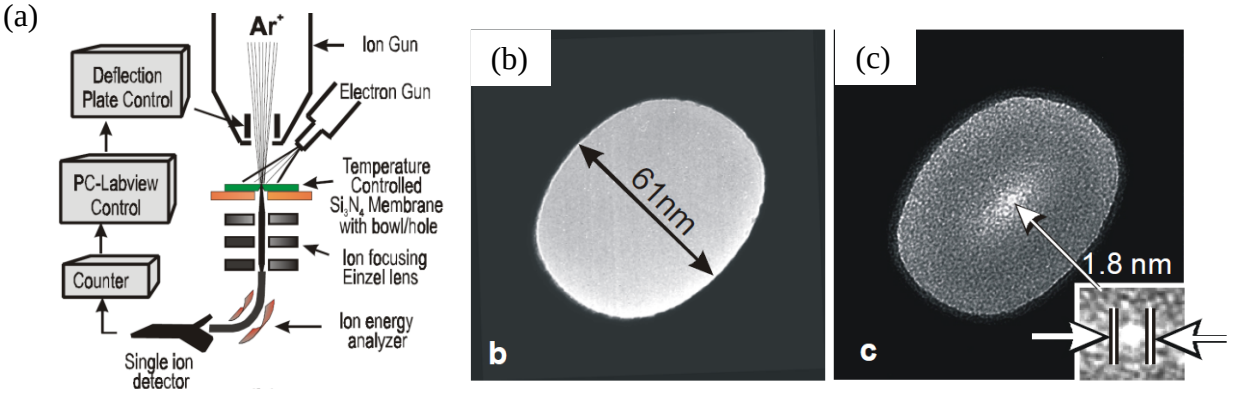


Figure 1.2: (a) Apparatus employed for fabrication of nanopores using a feedback mechanism for precise control of pore size (b) A 61 nm prefabricated hole (c) 1.8 nm small nanopore formed by exposure to high energy ion beam. Figure 1.2 adapted by permission from Macmillan Publishers Ltd: Nature[1], copyright (2001).

Dekker and coworkers have employed high energy electron beams instead of ion beams to implement a similar scheme for fabricating nanopores[17]. Even though both these fabrication methods are highly precise, they are not scalable as they are typically employed for fabricating a single or a small array of nanopores. Also, the control of the cross-sectional nanopore profile is still a problem due to insufficient understanding of beam-matter interaction at the nanoscale.

1.3 Template Strategy for Fabrication of Nanopores

In this work, we employ an alternative 2-step fabrication route proposed by Nam and coworkers[6]. The first step is fabrication of relatively large model supports with a pore opening ~ 100 nm. These holes can be fabricated in a silicon-based device by using photo- or electron beam- lithography to pattern the features followed by reactive ion etching to create uniform array of cylindrical features. Aspect ratio of these holes is typically around 10. Alternatively, track etching can be used to create ultra-high aspect ratio pores of desired size and shape in a polymeric film by bombarding it with heavy nuclei[18]. Next step in this fabrication process

involves using vapor deposition techniques like atomic layer deposition (ALD) to shrink the pore size to nanometric dimensions.

Figure 1.3 demonstrates the capability of this technique to fabricate molecular level pores[6]. In the first step, 70 nm holes were patterned using electron beam lithography and reactive ion etching. To reduce dimensions of the pore to the molecular level, the pores were

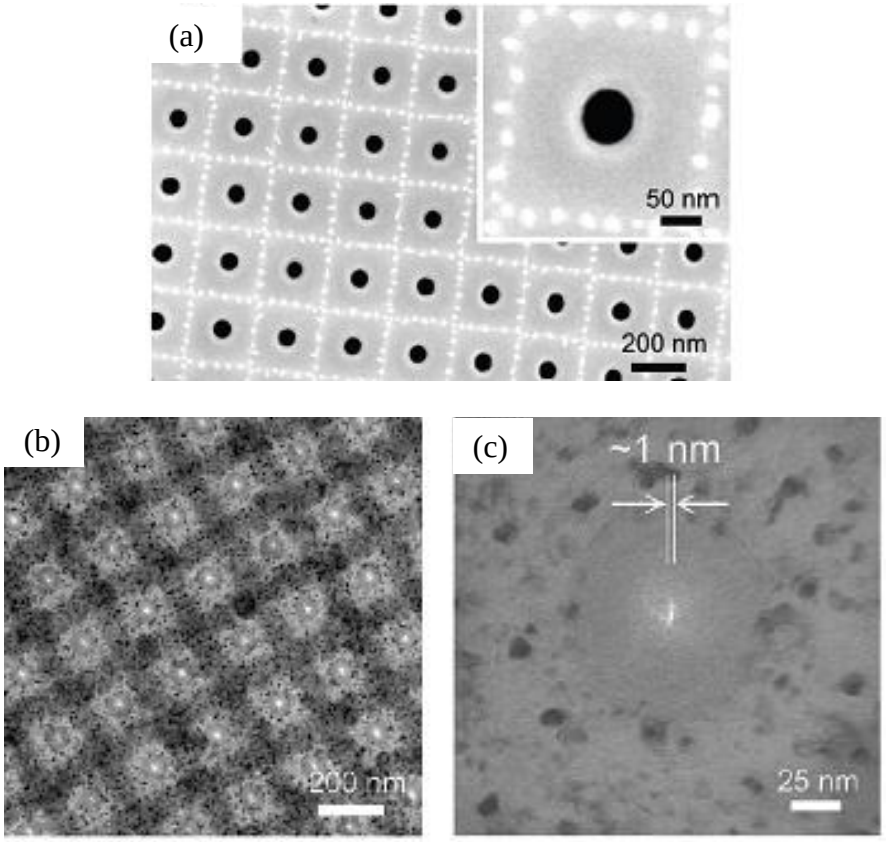


Figure 1.3: (a) Pores ~ 70 nm in size fabricated by using electron beam lithography and reactive ion etching (b, c) TEM images of nanopores fabricated by controllably shrinking the model pores by ALD of TiO_2 after 1100 cycles. Adapted with permission from [6]. Copyright (2009) American Chemical Society.

modified by ALD of titanium oxide (TiO_2). ALD is a self-limiting deposition technique, and can be used to deliver Angstrom (Å)-level control over thin film growth[19, 20]. It is possible to precisely tune the pore size to the desired level by simply changing the number of ALD cycles.

In the study performed by Nam and coworkers, the model pores were shrunk controllably to a final opening of 1 nm (Figures 1.3 (b) and (c)) after 1100 cycles of ALD. Compared to top-down approaches, this fabrication route is scalable, relatively less energy intensive and economical while retaining high degree of precision.

Figure 1.4 describes a typical ALD process[21]. The metal precursor such as titanium tetrachloride ($TiCl_4$) is first introduced in the reactor, and it adsorbs on the substrate surface saturating it with precursor molecules. In the subsequent step, the reactor is purged by flowing an

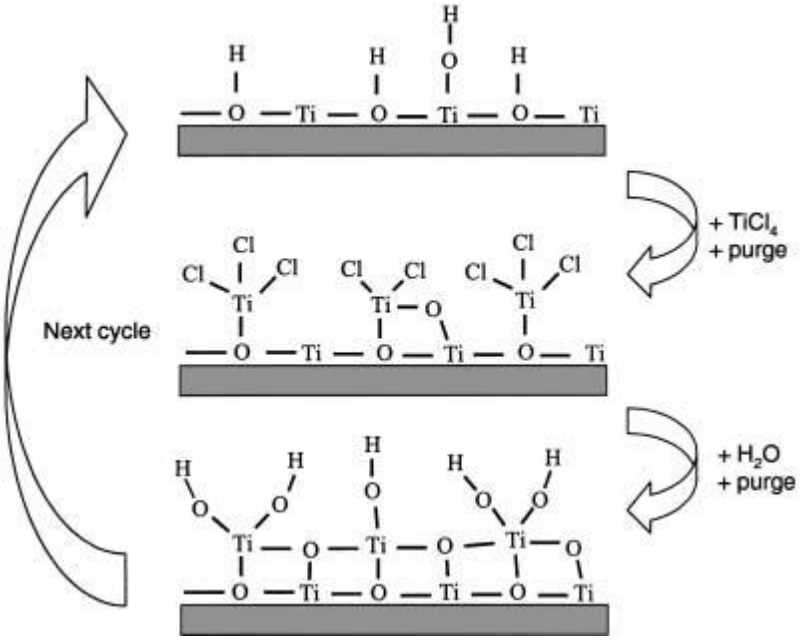


Figure 1.4: Representation of an ALD cycle. Reprinted by permission from John Wiley and Sons Publishers Ltd: Angewandte Chemie International Edition[21], copyright (2003).

inert gas or nitrogen to remove any excess precursor. The metal precursor does not react with itself, and this gives rise to self-limiting growth mechanism of ALD. The purge step leaves the gas phase of the system free of metal precursor and the surface is covered with a monolayer of metal precursor. The next step usually involves introducing a reactant such as H_2O in the

reactor. The oxidizer reacts with the adsorbed precursor molecules to remove the metal ligand groups, and form a monolayer of a metal oxide film with a thickness of the order of 1Å. The final step of this process involves another inert gas purge to remove the reaction byproducts. The number of cycles can be repeated to deposit films of desired thickness. Since, no surface sites are left unexposed, ALD usually leads to high-quality films devoid of any defect.

Although ALD provides self-limiting growth and highly conformal films, its application is restricted by few major drawbacks. Firstly, the conformal nature of ALD results in a densified pore interior, and this leads to dramatic attenuation of the flux of the original support, and severely limits its applicability. The ideal scenario would be to form asymmetric structures instead of densified pores. These asymmetric pores would demonstrate remarkable improvement in solute rejection properties without compromising the membrane flux. This is due to the fact that the membrane resistance is concentrated only near the mouth of the pore, and the rest of the pores is uncoated.

Secondly, application of ALD for coating large pores (~ 100 nm) is also problematic due to long exposure and purge steps in ALD. The purge steps can account for 50-90% of the total cycle duration, and can lead to very low net growth rates in ALD[22]. In addition, many ALD chemistries employ elevated substrate temperatures which can severely damage thermally labile substrates such as polymeric membranes. Due to these limitations, it is desirable to find an alternative thin film deposition technique which can deliver high net film growth rates without compromising precision of ALD.

The focus of this thesis is to explore pulsed PECVD as an alternative modification technique for precise pore size reduction of model supports like track-etched membranes. Pulsed PECVD has been engineered as a high throughput alternative to ALD to deliver self-limiting

growth of metal oxides. Self-limiting growth in pulsed PECVD is achieved by applying a square wave modulation to plasma power. There are two contributors to film growth in pulsed PECVD- an ALD-like conformal mode when the plasma is off, and a PECVD non-conformal mode when the plasma is on. The relative contributions of these 2 growth modes can be varied, and thus the geometry of the nanopore can be tuned to fabricate asymmetric nanopores. A feature scale model has been developed to simulate and design nanopore geometries for different deposition conditions in pulsed PECVD[23]. Finally, the metal oxide surface of a nanopore was funcationalized by attachment of self-assembled monolayers to create a hydrophobic interface.

1.4 Pulsed PECVD: An Introduction

Pulsed PECVD has been engineered as a high throughput alternative to ALD for delivering self-limiting growth of thin films[24]. A wide variety of oxides like Al_2O_3[25], SiO_2[26], TiO_2[27]and ZnO[28] have been deposited using this method. Figure 1.5 compares the gas flow and plasma sequences employed for PEALD and pulsed PECVD, respectively[25]. In PEALD, introduction of the precursor and the oxidizer is separated by lengthy purge steps. In pulsed PECVD, the precursor and the oxidant are continuously introduced in the reactor, and the purge steps are eliminated. The elimination of purge steps leads to considerably shorter cycle durations, and deposition rates as high as 30 nm/min, which is an order of magnitude higher than the deposition rates obtained in most conventional ALD reactors, can be obtained in pulsed PECVD reactors.

Self-limiting growth of thin films is obtained by pulsing the plasma at low frequency (~ 1 Hz)[29, 30]. Self-limiting growth in pulsed PECVD means that the growth rate per cycle is independent of the plasma on and plasma off time durations. Two conditions must be met to

ensure this kind of film growth. The first condition is that there should be no deposition when the plasma is off. This requires that the precursor is inert in the presence of molecular oxygen, which is observed for many metalorganic precursors of interest. The second condition entails that there

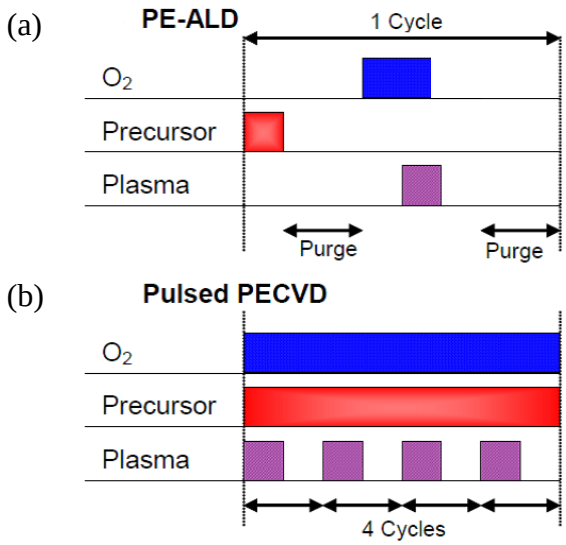


Figure 1.5: (a) Gas flow and plasma sequence in PEALD (b) Gas flow and plasma sequence in pulsed PECVD. Reprinted with permission from [25]. Copyright (2008), American Vacuum Society.

should be no deposition when the plasma is continuously on. This has been found to be true because the precursor is completely combusted before it can reach the substrate due to extremely fuel (precursor) lean conditions used in our reactors. The precursor can be either sacrificially deposited at the showerhead electrode where the inlet for the precursor is located or it can be oxidized in the gas phase and pumped out of the reactor.

In addition to throughput and self-limiting growth of thin films, the deposition mechanisms of ALD and pulsed PECVD will have a profound effect on the conformality or the geometry of the nanostructures. To understand how geometry of the nanopores can be tuned in pulsed PECVD it is essential to investigate growth mechanism of pulsed PECVD in greater

detail. Figure 1.6 shows a plot of concentration profiles of different gas species versus time[25]. Here we discuss the test case of aluminum oxide (Al_2O_3) deposition using trimethylaluminum (TMA) and oxygen. There are two growth modes which contribute to film growth in pulsed PECVD. The first growth mode is similar to ALD, and occurs when the plasma is off. During this step, the precursor (TMA) adsorbs on the substrate, and this adsorbed precursor layer is subsequently oxidized by atomic oxygen when the plasma is turned on. We refer to this growth mode as the ALD-like growth mode, and this mode leads to conformal film growth. The second growth component occurs when the plasma is turned on, and is similar to PECVD. During plasma ignition, the precursor molecules are converted into reactive intermediates (denoted by M*). These reactive intermediates stick to the surface in a PVD-like manner, and contribute to film growth only near the top of the feature leading to non-conformal film growth. These reactive intermediates are very unstable, and their concentration diminishes rather quickly due to their reaction with oxygen atoms. This rapid attenuation of these species leads to the self-limiting film growth during pulsed PECVD.

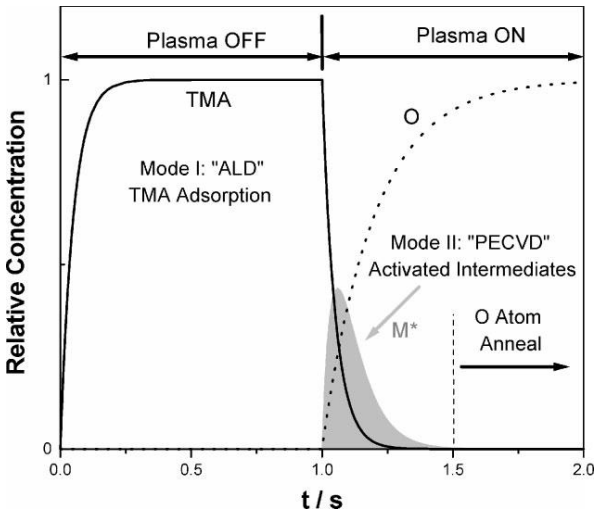


Figure 1.6: Growth Mechanism in pulsed PECVD. Reprinted with permission from [25]. Copyright (2008), American Vacuum Society.

The contribution of the ALD-like growth mode is constant (~ 1 Å /cycle) and is equal to the PEALD growth rate. However, the PECVD growth mode can be easily varied (1-10 Å /cycle) by manipulating the precursor exposure in the reactor. Thus, it is possible to tune the degree of conformality or the geometry of a nanopore by simply changing the growth per cycle (GPC) in pulsed PECVD. However, a feature scale model is required to predict the nanopore geometry as a function of the deposition conditions and the planar thickness. The next section will describe the development of a feature scale model which we have developed for design and fabrication of nanopores.

1.5 Feature Scale Modeling of Nanopore Geometries

In order to model transport at the nanoscale level it is essential to accurately determine geometry of the nanopore. This dictates that we should have predictive control over the pore size and shape of the nanopores fabricated during this work. This is relatively straightforward in processes like conformal ALD, as the pore size and geometry depend linearly on the planar thickness of the coating. Pulsed PECVD, on the other hand, offers us the flexibility of engineering conformality. However, achieving predictive control over pore size requires the input of a feature scale profile simulator.

As discussed above, there are 2 contributors to film growth in pulsed PECVD. The first mode is similar to PEALD as the precursor first adsorbs onto the surface when the plasma is extinguished, and this is followed by conversion of the adsorbed layer into an oxide film once the plasma is turned back on. This growth mode can be understood as the conformal mode where the thickness of the film is constant at all the points. The second growth mode occurs during plasma ignition when the precursor molecules are converted into highly reactive intermediate

species. These species deposit in a manner analogous to a PVD process. This growth mode is restricted mainly to the planar surface as the reactive intermediate species cannot penetrate into the feature due to their high reactivity.

The magnitude of the PVD-like mode can be adjusted by controlling the density of the precursor present at plasma ignition, and consequently the total (GPC) can be adjusted over a wide range (1 – 10 Å/pulse). The ability to vary the relative contribution of these two growth modes gives us the flexibility of engineering the nanopore geometry. This capability can be exploited to fabricate asymmetric nanopores which are important in applications which require high selectivity without compromising the membrane flux.

Figure 1.7 elaborates how the growth modes present in pulsed PECVD can be used to fabricate asymmetric nanopores. The figures show different deposition profiles (represented by white color) obtained by closing a pore which has an initial opening of ~ 100 nm. Figure 1.7 (a) represents the profile that would be obtained in a perfectly conformal process like ALD. In this case, the thickness of the coating is uniform throughout the feature, and this is an example of a densified or conformal pore that would be obtained in a post-ALD modification. It should be noted that this is similar to the first growth mode in pulsed PECVD. The second growth mode can be represented by Figure 1.7 (c), and is analogous to PVD. Here the film growth is restricted to the mouth of the feature, with little or no deposition occurring inside the feature. Figure 1.7 (b) shows the pulsed PECVD case, which is basically a combination of the ALD and PVD cases. When extending this technique to patterned substrates the resulting morphologies will depend on the specific feature geometry and the deposition conditions employed. One of the goals of this work was to develop and verify a transient feature scale model that is capable of predicting film conformality in pulsed PECVD.

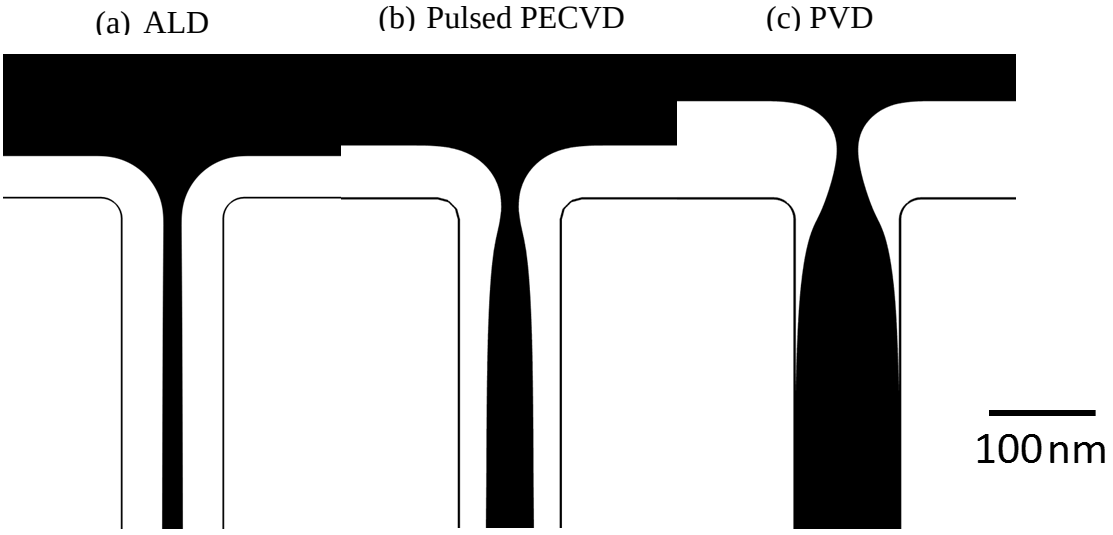


Figure 1.7: (a) Deposition profile in a perfectly conformal ALD process. (b) Deposition profile in pulsed PECVD (c) Deposition profile in a perfect sticking process like PVD.

In many semiconductor processing applications, the deposition layer has to coat the feature uniformly without leaving any voids or cracks behind. The ability to predict the shape of the deposition profile can lead to significant saving by reducing the parameter space employed during process development. There are three inter-related aspects involved in modeling of a thin film deposition process- (a) Transport of chemical species (b) reactions in the gas phase and on the surface, and (c) advancing boundary of the feature due to thin film growth. Typically, the pressure in vacuum deposition processes such as PECVD is of the order of 1 torr. At such low pressures, the mean free path of the molecules is of the order of tens of microns, which is much greater than the typical feature size. Under these circumstances, collisions between the walls and the molecules are much greater than the intramolecular collisions. Deposition, and hence the film growth, occurs through chemical reaction of the species at the surface of the feature. Subsequently, the surface reaction rates at all the local points on the feature surface are converted into a mesh velocity which is used to simulate evolution of the feature surface. The details of the implementation of this feature scale model are discussed in the next chapter.

1.6 Surface Functionalization of Nanopores

The transport of macromolecules through nanopores is hindered, and the interaction between the solute and the pore walls can govern the transport properties of these macromolecules. So, it is frequently necessary to modify surface chemistry of nanopore walls in order to reduce or enhance interaction between the solute and the pore walls. For example it is possible to selectively coat nanopore walls with hydrophobic groups such as octadecyltrichlorosilane (OTS, $CH_3(CH2)_{17}SiCl_3$) and create a hydrophobic environment inside the nanopore. These hydrophobic pore walls will preferentially allow a hydrophobic molecule to diffuse faster through the pore. Thus, it is possible to separate two molecules of identical size solely by exploiting these hydrophobicity-based interactions, and in many cases selectivity of the order of 100 can be readily obtained[31].

In this work, we propose to systematically modify the surface through application of self-assembled monolayers (SAMs) to create both hydrophilic and hydrophobic interfaces. So, the idea here is to exploit surface interactions, in addition to precise pore shrinkage, as another handle to control transport inside nanopores. In this strategy, the model support with an initial opening ~ 100 nm is shrunk by pulsed PECVD of metal oxide. In the next step, functional groups such as silane are anchored to the metal oxide surface of the nanopore to create hydrophobic or hydrophilic interfaces.

OTS is a commonly used silane derivative employed for creating highly hydrophobic interfaces. It binds with a pre-hydroxylated metal oxide surface through a covalent bond which is stable upto temperatures as high as 450^oC. In addition, it is possible to control the process conditions to add only a monolayer of OTS (~ 2.8 nm) to surfaces. This is especially important while modifying very small holes (< 10 nm) to prevent clogging. Another advantage of OTS

modification is that it is possible to anchor other functional groups such as polyethylene glycol (PEG) using pre-silanated surfaces. Thus different functional groups can be attached to the nanopore walls through an intermediate silane moiety. This strategy gives us a lot of flexibility to fabricate functionalized nanopores tailored specifically to the desired membrane separation application.

1.7 Thesis Overview

The overall goal of this thesis to engineer pulsed PECVD as an alternative to ALD for precise tailoring of pore size of model supports. Digital control over pore closure, high deposition rates, and ability to engineer degree of conformality are the main advantages of this fabrication approach. The first goal of this project is to establish predictive control over conformality in pulsed PECVD. Feature scale modeling tools were developed and validated using cross section microscopy to achieve this goal. Subsequently, pulsed PECVD, PEALD and PVD were employed to modify track etched membranes, and experimental measurements of flux and solute rejection were used to test the membrane performance. Lastly, the role of surface chemistry was examined by systematic modification of metal oxide surfaces through the attachment of hydrophobic silane groups using self-assembly techniques.

In contrast to ALD, predicting geometry of the modified pore is a non-trivial task in pulsed PECVD, and requires input from a profile simulator. To achieve this goal, a feature scale model was developed to simulate deposition profile evolution in steady state- and transient-deposition processes. The model was developed in COMSOL, and is based on a diffusion reaction approach. The model was initially developed for steady state processes like CVD. A step coverage modulus (analogous to sticking coefficient) was used to characterize the deposition profiles. The model was subsequently extended to simulate profiles in transient pulsed PECVD.

The deposition profiles in pulsed PECVD are a function of the relative contribution of the PVD-like and ALD-like growth modes, as well as the aspect ratio of the feature. The model was verified by cross-section microscopy of deposition profiles on patterned trenches and cylinders fabricated using electron beam lithography and reactive ion etching. The implementation of the feature scale model and its validation is presented in Chapter 4.

Pulsed PECVD, PEALD and PVD were used to modify polycarbonate TE membranes with an initial pore opening of 100 nm. The pore size is relatively large which makes modification with PEALD cumbersome. The pores were tailored by coating the membrane with different thicknesses of material deposited using the three techniques, and the modified membranes were tested for their flux and selectivity. PVD was used for pore modification as it exhibits perfect sticking behavior ($\gamma = 1$), which represents the extreme for non-conformality. Perfectly conformal ALD exhibits the opposite behavior ($\gamma \rightarrow 0$), and these techniques establish well-characterized bounds that serve as benchmarks for evaluating the pulsed PECVD- modified TE membranes. The feature scale model described earlier was used to model geometry of the modified pores, and these geometries were subsequently used to predict flux behavior of the modified membranes. Both PVD and pulsed PECVD form asymmetric pores, and can be used to overcome flux-selectivity trade-off. In addition to its flux advantages, high degree of precision over pore closure can be obtained in pulsed PECVD due to its self-limiting nature. ALD-based modification is extremely slow relative to the other techniques, but some non-conformal behavior is also seen in ALD due to exposure limitations. The discussion on fabrication of asymmetric pores, and their membrane performance is presented in Chapter 5.

At the nanoscale, interactions between the solute and the pore walls can dominate the transport properties. To exploit these interactions, surface modification strategies have been

commonly employed to modify the environment inside the pores. For example, silane moieties can be easily attached to hydroxylated metal oxide surfaces to create hydrophobic interfaces. As a model system, attachment of OTS SAM to planar aluminum oxide surfaces was studied in-depth. The objective of doing this study was to develop a robust recipe for attachment of these SAMs to planar surfaces, which could then be extended to nanoporous substrates. However, the polymeric track-etched membranes showed signs of severe degradation in the silane solution, and hence, this surface modification approach had to be abandoned. The kinetic and thermodynamic investigations of the attachment of OTS SAM to aluminum oxide coated surfaces are discussed in detail in Chapter 6.

CHAPTER 2

MODELING DETAILS

This chapter provides an overview of the modeling work performed in Chapters 4 and 5. Chapter 4 has been previously published in Journal of Vacuum Science and Technology B, whereas Chapter 5 will be submitted for publication in a peer reviewed journal. These chapters are reproduced in this work with only slight changes. In this chapter those modeling details are provided in full, while the specific details for the work done in each chapter are contained therein. This chapter describes the development of a feature scale model used for predicting deposition profiles in pulsed PECVD. Subsequently, procedure used for predicting flux through nanoporous membrane is described in brief.

2.1 Feature Scale Modeling

In order to model transport at the nanoscale level it is essential to accurately determine geometry of the nanopore. This dictates that we should have predictive control over the pore size and geometry of the nanopores fabricated during this work. This is relatively straightforward in processes like ALD, as the pore size and geometry depend linearly on the planar thickness of the coating. Pulsed PECVD, on the other hand, offers us the flexibility of engineering conformality or the shape of the nanopore. However, achieving predictive control over pore size requires the input of a feature scale profile simulator. This problem was solved by developing a feature scale model capable of simulating the nanopore geometry as a function of the deposition conditions. This model was built in COMSOL 4.3b using a diffusion reaction framework. Initially, the model was developed for a steady state CVD process, and then extended to the transient case of pulsed PECVD. There were two reasons for this approach. Firstly, our steady state model

employs the same methodology and same set of assumptions as the pulsed PECVD model. Secondly, the steady state model has been studied in-depth in the literature, and serves as metric to compare and verify our simulations. In the next section, the governing equations in our model and details regarding implementation of the model in COMSOL are described.

2.1.1 Modeling of Steady State Deposition Processes

Figure 2.1 shows a representative computational domain and the boundary conditions employed in our model. Our model is 2-D axisymmetric, and hence, only half of the cylinder cross-section is shown in Figure 2.1. The control volume consists of a cylindrical feature with a radius (R) of 50 nm having a height (H) of 400 nm. A specified region above the cylindrical feature is included in the control volume. The sharp corners of the feature have been smoothed to avoid any mesh distortion during film growth.

The overall physics of the model consists of 3 inter-related aspects which are coupled together: (a) Transport of gaseous species (b) Reaction Chemistry (c) Dynamic profile evolution of the surface. Predicting deposition profile requires coupling of all 3 components in a feature scale model.

The key assumptions in our model are listed below:

- The frequency of particle-particle collisions is negligible relative to particle-wall collisions; i.e., we are operating in Knudsen flow regime.
- The open end of the feature is exposed to low-pressure ideal gas. The convective mode of transport can be neglected within the boundary layer which is a few microns from the substrate surface.

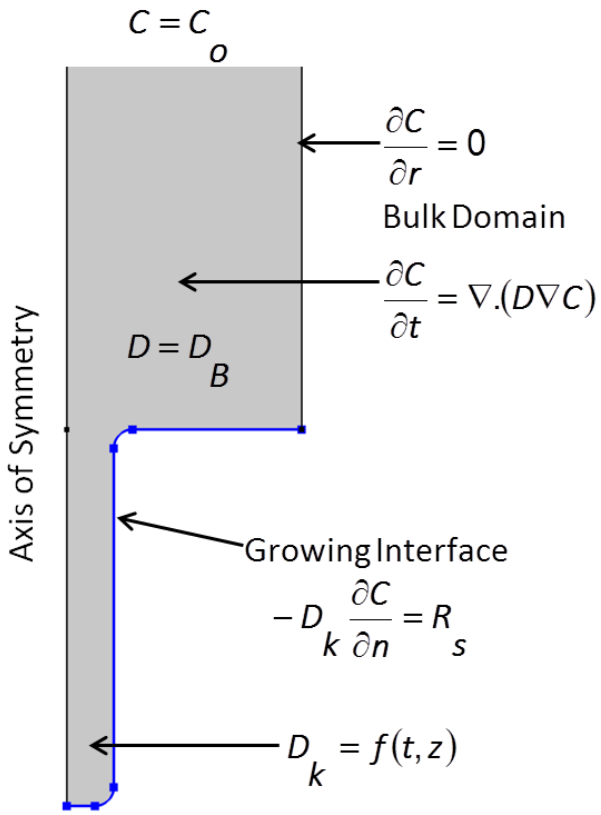


Figure 2.1: Computational domain and governing boundary equations[23].

- Surface diffusion is negligible.

In low pressure chemical vapor deposition (LPCVD), gas transport inside sub-micron features is dominated by molecular flow. In pulsed PECVD, the operating pressures (*P*) are typically less than 1 Torr, and the characteristic feature size employed in this study is about 100 nm. The mean free path at this operating pressure is around 35 μm and the Knudsen number (*Kn*) is ~ 350. In this regime, collisions between gas molecules and the feature walls are much greater in number than inter-molecular collisions. In the next section, all the governing equations used in our model are discussed in detail.

Due to the small size of our features, transport by convection mode is insignificant in our computational domain, and mass transport is assumed to occur only through diffusion. Equation 2.1 is a result of species mass balance in the control volume.

$$\nabla.(D\nabla C) = \frac{\partial C}{\partial t} \tag{2.1}$$

where, C is the concentration of the reactive species, D is the diffusion coefficient.

We assume that flux of the reactive species coming from the reactor (bulk domain) is uniform at the top of the control volume. The concentration at the top of the domain is calculated from the partial pressure (*pp*) by assuming ideal gas behavior. Since, we are operating at reactor pressures less than 1 Torr this assumption can be safely applied here. We assume a stirred tank reactor model for our reactor, and hence, concentration at the top of the domain is equal to the bulk concentration.

$$C = C_0 \tag{2.2}$$

where C_0 is the concentration of the reactive species at the entrance of the control volume. Although this assumption may not be strictly correct, and there may be additional mass transfer resistances in the reactor, actual C_0 can be found by employing a reactor scale model. However, for the purpose of studying profile evolution this is not essential.

Other assumption in our model is that pores are isolated and deposition in any feature is unaffected by the deposition in adjacent features. This assumption gives rise to an insulating boundary condition on the sidewall.

$$\frac{\partial C}{\partial r} = 0 \tag{2.3}$$

The reactive surface is highlighted in blue in Figure 2.1. The diffusion flux on the reactive surfaces is equal to the product of the diffusion coefficient and the local concentration gradient. Here, we neglect any mass transport due to surface diffusion.

$$J = -D\frac{\partial C}{\partial z} \tag{2.4}$$

We employ a time-dependent and position-dependent diffusion coefficient (D) in this study. In chemical vapor deposition, D depends on the flow regime. For Kn <<1, D is given by the continuum value D_B. Equation 2.5 is derived from kinetic theory of gases and is used to calculate D_B[32]. This diffusion coefficient is appropriate in the bulk domain as the characteristic feature size is of the order of centimeters (>> mean free path of gas molecules).

$$D_B = \frac{1}{3} v_m \lambda \tag{2.5}$$

where v_m is the mean molecular speed. As discussed before, the gas transport inside the feature occurs in the high Knudsen number flow regime. The Knudsen diffusion coefficient (D_k) in this flow regime is a function of the instantaneous local radius and varies with position (z) and time (t) as the opening shrinks due to material deposition[33].

$$D_k(z) = \left\{ \frac{20 + 8\left(\frac{H}{2R(z)}\right)}{20 + 19\left(\frac{H}{2R(z)}\right) + 3\left(\frac{H}{2R(z)}\right)^2} \right\} \frac{H}{4} v_m \tag{2.6}$$

Transport of reactive species by diffusion ultimately results in film growth by heterogeneous surface reaction. The rate of heterogeneous surface reaction is equal to the diffusion flux.

$$J = R_s \tag{2.7}$$

We assume that homogeneous gas phase reactions contribute negligibly to the consumption of the reactive species. Any homogeneous gas phase reaction can be easily incorporated in our model but we avoid this complication in the present study.

$$R_g = 0 \tag{2.8}$$

Also we assume that the heterogeneous surface reaction rate is first order in the reactive species.

$$R_s = k_s C \tag{2.9}$$

where the rate constant (k_s) was evaluated using gas collision theory and a sticking coefficient formulation.

$$k_s = \gamma \sqrt{\frac{kT}{2\pi m}} \tag{2.10}$$

For the PVD-like growth mode the value of γ was set to unity, while for the ALD-like mode this value was made sufficiently small to ensure perfect conformality as described below.

Topography simulation is one of the most important components of any deposition profile simulator. There are many algorithms like level set method[34] and string/segment based algorithms[35] which have been used to simulate film growth. We use arbitrary lagrangian eularian (ALE) scheme for surface propagation. Compared to other algorithms, ALE requires less memory and is computationally less intensive[35]. The mesh extension velocity is governed by the surface reaction rate calculated from equation 2.9. The moving mesh tracks the evolving feature morphology.

$$v = R_s . V_m \tag{2.11}$$

where v is the mesh extension velocity or the local deposition rate and V_m is the molar volume of the deposited material.

The model equations described above can be written in dimensionless form to extract important parameters which govern the step coverage (SC) in LPCVD. For a fixed initial geometry and Knudsen number, the SC depends on a single dimensionless parameter known as the step coverage modulus (ϕ)[33]. ϕ is the ratio of characteristic surface reaction rate to the mass transfer rate by diffusion.

$$\phi = \frac{Characteristic\ Deposition\ Rate}{Diffusion\ Rate} = \frac{(k_s C_0) * (Sidewall\ Area)}{D_{k0} * \left(\frac{c_0}{h}\right) * (Cross\,sectional\ Area)} \qquad (2.12.a)$$

$$\phi = \frac{2k_s H^2}{RD_{k0}} \qquad (2.12.b)$$

Where, C_0 and D_{k0} are the concentration of the reactive species and Knudsen diffusion coefficient at the feature mouth respectively.

Figure 2.2 shows how the deposition profiles vary as a function of ϕ. For extremely low values of ϕ, the profiles are perfectly conformal (Figure 2.2 (a)). A conformal profile implies that the thickness of the deposition layer labeled as 't' is uniform throughout the feature. This can be contrasted against an asymmetric PVD-like profile where the deposition is concentrated near the feature mouth with little or no deposition inside the feature. In the protocol described in the appendix, procedure for simulating Figure 2.2 (c) is described. The remaining cases can be simulated by simply changing ϕ or the step coverage modulus of the deposition process. This translates into changing the reaction rate constant k_s in our simulations. It should be noted here that the kinetic theory of gases provides an upper limit to k_s corresponding to perfect sticking

case, whereas reducing k_s results in more and more conformal films, and below a certain value, the deposition profiles are perfectly conformal, and hence, identical.

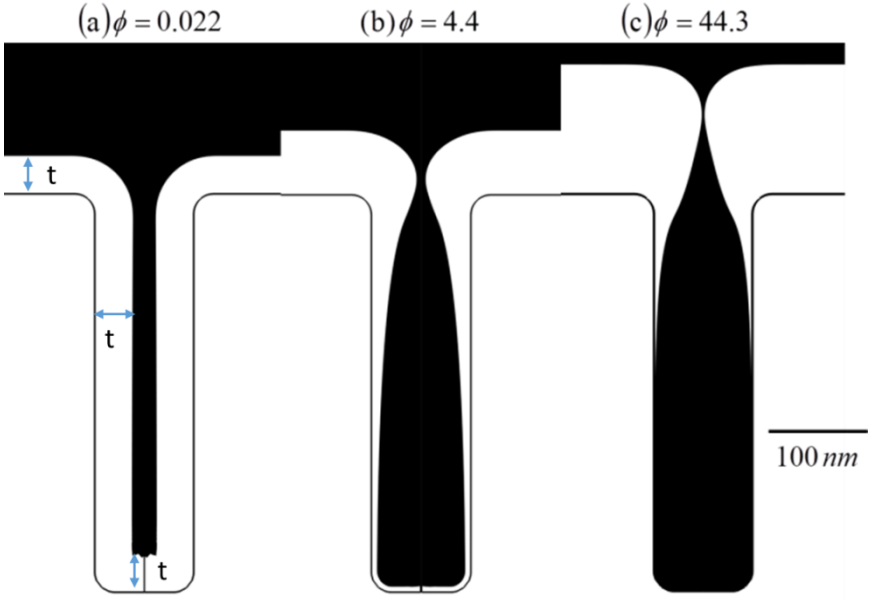


Figure 2.2: Deposition profiles as a function of ϕ. Deposited material is represented by white color, and the surrounding gas phase is represented by black color[23].

The diffusion reaction model for simulating steady state deposition processes was implemented in COMSOL version 4.3 b. 'Transport of Diluted Species' node was used to model transport of reactive species inside the feature. This application mode was coupled with the 'Moving Mesh' application mode to simulate profile evolution during deposition. A hyperelastic mesh smoothing method was employed with a smoothing factor of 0.1 during mesh movement. The mesh was periodically remeshed to minimize mesh distortion, and to ensure proper resolution of the evolving geometry. For simulating the non-conformal PVD-like case, the rate constant was evaluated at the reactor operating temperature. The step coverage modulus for the PVD-like case was calculated to be 88. To simulate conformal deposition case, a much smaller

value of rate constant k_{ALD} was determined by running simulations for a range of k values and picking the value that gave us a perfectly conformal profile.

A time- and position- dependent Knudsen diffusion coefficient was employed in the simulation based on equation 2.6. The evolving pore radius R(z) was tracked by using general projection and general extrusion operators, and fed into equation 2.6 to evaluate the diffusion coefficient. This subroutine is crucial as the local diffusion coefficient has to be calculated at each time step. The general projection operator is an integration operator, and it is used to integrate in the 'r' dimension. This is necessary in order to obtain the pore radius 'R' as a function of the height (z) of the feature. In the next step, the pore radius is 'extruded' back from a 1-D model to the original 2-D asymmetric model using a general extrusion operator. Thus our feature scale model requires a coupling of 2 models. The next section discusses implementation of pulsed PECVD simulations in COMSOL.

2.1.2 Modeling of Unsteady State Pulsed PECVD Process

Figure 2.3 shows the modeling scheme employed for simulating the transient pulsed PECVD case. As discussed earlier, there are 2 growth modes in pulsed PECVD. The first growth mode is ALD-like and results in perfectly conformal films. Initially, we will neglect any diffusion limitations present in ALD, and assume that ALD results in perfectly conformal films. This is similar to a steady state CVD profile with a very low step coverage modulus ϕ_{ALD}. The second growth mode occurs during plasma ignition, and is characterized by perfect sticking behavior. This type of profile will be non-conformal, and will be characterized by a step coverage modulus of ϕ_{PVD}. Thus every cycle in pulsed PECVD consists of 2 deposition modes characterized by two growth modes represented by ϕ_{ALD} and ϕ_{PVD} which have time durations

Δt_{ALD} and Δt_{PVD} respectively. In order to simulate profiles in pulsed PECVD we simply alternate between these two growth modes till the desired planar thickness is achieved. The relative contribution of these two growth modes is characterized by a parameter '*R*' which is determined experimentally. *R* is simply the ratio of the contribution of the PVD-like growth mode to the contribution of the ALD-like growth mode. The contribution of the ALD-like growth mode is fixed. However, growth rate in the PVD-like growth mode can be arbitrarily varied by changing the precursor density in the reactor. For example, if the total growth per cycle (GPC) is 2 Å /cycle, and if the contribution of the ALD mode is 1 Å /cycle then the corresponding '*R*' value would be 1.

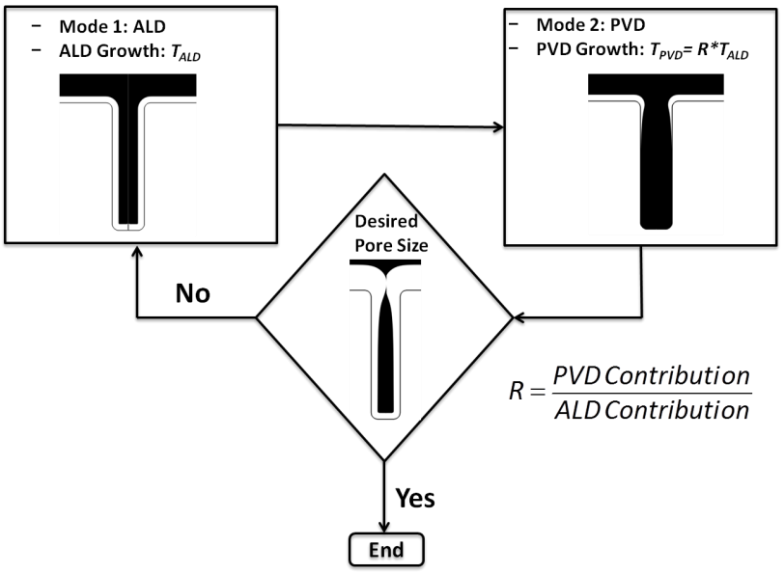


Figure 2.3: Modeling Scheme for pulsed PECVD[23].

Pulsed PECVD can be used to obtain a spectrum of conformalities between the extreme cases of conformal ALD and non-conformal PVD profiles. As *R* is increased the profiles become more and more non-conformal, and increasingly resemble the PVD case. To simulate different pulsed PECVD scenarios, '*R*' values can be varied by simply changing the contribution of the

PVD growth mode while keeping the ALD contribution constant. The growth rates in pulsed PECVD can be typically varied from 1-10 Å /cycle, and hence assuming ALD contribution of 1 Å /cycle, the *R* values can be experimentally varied from 1 to 10. In our model this can be easily achieved by keeping Δt_{ALD} constant and progressively increasing Δt_{PVD} so as to deposit more and more material during the PVD growth mode. It should be pointed out here that the ALD growth mode considered uptil now has been assumed to result in perfectly conformal deposition profiles even in very narrow pores. In reality this requires use of very high precursor doses, which might not be feasible in actual ALD processes. The next section briefly describes modeling approach employed to take into account this non-ideality in our model.

2.1.3 Modeling of Exposure-Limited ALD Case

Gordon and coworkers have developed scaling relationships which can predict the precursor exposure required for conformally coating a feature of a given aspect ratio[36]. In our work, we employ these scaling relationships to simulate non-ideal ALD behavior. We define a parameter termed as 'critical aspect ratio' or a* which is the maximum aspect ratio that can be conformally coated in an ALD process for a given precursor exposure. This parameter accounts for the precursor diffusion limitations, and depends on the experimentally determined precursor exposure. To incorporate the precursor diffusion limitations, the aspect ratio (a) at all the feature locations is continuously tracked. The modified simulator employs an 'if' conditional statement to terminate the film growth at all the points where a > a*. Figure 2.4 shows the modified conformal profiles for different a* values. As a* decreases, the profile become increasingly non-conformal as the precursor cannot diffuse to the feature bottom.

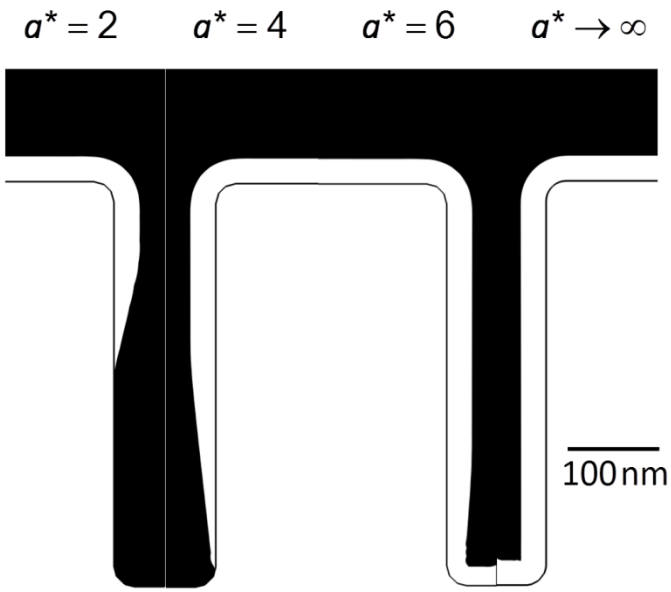


Figure 2.4: ALD deposition profiles as a function of critical aspect ratio a*[23].

2.1.4 Model Validation

The model was validated by deposition of oxide on patterned trenches and cylinders. These patterned features were fabricated at the Oak Ridge National Laboratory using electron beam lithography and reactive ion etching. For both cases, the openings were shrunk by using pulsed PECVD of aluminum oxide. The PVD-like and ALD-like components were equal for both the depositions i.e. $R = 1$. The agreement between the experimental and the simulated profiles was impressive in both cases. The model verification results are discussed in detail in chapter 4.

2.2 Modeling Flux of Nanoporous Membranes

The flux behavior of the modified TE membranes was modeled using a laminar flow model in COMSOL. The geometry of the modified TE membranes was simulated using the feature scale model described above. Supports modified with different thicknesses of aluminum

deposited by thermal evaporation were simulated by assuming perfect sticking behavior. The pulsed PECVD- modified supports were simulated using the transient model with the parameters set at R = 1 and a^*=8.2. The features are simulated for different planar thicknesses, and the geometry of the modified pore is exported to a 2-D axisymmetric COMSOL model to determine flux through a single pore. In order to compare with experimental measurements, the model flux of the modified pore is normalized with the flux of an unmodified pore to obtain the relative flux.

CHAPTER 3

EXPERIMENTAL DETAILS AND CHARACTERIZATION TECHNIQUES

This chapter provides an overview of the experimental details for the work performed in chapters 4-6. Chapters 4 and 6 have been published whereas Chapter 5 is to be submitted for publication in a peer-reviewed journal. Due to length constraints, some of the details were not discussed in these chapters. In this chapter those experimental details are provided in full. Specific details for the work done in each chapter is contained in those chapters.

First, this chapter discusses the model supports employed in this work for pore modification investigations. Secondly, different deposition techniques such as pulsed PECVD, PEALD and PVD used for tailoring pore size of track-etched (TE) membranes are described. The next section describes different tools such as ellipsometry and scanning electron microscopy used for characterizing the nanoporous membranes fabricated in this work.

3.1 Model Supports

The pore modification strategy employed in this work is predicated by the availability of well-defined model supports. Model supports contain high-aspect ratio pores with an opening ~ 100 nm. This section describes two model supports explored during this work.

3.1.1 SOI Membrane Support

The initial plan was to fabricate model supports in silicon on insulator (SOI) wafers using electron beam lithography and cryogenic etching at the Center for Nanophase Materials Sciences, a user facility at the Oak Ridge National Laboratory. These silicon supports would have well-defined holes which can be easily analyzed using cross section microscopy. Also, it is

easy to regenerate these pristine supports by selectively etching pulsed PECVD metal oxide with respect to silicon.

The device envisaged in this work is shown in Figure 3.1, and it consists of 25 mm discs which could easily fit into our membrane testing apparatus. The disc comprised of a 5*5 array of 'active' regions each having an area of ~ 4 mm^2 which ultimately opened up into the 'window' region. The active region consisted of regularly spaced holes with a desired opening between 100 to 200 nm. The periodic structure repeats over the entire active region area. The depth of the active region was about 2 µm, and during fabrication, circles with different diameters ~ 100, 134, 170 and 200 nm were patterned on the wafer. The final device was built on a SOI wafer where the oxide insulator served as an etch stop for windows to the active region.

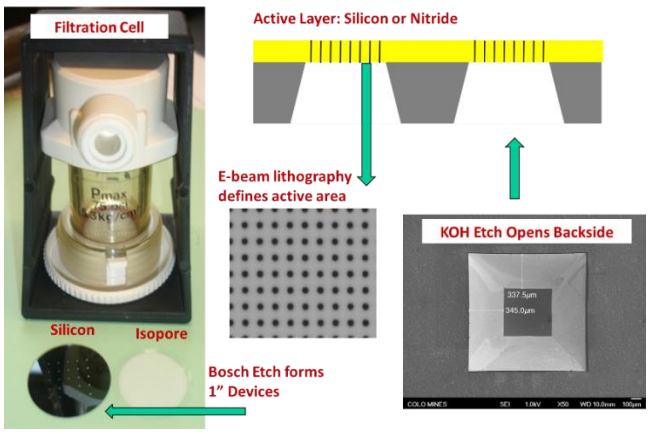


Figure 3.1: Model silicon support placed alongside an isopore membrane support. Model silicon supports comprise of active and window regions. The active region consists of an array of well-defined holes patterned using electron beam lithography and cryogenic etching. The window region is formed from the backside using KOH etch to create a membrane.

Extensive efforts were expended to optimize this approach and create robust membrane templates as documented in Appendix A. However, due to several problems, limited time and resources we abandoned this approach in favor of commercial track-etched membranes as model

supports. Briefly, the two major challenges encountered were the inability to conduct perfectly anisotropic etching and the mechanical fragility of the active layer.

The most crucial step in the fabrication of these model supports is the cryogenic etching step in which the pattern is transferred from a resist mask to the underlying silicon device layer. Optimizing the etch profile without compromising the integrity of the mask was found to be a major challenge in the fabrication of these high-aspect ratio features. Figure 3.2 (a) shows undercutting of the etch profile due to insufficient passivation. This is a common problem in etching sub-micron features. It is difficult to maintain straight sidewalls due to isotropic etching, and the feature opening at the end of the etch process (~ 500 nm) is much larger than the size of the patterns formed by electron beam exposure (~ 100 nm). Another issue which was commonly encountered while using these models supports was the cracking of the active layer containing the pores. The presence of cracks was found to be absolutely detrimental for any potential membrane application.

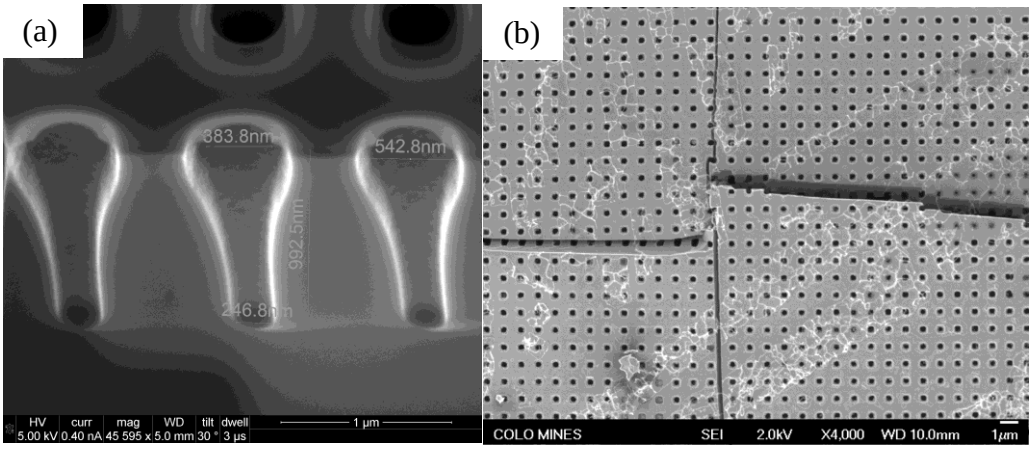


Figure 3.2: (a) Undercutting in the silicon layer due to inadequate passivation (b) Cracking of the active layer.

3.1.2 Track-etched Membrane Support

Track etching is a popular technique in membrane technology for fabricating membranes with precisely determined size. These membranes are fabricated by bombarding polymeric films with heavy nuclei to create damaged tracks[18]. These tracks are subsequently etched chemically to create sub-micron sized pores. Track-etched (TE) membranes are very cheap, and are available in different sizes, shapes and pore densities. Figures 3.3 (a) and (b) show the top view and cross-section SEM micrographs of a TE membrane support employed in this work. The nominal pore size of the membranes is about 100 nm. The thickness of these membranes is about 25 μm, and the initial aspect ratio of these membranes is about 250. A few doublets are seen in these membranes which have a pore size much greater than 100 nm. These doublets are formed by fusion of adjacent single pores, and account for about 7.5 % of the total number of pores in our sample. For pore modification strategy described in the next section, TE membranes are used as templates. The pore size and shape of these membranes is controllably tuned to form asymmetric nanopores.

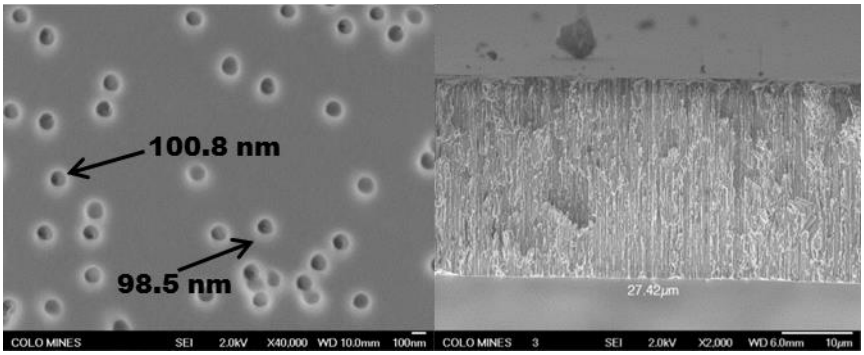


Figure 3.3: (a) Plan view SEM micrograph and (b) Cross-section image of a track-etched membrane support employed for pore modification study in this work.

3.2 Pore Modification Techniques

In this section, different deposition techniques like pulsed PECVD, PVD and PEALD are described in detail.

3.2.1 Pulsed PECVD

Pulsed PECVD depositions were done in an existing custom-built parallel plate capacitively coupled plasma (CCP) reactor shown in Figure 3.4 [37]. To generate vacuum in the reactor, it is evacuated using a 2 stage Edwards mechanical pump (E2M40). All gases such as argon, oxygen and metal precursor were premixed in a teflon tube before entering a showerhead. After mixing, the gas stream was distributed through a perforated showerhead which also acted as the RF-powered electrode used to generate plasma during depositions. The RF power supply was connected to the showerhead electrode through an intermediate matching network to minimize reflected power. Also, the showerhead was encased in a Teflon casing for electrical isolation from the grounded reactor walls. A narrow annulus formed between the showerhead and the reactor walls served as the outlet for reaction byproducts to exhaust.

Growth per cycle (GPC) and film quality can be strongly dependent on the substrate temperature, and it is important to uniformly heat the substrates during depositions[27]. For all depositions, the substrates were resistively heated from the backside by a disc substrate heater using a variac voltage transformer. The temperature was monitored by a thermocouple in contact with the top surface of the reactor lid. Before beginning any depositions, sufficient time was given for the substrates to reach a steady state temperature to avoid any temperature variations during depositions. Since the polymeric TE membrane supports degrade at temperatures higher than 140 °C, the substrates were usually maintained at temperatures less than 100 °C.

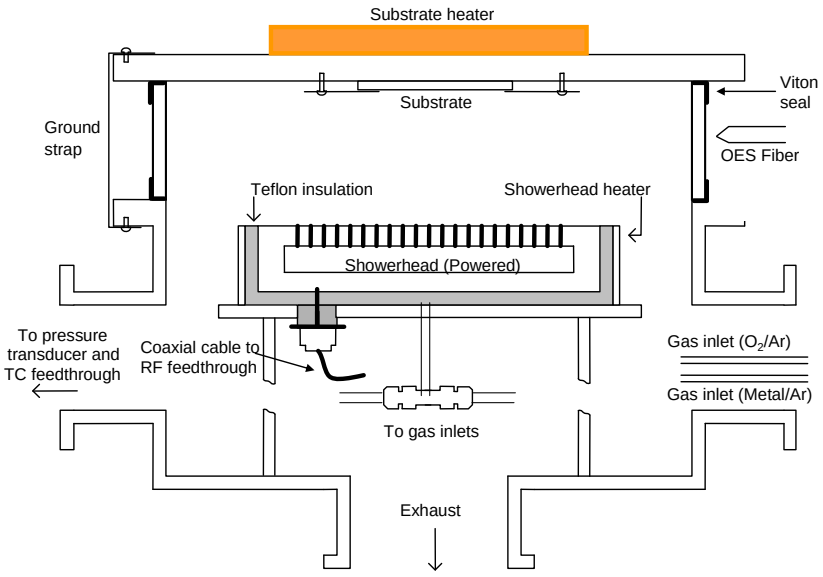


Figure 3.4: Schematic of the parallel plate capacitively coupled plasma (CCP) reactor employed for pulsed PECVD and PEALD depositions. Figure taken from [37].

Film growth in pulsed PECVD occurs due to reaction of metal precursors with oxygen in plasma. Precursors like trimethylaluminum (TMA) and titanium tetrachloride ($TiCl_4$) were supplied to the reactor using a bubbler setup. During bubbler operation, a non-reactive carrier gas like Ar was flown through an inlet tube which is submerged in a pool of liquid precursor. As the Ar gas bubbles out, it becomes saturated with the metal precursor, and a controlled amount of precursor can thus be supplied to the reactor. The bubbler is also immersed in a cooling bath to maintain the bubbler temperature at about 15 °C. The precursor flowrate can be easily varied by adjusting the bubbler pressure or the carrier gas flow rate according to Equation 3.1.

$$F_{pre} = \frac{F_{carr} P_{Vap}}{P_{Bub} - P_{Vap}} \qquad (3.1)$$

where F_{pre} is the precursor flowrate, P_{Vap} is the vapor pressure of the precursor calculated from Antoine's equation, F_{carr} is the flowrate of the carrier Ar gas and P_{Bub} is the bubbler pressure controlled using a neddle valve.

All the gases used during the deposition such as argon and oxygen were of ultra-high purity (UHP) grade. The flow of these gases was maintained using mass flow controllers (MFCs). The pressure in the reactor as well as the bubbler pressure was measured using a pressure transducer which was connected to a pressure readout display. The reactor pressure was maintained around 0.8-0.9 torr for different depositions performed in this work, and the plasma power was set at 50 W. During depositions, the matching network was tuned to maintain the reflected power well below 5 W. To achieve self-limiting growth, the plasma was pulsed at a low frequency ~ 1 Hz using a square wave modulation applied using LabVIEW. The thickness of the deposited film was varied by simply adjusting the number of pulses or cycles.

3.2.2 Physical Vapor Deposition

Thermal evaporation is part of a family of deposition techniques known as physical vapor deposition (PVD). These techniques typically result in non-conformal deposition profiles due to perfect sticking behavior (γ=1). This means that the membranes fabricated using PVD would be asymmetric, consisting of a thin deposition layer near the mouth of the pore, whereas there would be little or no deposition inside the pores. So, PVD- modified membranes can serve as a good metric for comparing the performance of pulsed PECVD- modified asymmetric TE membranes.

Figure 3.5 shows a schematic of the apparatus used for depositing aluminum onto TE membranes. The apparatus consists of a diffusion-pumped bell jar with a base pressure of 10^{-7} Torr. Aluminum pellets are placed in a tungsten boat, and are resistively heated by applying high voltage across the boat. As temperature increases, the metal vaporizes and deposits on the substrate (TE membranes) without undergoing any chemical decomposition. The filament

current is maintained at 40 amperes, and the resulting growth rates are ~ 40 Å /s. These growth rates are much higher than pulsed PECVD growth rates, and it is routinely possible to deposit very thick films (> 1µm thick) using thermal evaporation. The quartz crystal monitor (QCM) determines the thickness of the evaporated film by correlating the change in resonance frequency of the crystal with the change in the mass of the crystal. As soon as the desired thickness is achieved, a shutter is used to isolate the sample (not shown in the figure), and the voltage is gradually reduced to zero to stop any additional deposition.

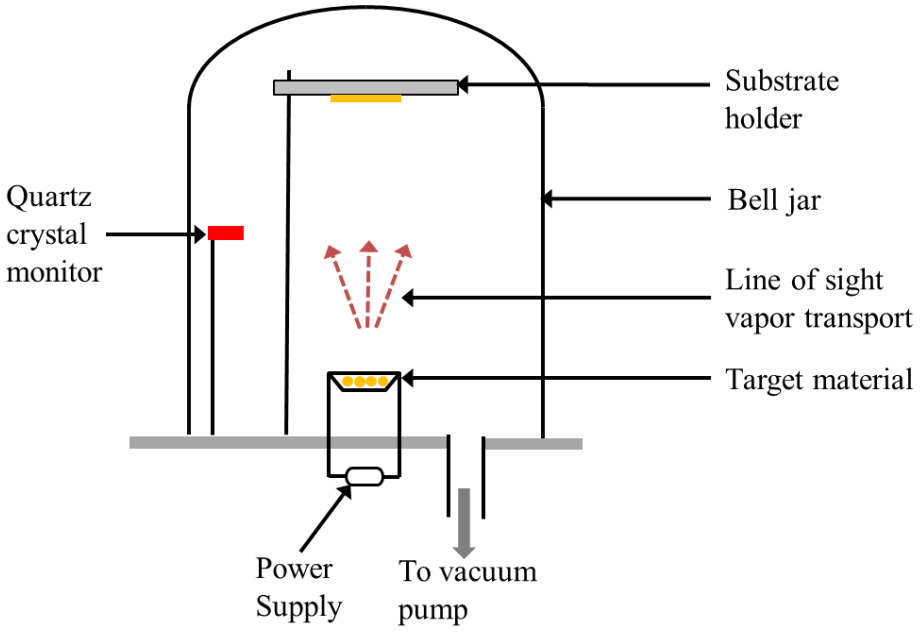


Figure 3.5: Schematic diagram of a resistive thermal evaporation system.

Different planar thicknesses of aluminum can be deposited by varying the time for which the sample is exposed to the metal vapor. In every run, 4 TE membranes were coated. Each TE membrane was surrounded by 4 dummy silicon wafers, which were subsequently analyzed after every deposition to determine the thickness of aluminum coatings using profilometry.

3.2.3 Plasma-enhanced Atomic Layer Deposition

Plasma enhanced atomic layer deposition (PEALD) of TiO_2 was carried out in the same parallel plate capacitively coupled plasma reactor described above in Figure 3.4. The plasma power was maintained at 50 W, and other process parameters like substrate temperature and gas flow rates were kept the same as in the pulsed PECVD process described before. In our reactor, oxygen and argon flow continuously in the reactor, and serve as the purge gas. The precursor flow was alternately directed to the reactor or directly to the vacuum pump through LabVIEW controlled solenoid valves.

The duration of precursor exposure, plasma exposure and purge steps were varied to ensure that we operated in the self-limiting growth regime. Figure 3.6 plots the GPC as a function of precursor dose times for PEALD of TiO_2. The GPC increases and then saturates at a dose time of 4 s. For PEALD modifications, a precursor dose time of 8 s was used in order to operate in the self-limiting regime. Note that this ensures that deposition on the surface is self-limiting, but exposure limitations certainly occur within the high aspect ratio support.

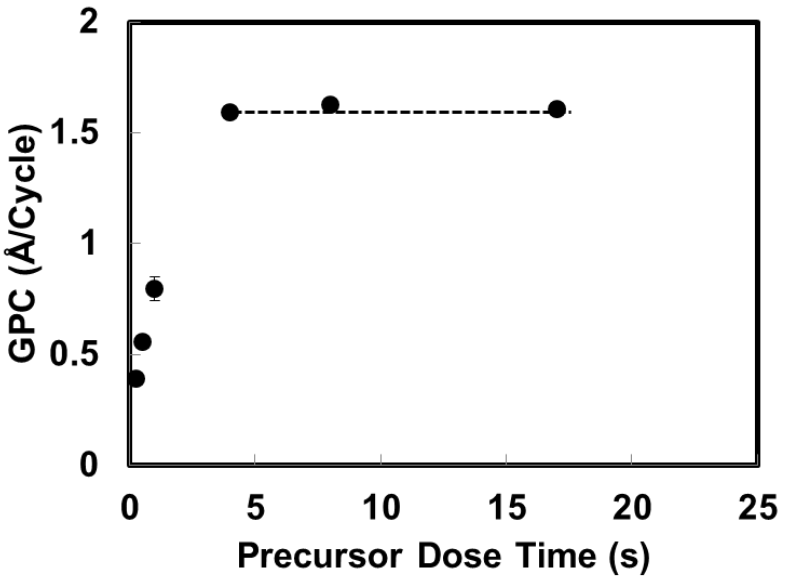


Figure 3.6: PEALD growth rates as a function of precursor dose times.

3.3 Membrane Testing and Characterization

The TE membranes modified in this work were characterized using a number of different techniques. The membrane was tested in a stirred ultrafiltration cell to determine the membrane flux and solute rejection. Dummy silicon wafers were placed alongside the TE membranes to determine the planar thickness of the coating deposited during PEALD, pulsed PECVD and PVD. The thickness of the TiO_2- modified TE membranes was determined using ellipsometry, and the thickness of Al-modified membranes was measured using profilometry. Scanning electron microscopy (SEM) was used to determine the pore opening of the pristine and the modified TE membranes. It should be noted here that the top view pore opening does not correspond to the narrowest pore dimension of the modified pore. This is attributed to the curvature of the deposition layer near the pore opening. This dimension is determined by simulating the pore geometry for different planar thicknesses and deposition conditions. Finally, a home-built contact angle measuring apparatus was used to determine the change in hydrophobicity of the membranes after modification with PEALD, pulsed PECVD and PVD. The next section describes the principles behind some of the techniques used for membrane characterization in greater detail.

3.3.1 Determination of Flux and Solute Rejection

Pure water flux (PWF) is determined by measuring flowrate of water under an overhead pressure of 10 psi using a stirred ultrafiltration cell (Amicon Milipore Co.) shown in Figure 3.7 (a). The resulting flux was reported as relative flux, which is the flux of the modified membrane normalized with respect to the flux of an unmodified TE membrane. Bovine serum albumin (BSA, 66 kDa, Sigma Aldrich) was used to determine solute rejection of the membranes. A 1 g/L

solution of BSA was prepared in a phosphate buffered saline (PBS) to maintain the pH at 7.4. During solute rejection measurements, the retentate solution was continuously stirred at 400 rpm using a magnetic stirrer to avoid buildup of a boundary layer. The concentration of BSA in the filtrate was determined by measuring the absorbance values at 280 nm with a Cary 5G UV-Vis-NIR spectrophotometer. The determination of the protein concentration is based on Beer-Lambert law which implies that the absorbance linearly depends on the analyte concentration. Figure 3.7 (b) shows a calibration curve obtained by measuring the absorbance values for solutions of known protein concentrations. The unknown protein concentration can be easily determined by measuring the absorbance, and using the plot below to back out the concentration.

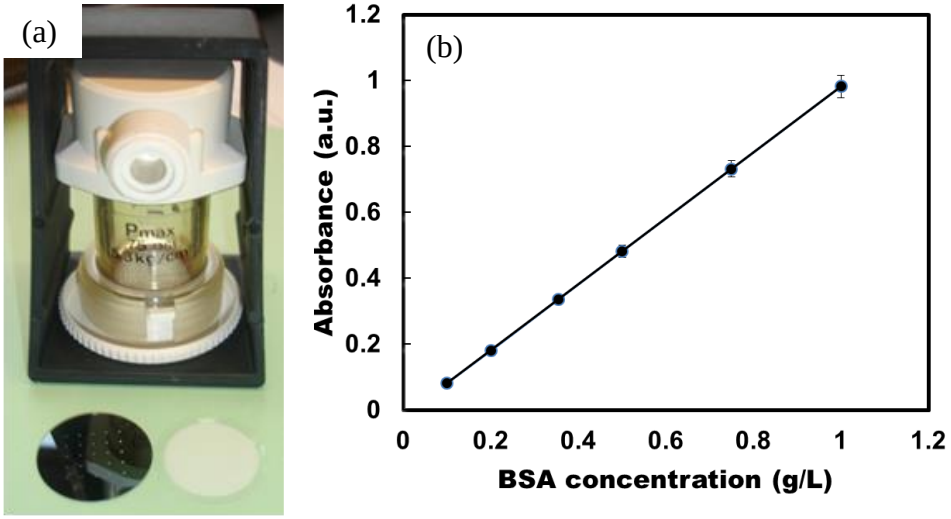


Figure 3.7: (a) Stirred ultrafiltration cell used for characterizing membrane flux and solute rejection (b) Absorbance plotted as a function of concentration of bovine serum albumin (BSA).

3.3.2 Ellipsometry

Ellipsometry is a non-contact and non-destructive film characterization technique that can measure optical properties and film thickness with high precision and sub-Angstrom level accuracy. Figure 3.8 shows a typical configuration of an ellipsometer[38]. When polarized light

is obliquely reflected from a sample, the incident and reflected beam defines the plane of incidence. The p- plane corresponds to a plane parallel to the plane of incidence of light, whereas the s-plane corresponds to a plane perpendicular to the plane of incident light.

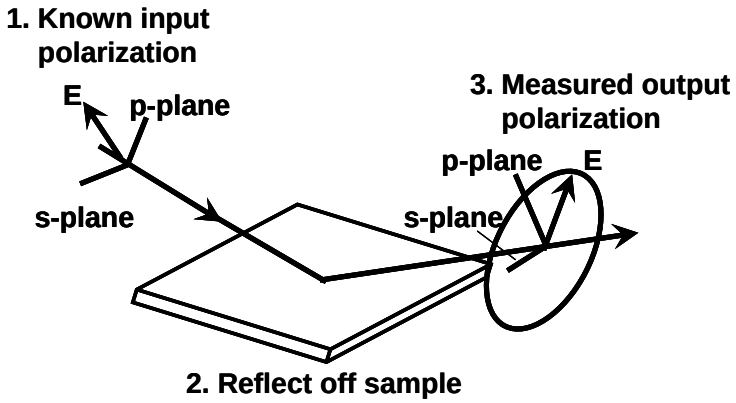


Figure 3.8: Typical ellipsometer configuration. Ellipsometer measures change in polarization of light to determine film thickness and optical properties. Figure adapted from J. A. Woollam Co[38].

In ellipsometry, the measured values are expressed as psi (Ψ) and delta (Δ). These measured values are related to the complex reflectivity ratio of p- and s- polarized light according to Equation 3.2. Here, $\tan(\Psi)$ is the magnitude of the complex reflectivity ratio, and Δ is the phase difference between the p- and s- reflected light.

$$\frac{R_p}{R_s} = \tan(\Psi)e^{i\Delta} \qquad (3.2)$$

Thin film measurements in this study were carried out in J. A. Woolam Co. Inc. WVASE 32 system. For all the measurements, the angle of incidence was kept fixed at 70 °, and a Cauchy model was used to extract the optical constants. The Cauchy model (Equation 3.3) was used to describe the refractive index of films as a function of wavelength. This model assumes that the

film is non-absorbing or transparent, and that the refractive index only consists of a real component, with extinction coefficient '*k*' being equal to 0.

$$n(\lambda) = A + \frac{B}{\lambda^2} + \frac{C}{\lambda^4} \qquad (3.3)$$

For aluminum oxide (Al_2O_3) films, measurements were taking over a wavelength range of 300-1300 nm, whereas for TiO_2 films a smaller spectral range of 450-1300 nm was employed. The band gap of TiO_2 is ~ 3 eV, and these films show absorption for wavelengths less than 450 nm. The thickness of the octadecyltrichlorsilane (OTS) self-assembled monolayers (SAM) was analyzed by using a three layer Cauchy model ($Si/Al_2O_3/OTS$). Before adding the OTS layer, the aluminum oxide- coated silicon wafers were characterized to predetermine thickness and the optical constants of the Al_2O_3 layer. For determining OTS thickness, the properties of the Al_2O_3 films were fixed at the measured values, and the refractive index of the OTS film was assumed to be constant (n =1.465) at a wavelength of 580 nm.

3.3.3 Scanning Electron Microscopy

Scanning electron microscopy uses interaction of a focused electron beam with matter to create a magnified image of the specimen. SEM can be operated in different imaging modes which use different signals to image the sample. Signals from secondary electrons, backscattered electrons and x-rays can be detected to form an image of the specimen. For all the samples analyzed in this work, secondary electron imaging (SEI) mode was used. Secondary electrons are low-energy electrons, and are produced by inelastic collision of the incident electron beam with the specimen atoms. The SEI mode is especially useful for resolving fine surface topographical details as the secondary electrons are produced close to the specimen surface.

In this work, JEOL JSM7000F field emission scanning electron microscope (FESEM) was used to measure pore openings of the TE membranes before and after modification. The TiO_2-and Al_2O_3- modified TE membranes required prior coating with gold to reduce surface charging. The Al- coated TE membranes did not show any charging, and hence, these samples were not modified in any way before imaging. The samples were studied at an accelerating voltage of 2 kV and a working distance of 10 mm. Deposition profiles on patterned holes and trenches were studied using cross-section SEM. The features were cleaved using a scribe just before imaging to avoid damaging and distorting the features.

3.3.4 Contact Angle Measurement

Contact angle measurements provide a quick and easy method for evaluating effects of different surface functionalization treatments. Figure 3.9 shows the apparatus built in our laboratory for measuring contact angles of different surfaces[39]. The apparatus consists of a Canon Powershot camera, with an optical zoom of 9X, for taking images of the water drop. An

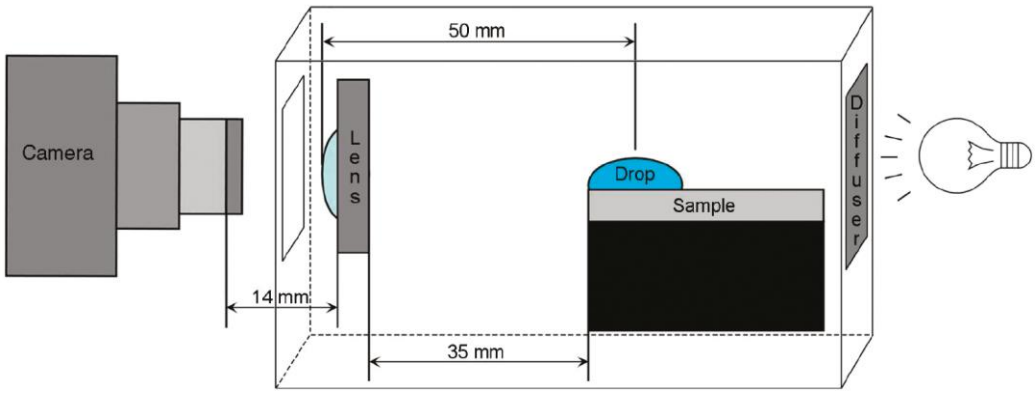


Figure 3.9: Schematic of the contact angle measurement apparatus. Reprinted with permission from [39]. Copyright (2010) American Chemical Society.

optical lens with a focal distance of 50 mm is placed between the camera and the sample. A lamp is placed behind the sample to make the water droplet appear black, and improve accuracy during image processing. A 2.5 µL drop is introduced on the sample surface through a microliter syringe. The image is then analyzed in ImageJ using a Contact angle plugin developed by Brugnara. This plugin applies a circular or elliptical approximation to the drop profile to calculate the contact angle.

Figure 3.10 shows the capability of our apparatus to analyze highly hydrophilic and hydrophobic surfaces. Figure 3.10 (a) shows a water drop on a surface cleaned with UV-Ozone treatment and Figure 3.10 (b) shows a drop on a surface modified with a monolayer of octadecyltrichlorsilane (OTS).

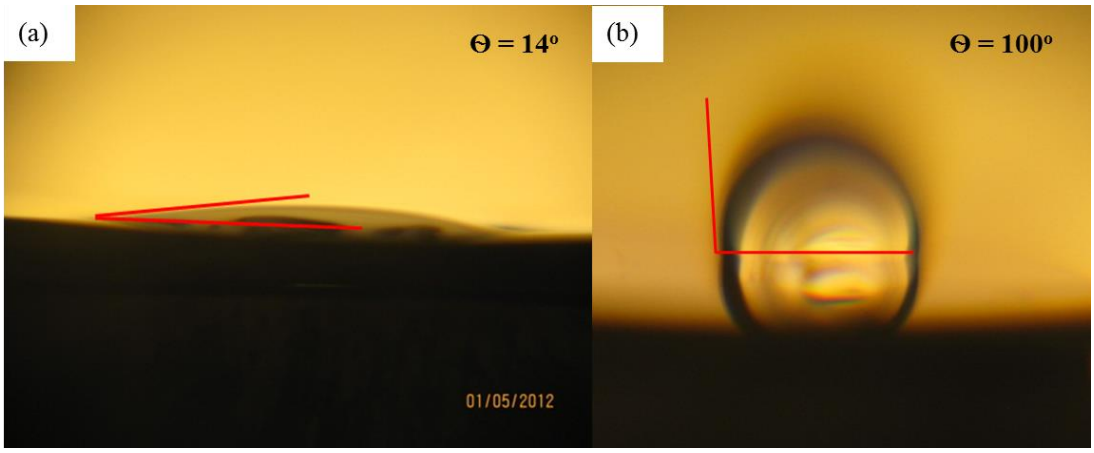


Figure 3.10: Liquid droplet on a (a) Surface cleaned with UV-Ozone treatment (b) Aluminum oxide surface coated with self-assembled monolayer (SAM) of octadecyltrichlorosilane (OTS).

It has been previously shown that the non-dimensional contact angle, which is the ratio of the contact angle at any time to the saturation contact angle value, is a close approximation of the fractional surface coverage[40]. Thus, the kinetics and thermodynamics of any surface modification process like silanation can be quantified using contact angle measurements.

CHAPTER 4

FEATURE SCALE MODELING OF STEADY STATE- AND TRANSIENT-DEPOSITION PROCESSES

The following is a reproduction of a paper published in the Journal of Vacuum Science and Technology B. Volume 32, Issue 5, pp. 1-8, 2014. This chapter is reproduced as published except that section numbers, references, and figure labels were changed to conform to the thesis format.

Feature Scale Modeling of Pulsed Plasma-Enhanced Chemical Vapor Deposition

Sanket S. Kelkar and Colin A. Wolden
Department of Chemical and Biological Engineering, Colorado School of Mines, Golden, CO 80401

Abstract

A two dimensional feature scale model has been developed to predict film profile evolution during pulsed plasma enhanced chemical vapor deposition (PECVD). The model employs a diffusion reaction framework with a spatially variable Knudsen diffusion coefficient to account for molecular transport in evolving feature geometries. The transient model accounts for the alternating atomic layer deposition (ALD) and PECVD growth modes that contribute to deposition. A scaling analysis is used to account for diffusion limitations that affect the ALD component in high aspect ratios due to insufficient precursor exposure. The model predictions have been validated using cross section micrographs of nanostructures produced by pulsed PECVD of aluminum oxide on patterned substrates. The model provides a tool to design the fabrication of nanostructures with digital precision. By varying the relative contributions of the

* Electronic mail: cwolden@mines.edu

two modes pulsed PECVD provides an opportunity engineer the degree of conformality to produce unique morphologies that are distinct from either steady state vapor deposition processes or conventional ALD.

4.1 Introduction

Deposition techniques that form structures with nanoscale precision are important tools for enabling nanotechnology[41, 42]. One example is nanopore fabrication, which is of great interest for applications ranging from ionic transistors[6, 43, 44] to the sequencing of DNA molecules[4, 45]. Nanopores can be fabricated with great precision using high energy beam techniques[1, 3], however these techniques are costly, time-consuming and not easily scaled. An alternative approach is to begin with a template with features on the order of 100 nm patterned by conventional means, followed by the use of vapor deposition techniques to reduce the pore size into the nanopore regime (< 10 nm)[6]. The most common approach for this latter step has been atomic layer deposition (ALD), which provides digital control over the amount of material deposited[43, 46, 47]. However a drawback of ALD is that the required times for both precursor exposure and purging can become excessive, particularly when using patterned substrates[25]. Moreover, conformal ALD leads to densification of the pores, which dramatically attenuates flux in membrane applications[46]. Pulsed plasma enhanced chemical vapor deposition (PECVD) is a possible alternative to ALD for reducing the pore size in model supports while maintaining a high degree of porosity, but this deposition technique is not perfectly conformal and as such control of the final nanostructure is more complicated. In this work we develop feature scale modeling tools to predict and design the fabrication of nanostructures such as asymmetric nanopores.

Our group has developed pulsed PECVD as an alternative to ALD for self-limiting growth of metal oxide thin films[26-28, 30]. In pulsed PECVD a metal precursor and molecular oxygen are supplied continuously, and the plasma is modulated between on and off states at low frequency (~ 1 Hz). Under proper conditions the process is self-limiting and digital control is achieved (i.e. ~1-10 Å/pulse). The continuous delivery of the reactants and the elimination of the purge steps leads to considerably higher net growth rates[24]. The deposition mechanisms involved in pulsed PECVD, discussed in detail in earlier reports[25, 29], are reviewed briefly here. There are two potential contributions to film growth in this technique. The first mode is analogous to plasma–assisted ALD in that the precursor adsorbs onto the surface during the plasma off step, followed by conversion to oxide during the plasma exposure step. The second growth mode is due to the contribution of highly reactive species produced at plasma ignition. The magnitude of the PECVD mode can be adjusted by controlling the density of the precursor present at plasma ignition, and consequently the total growth per cycle (GPC) can be adjusted over a wide range (1 – 10 Å/pulse)[25]. As shown in this work the ability to vary the relative contributions of the ALD and PECVD growth modes leads to opportunities to engineer the level of conformality and design nanoscale morphologies that are distinct from those produced by typical steady state vapor deposition processes or conventional ALD.

In previous work it was shown that the PECVD mode primarily contributes to deposition on the planar surface, making only minor contributions to deposition within high aspect ratio features[24]. As a consequence, pulsed PECVD naturally leads to the formation of asymmetric nanopores, since the pore opening is closed faster than its interior. There are several potential benefits of asymmetric nanopores over uniform pores that would be produced by ALD. Asymmetric nanopores have been shown to demonstrate ion current rectification behavior and to

act as diodes[5]. This property can be potentially exploited in many applications such as ion pumping and information processing[48], protein sensors[49], and detection and sequencing of DNA[4]. In addition, membranes employing asymmetric nanopores can provide high selectivity for nanoscale compounds without compromising flux. As mentioned before, pulsed PECVD has been demonstrated to deliver digital control over deposition on planar surfaces. However, when extending this technique to patterned substrates the resulting morphologies will depend on the specific feature geometry and the deposition conditions employed. The goal of this work is to develop and verify a transient feature scale model that is capable of predicting film conformality in pulsed PECVD.

There is extensive literature on feature scale modeling of steady state processes like CVD and PVD[50-53]. Feature scale models are typically classified by their treatment of gas transport. Line of sight models are based on the solution to the Boltzmann equation, and film growth occurs by particles striking the surface and sticking to it. The high dimensional integro-differential Boltzmann equations can be solved numerically[54, 55] or by using Monte Carlo methods[56, 57]. The resulting profiles are characterized by a parameter known as sticking coefficient (γ)[50], which is the ratio of the surface reaction rate to the molecular flux. The sticking coefficient can be arbitrarily selected to fit the deposition profile[58] or can be evaluated from a known reaction chemistry[54]. The second approach is known as diffusion reaction model (DRM) and is based on continuum-like treatment of transport in the gas phase[32, 33, 51]. In this approach, the molecular flux is given by the product of the diffusion coefficient and the concentration gradient[32]. Film growth takes place as a result of heterogeneous reactions taking place on the feature surface. DRM is computationally less intensive and hence, we employ this approach in our investigations.

In this work a 2-D diffusion reaction model developed in COMSOL is used to predict deposition profile evolution for both conventional steady state as well as pulsed PECVD processes. The steady state model is discussed first, and its inclusion in this study serves two purposes. First, our pulsed PECVD model employs the same methodology and the same set of assumptions as those used in the steady state model. Second, steady state models have been developed extensively and provide a good metric for verifying our model and providing references for comparison with pulsed PECVD profiles. The transient pulsed PECVD model alternates between PVD and ALD contributions to film growth, reflecting the physical nature of the process. Exposure limitations that impact the ALD component are treated by evaluating the local aspect ratio as the profiles evolve. We explore the dependence of deposition profile on the relative contributions of the PECVD and ALD components during deposition. Furthermore, the model predictions are validated by comparisons with experimental profiles obtained from deposition on patterned contact holes and trenches.

4.2 Modeling

Figure 4.1 shows the computational domain and boundary conditions for the geometry employed in our model. We consider symmetric 2-D features such as trenches and contact holes and hence, only half of the geometry is shown in Figure 4.1. This geometry includes a bulk domain above the feature, which represents the stagnant boundary layer above the substrate. Figure 4.1 displays the base case feature used in this work which is a cylinder with a radius (R) of 50 nm and a height (H) of 400 nm. The feature volume is resolved by using an extremely fine mesh whereas the boundary layer is resolved by using a coarser mesh. The profiles are largely insensitive to the height or the radius of the bulk domain, but for consistency, these values were

fixed at 800 nm and 250 nm respectively in all simulations. Fillets have been applied to the sharp corners to avoid any mesh distortion during film growth.

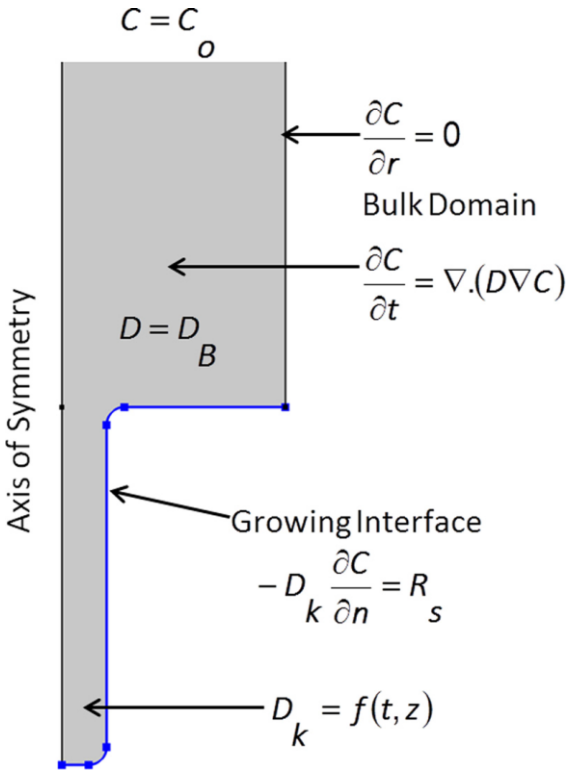


Figure 4.1: Computational domain showing half of a cylindrical cross-section (Initial Radius = 50 nm, aspect ratio = 4) with governing equations and boundary conditions. Film growth occurs on the surface of the feature, highlighted in blue.

4.2.1 Modeling of Steady State Processes

The overall physics of steady state models has been developed and reviewed in earlier studies[32, 33, 59] and is summarized below. Due to the small size of our feature, transport by convection is insignificant within the computational domain, and mass transport occurs only through diffusion. In addition, we assume that homogeneous gas phase reactions contribute

negligibly to the consumption of the reactive species. Under these assumptions the mass balance reduces to

$$\nabla.(D\nabla C) = \frac{\partial C}{\partial t} \qquad (4.1)$$

where C is the concentration of the reactive species and D is the diffusion coefficient.

We employ a time- and position-dependent diffusion coefficient (D) in this study. For Kn <<1, D is given by the continuum value D_B which is the value used in the bulk domain above the feature. Equation 4.2 is derived from kinetic gas theory[32] and is used to calculate D_B.

$$D_B = \frac{1}{3} v_m \lambda \qquad (4.2)$$

where v_m is the mean molecular speed and λ is the mean free path. In this work these parameters are evaluated for a dilute mixture of trimethylaluminum (TMA) in oxygen and argon, which reflect the experimental conditions used for deposition.

In pulsed PECVD, the operating pressures (P) are typically less than 1 Torr and the characteristic feature size employed for the base case is about 100 nm. The mean free path at this operating pressure is > 10 μm and as such the Knudsen number (Kn) in the pores is >>1. In the Knudsen or molecular flow regime, collisions between gas molecules and the feature surface dominate over inter-molecular collisions. The Knudsen diffusion coefficient (D_k) in this flow regime was evaluated as a function of the instantaneous local feature dimension that varies with position (z) and time (t) as the pore opening constricts due to material deposition. For simplicity, the height (H) of the feature is assumed to be unchanged during deposition, and the Knudsen diffusion coefficient was evaluated using the following expression[33].

$$D_k(z) = \left\{ \frac{20 + 8\left(\frac{H}{2R(z)}\right)}{20 + 19\left(\frac{H}{2R(z)}\right) + 3\left(\frac{H}{2R(z)}\right)^2} \right\} \frac{H}{4} v_m \qquad (4.3)$$

The boundary conditions are highlighted in Figure 4.1. At the top of the domain the concentration is fixed at C_0. Symmetry is imposed along the center line. Another assumption is that pores are isolated and deposition environment in any feature is unaffected by the deposition in adjacent features. This assumption gives rise to an insulating boundary condition on the sidewall.

$$\frac{\partial C}{\partial r} = 0 \qquad (4.4)$$

The reactive surface is highlighted in blue in Figure 4.1. The transport of reactive species by diffusion results in film growth by heterogeneous surface reaction, which is assumed to be first order in the reactive species.

$$J = -D\frac{\partial C}{\partial n} = k_s C \qquad (4.5)$$

where the rate constant (k_s) was evaluated using gas collision theory and a sticking coefficient formulation.

$$k_s = \gamma \sqrt{\frac{kT}{2\pi m}} \qquad (4.6)$$

For the PVD growth mode the value of γ was set to unity, while for the ALD mode this value was made sufficiently small to ensure perfect conformality as described below.

The transport and reaction equations described above were solved to extract the local deposition rate, which is represented by the mesh extension velocity (v). The mesh extension velocity is governed by the surface reaction rate as shown in Equation (4.7). The moving mesh tracks the evolving film profile.

$$v = (k_s C).V_m \qquad (4.7)$$

where V_m is the molar volume of the deposited material. Equation (4.7) is utilized in our boundary movement model to simulate the deposition profile at different time intervals. There are many approaches like level set method[34] and string/segment based algorithms[60] which have been used to simulate profile evolution in micro-fabrication techniques. We employ an arbitrary lagrangian eularian (ALE) scheme for surface propagation. ALE attempts to combine the merits of Lagrangian and Eularian schemes while minimizing their shortcomings[61]. As compared to other algorithms, ALE is computationally less intensive and allows for accurate evolution of deposition profile through pore closure. Another advantage of ALE is that it gives us the flexibility of using mesh smoothing algorithms to minimize distortion of the profile[61]. As such the evolving feature geometry was periodically re-meshed to avoid any mesh distortion.

The model equations described above can be written in dimensionless form to extract important parameters which govern the conformality or step coverage (SC) in LPCVD. For a given geometry and a first order heterogeneous surface reaction, the SC depends on a single dimensionless parameter known as the step coverage modulus (ϕ) [33]. The step coverage modulus ϕ describes the ratio of surface reaction rate to the mass transfer rate by diffusion. For a cylindrical feature, ϕ is expressed as

$$\phi = \frac{2k_s H^2}{RD_{k0}} \qquad (4.8)$$

where D_{k0} is the initial Knudsen diffusion coefficient evaluated at the entrance to the feature.

Figure 4.2 displays the profiles obtained for steady state deposition as a function of ϕ. Here we display the two limits that correspond to the profiles expected in ALD and PVD respectively, as well as an intermediate example that one might observe in a steady state CVD process. Profiles for values of $\phi \leq 0.022$ (Figure 4.2 (a)) are perfectly conformal, characteristic of ALD. Ganguli *et al*., have showed that the surface reaction rate should be very small, roughly $5*10^{-4}$ times the diffusion flux, for voidless filling of a trench with aspect ratio of 3 [32]. Similarly, we find that surface reaction rates < $5*10^{-4}$ times the incident flux (as predicted by kinetic theory of gases) is sufficiently low for conformal coating of the features discussed in this work. This step coverage modulus is used below to simulate the ALD component of the pulsed PECVD process, denoted as ϕ_{ALD}. Figure 4.2 (b) displays a profile obtained at the intermediate value of ϕ = 4.4, which is characteristic of a steady state CVD profile with γ = 0.1. As the value of ϕ is increased the deposition profiles become progressively non-conformal. This is in agreement with previous reports, where a large value of step coverage modulus is found to result in sharp concentration gradients and hence, non-uniform deposition profiles[33]. Figure 4.2 (c) shows the other extreme, ϕ = 44.3, corresponding to the case of PVD in which γ = 1. This case is a suitable approximation of the PECVD growth mode. During plasma ignition, the precursor is converted into highly reactive intermediate species. These species stick to the surface and contribute to film growth in a process analogous to PVD. In the profile simulations described

below, we refer to the contribution to deposition by radicals produced at plasma ignition as the 'PVD' growth mode, and characterize it by a step coverage modulus of ϕ_{PVD} .

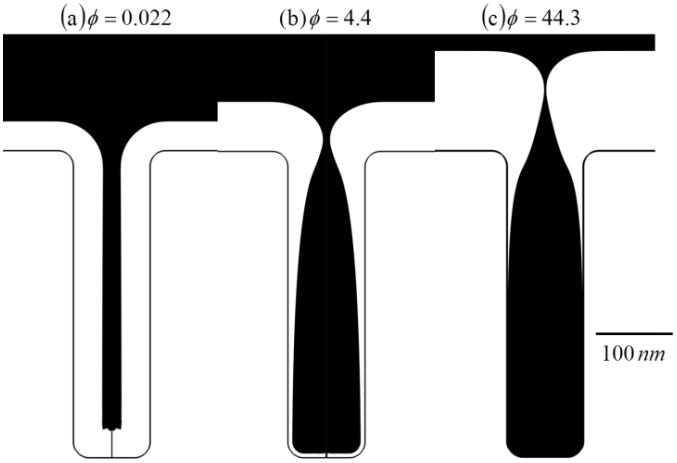


Figure 4.2: Steady state profiles on a cylinder (Initial opening = 100 nm, aspect ratio = 4) simulated as a function of step coverage modulus (ϕ) for conditions characteristic of (a) ALD, ϕ = 0.022; (b) CVD, ϕ = 4.4; and (c) PVD, ϕ = 44.3.

4.2.2 Modeling of Unsteady State Pulsed PECVD Process

As discussed above, deposition in pulsed PECVD proceeds through alternating ALD and PVD contributions to film growth. Figure 4.3 displays a schematic diagram outlining the modeling approach used to simulate profile evolution during pulsed PECVD. Initially, a coating with a planar thickness of T_{ALD} is applied to our model support using the ALD step coverage modulus (ϕ_{ALD}) described above (Figure 4.2 (a)). This step is followed by the subsequent deposition of material up-to a planar thickness of T_{PVD} that is simulated using the PVD step coverage modulus (ϕ_{PVD}, Figure 4.2 (c)). This process is repeated for the desired number of cycles to produce the appropriate planar thickness. The ratio of the two growth modes, $R = T_{PVD} / T_{ALD}$, is an adjustable parameter that may be determined experimentally by comparing the GPC

obtained under pulsed PECVD with the GPC measured during plasma-assisted ALD[24, 25]. The transport and the boundary movement model employ the same methodology as described above for the steady state model.

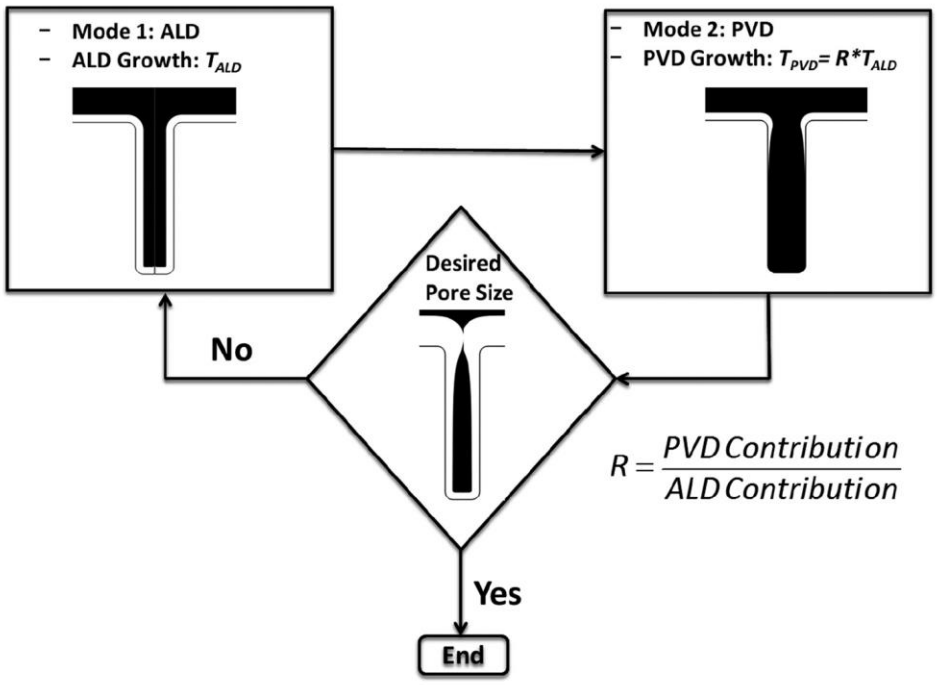


Figure 4.3: Block diagram of pulsed PECVD modeling approach. The model alternates between ALD and PVD modes till the desired planar thickness is achieved. '*R*' is the ratio of the two growth modes which is the adjustable parameter in the unsteady state pulsed PECVD model.

The approaches described above was implemented using COMSOL 4.3b, a finite element solver and simulation software. 2D Cartesian or axisymmetric geometries were employed as appropriate that were partitioned with a user defined mesh using 2500 triangular mesh elements for the base case geometry described here. The model was constructed using the physics modules titled "transport of diluted species" and "moving mesh" using the "time dependent" study option. A complementary 1D model was simultaneously employed to track the evolving pore radius *R(z)* as a function of time using the general projection and general extrusion operators in COMSOL.

The spatially variable Knudsen diffusion coefficient was implemented as a user defined expression that was a function of *R(z)*. At each time step, the moving mesh interface utilizes the concentration profile produced by the transport of diluted species' module to modify the feature geometry according to the surface reaction rate equation. As the features evolved, the geometry was periodically remeshed to prevent instabilities that arise due to mesh distortion.

4.3 Results and Discussion

Figure 4.4 displays simulated profiles for pulsed PECVD as a function of the PVD/ALD ratio *R*. As expected, the profiles become increasingly non-conformal as *R* is increased. In these simulations, material deposited at the base of the pore is almost exclusively due to ALD, while deposition on the surface and near the feature opening includes contributions from both ALD and PVD growth modes. An interesting observation is that as *R* is increased the amount of planar deposition required to close the feature also increases. An implicit assumption in our model is that the duration of the plasma off step during pulsed PECVD process is sufficiently long to allow the precursor to fully diffuse to the bottom of the feature and adsorb. Likewise, it also assumes that the duration of plasma on step is sufficiently long for atomic oxygen to diffuse through the feature and complete the other ALD half reaction. This is a good assumption for the majority of conditions evaluated in this work. However, this "sufficient exposure" assumption can fail in the case of very high aspect ratios that occur when the feature opening $\rightarrow 0$ and the aspect ratio of the feature $\rightarrow \infty$. Under these conditions the ALD contribution to growth is no longer uniform due to diffusion limitations as well-documented in the ALD literature[36, 62-64]. The practical consequences and our treatment of this issue are discussed below in more quantitative detail.

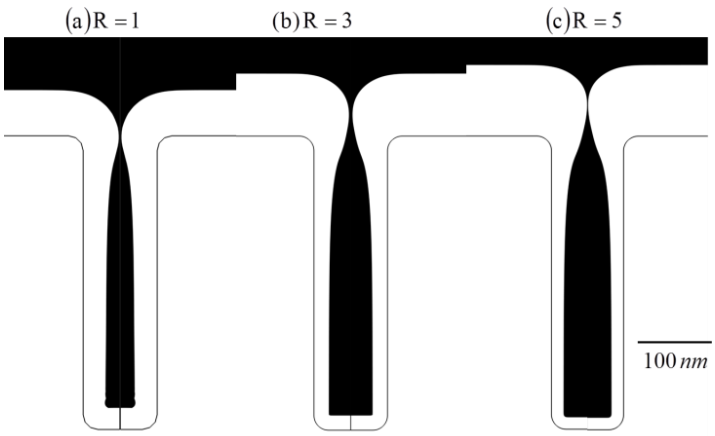


Figure 4.4: Comparison of pulsed PECVD profiles on a cylinder (Initial opening = 100 nm, aspect ratio = 4) as a function of PVD/ALD ratio for (a) R = 1; (b) R= 3; and (c) R = 5. 'R' values employed for these simulations reflect the typical operating conditions in pulsed PECVD.

Typical GPC values in pulsed PECVD are 1-10 Å /pulse, and experimentally it takes hundreds of cycles to close a 100 nm feature. To accelerate the simulations the sensitivity of the

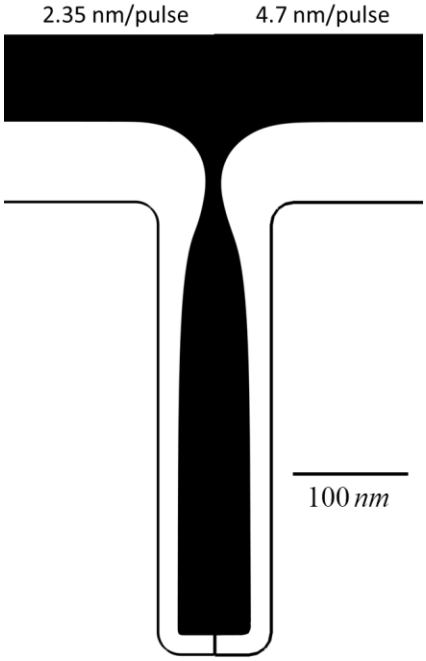


Figure 4.5: Comparison of deposition profiles on a cylinder (Initial opening = 100 nm, aspect ratio = 4) obtained at *R* = 3 simulated using GPC values of 2.35 nm/pulse (left) and 4.7 nm/pulse (right). Model GPC values < 5 nm/pulse were found to be sufficiently small to significantly reduce the computation time without compromising on the integrity of the final deposition profile.

profiles to the magnitude of the GPC value used in the simulations was investigated. For example, a profile at $R = 3$ could be simulated using T_{PVD}/T_{ALD} values of either1 and 3 Å/pulse or 1 and 3 nm/pulse. While the former is representative of the experiment, the latter has the advantage that it affects the ultimate resolution and at some point it can impact the accuracy of the results. For the 100 nm features simulated in this work it was found that using GPC values < 5 nm/pulse were sufficient to maintain the integrity of the final profile. Figure 4.5 displays a side by side comparison of profiles at $R = 3$ where the simulated GPC was 2.35 and 4.7 nm/pulse, respectively. As no difference was observed this was judged to be sufficient. Alternatively the GPC could be adjusted adaptively as the profile evolves to accurately capture sub-nanometer features.

As shown in Figures 4.2 (b) and (c), steady state deposition techniques typically lead to tapered profiles, with little or no deposition at the base of the feature. ALD, on the other hand, (Figure 4.2 (a)) results in a layer of consistent thickness throughout the feature. Pulsed PECVD produces feature profiles that are essentially a superposition of the ALD and PVD profiles. The deposition in the bottom half of the feature is characterized by a layer of consistent thickness similar to ALD whereas the profile near the feature opening is more characteristic of the PVD profile. However, the pulsed PECVD profiles shown in Figure 4.4 are distinct from the steady state processes, and cannot be represented by a single value of γ or ϕ.The PVD/ALD ratio provides an extra degree of freedom which can be used to engineer the level of conformality. Like ALD, pulsed PECVD offers digital control over planar film growth, but the modeling tools described here are required for the design of nanostructured features. For example, if one wants to create a 10 nm opening from a 100 nm feature using ALD, that simply requires the application of the number of cycles required to deposit 45 nm of material. In contrast, for pulsed PECVD

the amount of material required depends on the PVD/ALD ratio employed. For the case considered here the planar thickness required to produce a10 nm opening increases from 60 to 78 to 85 nm for *R* values of 1, 3, and 5, respectively.

Simulated profiles were compared with SEM micrographs obtained from both cylindrical holes and trenches. Figure 4.6 compares the cross-section SEM micrograph of a nanopore fabricated by pulsed PECVD of alumina with the model. The initial feature is a cylinder with concave sidewalls, and the initial and final geometries have been highlighted in Figure 4.6 for clarity. The initial opening is around 125 nm and the height of the cylindrical feature is around 770 nm. Approximately 80 nm of aluminum oxide was deposited onto the surface using a PVD/ALD ratio of R =1, resulting in a final pore opening of ~10 nm. The model approximation of the initial geometry and the final geometry is also shown. The left half section shows the simulated profile for sufficient exposure assumption. The simulation on the right half section accounts for ALD exposure limitation encountered experimentally, the details of which will be discussed momentarily. In general, the basic modeling approach does a very good job of capturing the experimental results observed for this relatively complex feature. The predicted deposition profile is slightly more rounded in comparison to the experimental feature. We fillet sharp corners in the starting geometry in our simulation to ensure convergence, and this leads to artificial rounding near the pore mouth. This introduces a slight discrepancy in our modeling result and the experimental profile but does not impact the broad message of this study. As we move down the pore, however, there is very good quantitative agreement near the middle of the feature, but the model slightly over-predicts the film thickness near the pore bottom. The predicted thickness of the aluminum oxide layer at both the midpoint and the bottom of the cylinder was found to be ~ 38 nm. This indicates that deposition in the bottom half of the feature

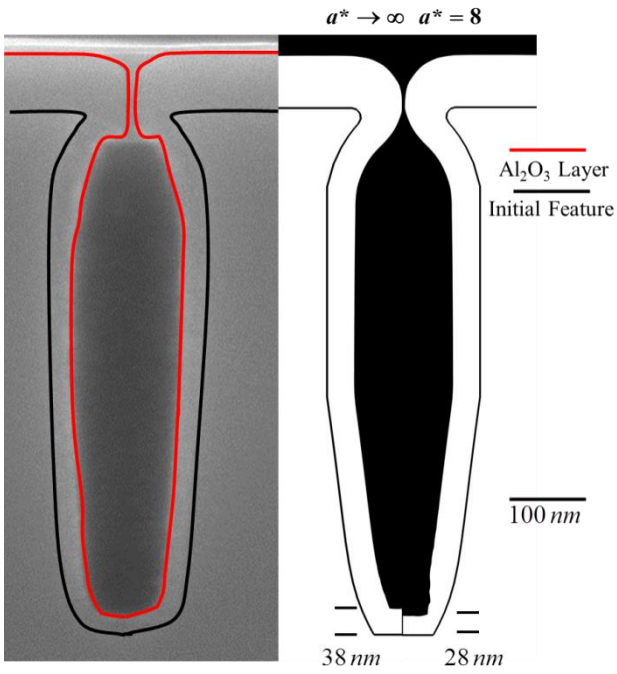


Figure 4.6: Comparison of experimental (left) and simulated (right) profiles obtained from a cylindrical feature coated by pulsed PECVD of alumina under conditions where R = 1. The initial opening is around 125 nm and the height of the cylindrical feature is around 770 nm. Final pore opening ~ 10 nm is achieved by deposition of 80 nm aluminum oxide layer using PVD/ALD ratio of R =1. The left half of the simulated profile was obtained using the sufficient exposure assumption whereas the right half accounts for the exposure limitations present during the experiment. The two profiles are very similar with exception of the base of the feature. The black and red curves in the experimental SEM are provided to highlight the initial feature and the final deposition profile, respectively.

occurs through ALD and that the contribution of the PVD growth mode in this region is negligible. Experimentally the Al_2O_3 thickness at the midpoint and bottom are estimated to be 36 nm and 28 nm, respectively. The difference between the model and experiment near the pore bottom is attributed to the limited validity of the sufficient exposure assumption discussed above. As the aspect ratio increases the plasma off times employed experimentally became insufficient to provide the required reactant exposure throughout the depth of feature, and as a consequence the model over-predicts the ALD contribution. Next, our approach to address exposure

limitations is discussed and demonstrated for conventional ALD and in the pulsed PECVD modeling.

There are many reports available in the literature which model the conformality of atomic layer deposition inside high aspect ratio features[36, 65-67]. Gordon and coworkers[36] developed scaling relationships based on simple kinetic models to predict the minimum exposure needed to conformally coat high aspect features as a function of the exposure required to coat planar surfaces. This model was extended by Dendooven and coworkers, who assumed a variable sticking probability based on a Langmuir surface coverage mechanism[67]. Adomaitis further developed a multiscale ALD model in which Knudsen transport through nanopores was coupled to a detailed kinetic Monte Carlo ALD growth model[65]. Subsequently, the continuum-like transport model was replaced by a rigorous ballistic transport model based on the direct solution to the integro-differential Boltzmann equations[66]. Here we adopt an approach based on Gordon's scaling relationships, which has the advantage that it does not require knowledge of the detailed kinetics which are unknown for most ALD processes.

Figure 4.7 plots the exposure requirements as a function of aspect ratio (a) for an ideal ALD precursor such as TMA that requires just a few Langmuirs (L) of exposure to fully saturate a planar surface[36]. The horizontal lines in Figure 4.7 indicate the TMA exposure used experimentally during the fabrication of the nanostructures shown in Figures 4.6 and 4.9. The intersection of these line with the solid curve indicates the critical aspect ratio (a^*) that can be accurately simulated using our basic modeling assumptions. We employ a simple approach to incorporate exposure limitations into the feature scale simulations. During the simulations a local aspect ratio a(r, z) is calculated at each time step as the profile evolves. Once the local aspect ratio exceeds the critical a^* value the ALD component is terminated.

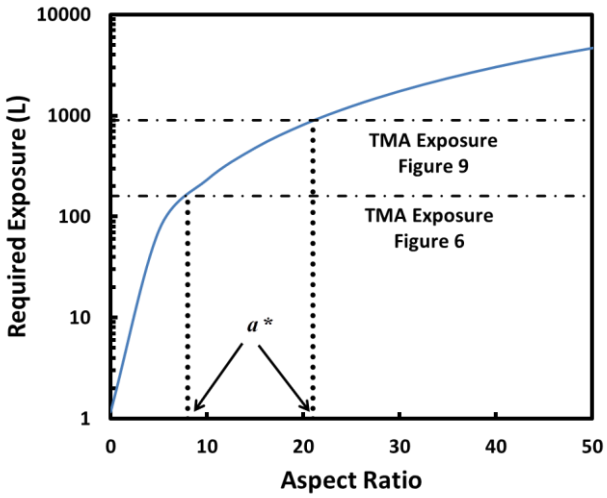


Figure 4.7: A plot of minimum reactant exposure required to conformally coat a feature as a function of aspect ratio. Horizontal lines indicate the experimental TMA exposure employed during the fabrication of the structures shown in Figures. 4.6 and 4.9, respectively.

Figure 4.8 displays the ALD profiles obtained on our base feature (initial aspect ratio = 4) for a^* values of 2, 4, 6 and ∞ respectively. ALD deposition under exposure limitations produces features that are conformal to a point, followed by a linear gradient to the point where growth terminates. For $a^* = 2$, there is no deposition in the bottom ½ of the feature whereas at $a^* = 4$ deposition extend the length of the pore wall but no deposition is observed at the base. When a^* exceeds the initial feature aspect ratio a conformal layer coating is obtained until this value is exceeded ($a^* = 6$), where the $a^* \rightarrow \infty$ case illustrates the perfect conformality achieved under the sufficient exposure assumption. These profiles illustrate how underexposed ALD may be engineered to produce asymmetric nanopore features.

Returning to Fig. 4.6 the exposure used experimentally corresponded to a critical aspect ratio of ~8 (Figure 4.7). The right half profile in Figure 4.6 was obtained by integrating $a^* = 8$ into the ALD component of the feature simulation. Comparison of the two shows that the

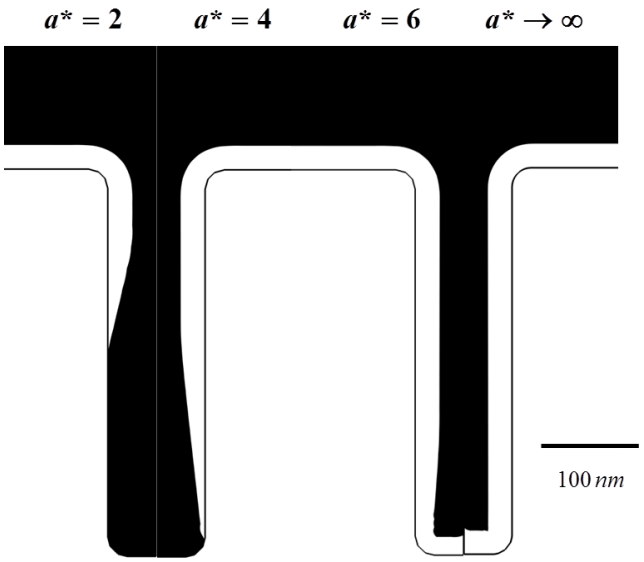


Figure 4.8: Comparison of ALD profiles on a cylindrical feature (Initial opening = 100 nm, aspect ratio = 4) as a function of the critical aspect ratio (a^*). $a^*$is determined from the precursor exposure using scaling relationships developed by Gordon and coworkers. $a^* \to \infty$ case is a representation of the sufficient exposure assumption.

deposition profile near the pore mouth is essentially unchanged for both the simulations. The thickness at the midpoint is ~ 38 nm and compares favorably with both previous model predictions and the experimental profile. Due to the concave shape of our initial feature, the local aspect ratio values near the mouth and the middle of the feature do not exceed a^* value even when the pore mouth is almost completely closed. However, the inclusion of the exposure limitations become evident in the bottom half of the feature. The modified model predicts a film thickness of 28 nm at the base which agrees very well with the experimental value. The simple strategy employed here is a computationally simple and effective for handling such exposure limitations that eventually arise.

The examples described above have employed cylindrical geometries, however the framework may be readily extended to 2D Cartesian geometries. Figure 4.9 compares the SEM and simulated profile of a trench coated by pulsed PECVD[24]. The feature employed here is a 6

μm deep trench with a ~700 nm opening that tapers linearly to ~450 nm at the base. As in the previous experiment *R*= 1, indicating that the contributions of the ALD and PVD components were identical. The simulation was run to match the experimentally measured planar thickness of ~240 nm. Transport within the trench employed the appropriate geometry-dependent description of the Knudsen diffusion coefficient available in the literature[32]. Other details of the simulation were the same as described above. As before the PVD contribution is attenuated

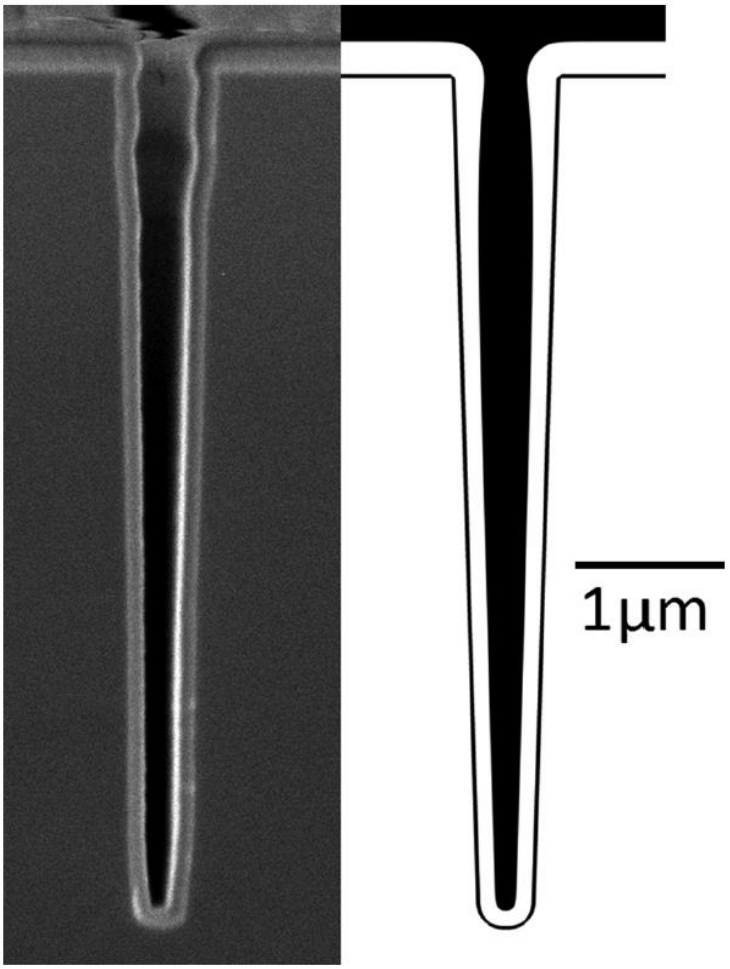


Figure 4.9: Comparison of experimental and simulated deposition profiles in a trench. The trench is 6 μm deep and shows a taper with top width ~ 700 nm and bottom width ~ 450 nm. Aluminum oxide layer with a planar thickness of 240 nm was deposited during the filling process. The contributions of the PVD and ALD components were identical, and hence, PVD/ALD ratio of *R* =1 was employed during the simulation.

as one moves down the sidewall, becoming negligible at the bottom of the trench. An interesting observation is the presence of notches near the opening of the final deposition profile as seen in the SEM. These notches are present in the initial trench geometry and are mirrored in the topography of the final deposition profile. Although these notches demonstrate the capability of pulsed PECVD to coat irregular features, we avoid replicating these notches in our simulation due to problems associated with meshing such a geometry. At the bottom of the trench the predicted thickness is ~ 120 nm, matching the experiment and confirming that only the ALD component contributes appreciably to film growth at the bottom. In contrast to the previous example, exposure limitations did not attenuate the contributions of the ALD growth mode. This was expected as the experimental TMA exposure in this experiment was 875 L (Figure 4.7), which was greater than the minimum exposure value required at the end of deposition (~800 L).

4.4 Summary and Conclusions

This work described the development of a feature scale model capable of predicting film profile evolution in pulsed PECVD under conditions that are self-limiting. Our model simulates the transient nature of pulsed PECVD by assuming it to be a combination of two steady state deposition processes, represented by ϕ_{ALD} and ϕ_{PVD}. This relatively simple formulation does a good job of predicting feature evolution in pulsed PECVD as a function of the relative contribution of these two growth modes. Moreover, a simple and effective approach is used to account for ALD exposure limitations that can arise in high aspect ratio features. The sensitivity of our results was studied as a function of the model GPC, and it was demonstrated that significant saving in computation time was possible by employing higher model GPCs, and without compromising on the accuracy of our predictions. The model was validated by

comparisons to experimental results from coated cylinders and trenches. In pulsed PECVD the relative contributions of the PVD/ALD components is an important parameter that can be used to engineer the degree of conformality to produce novel structures that cannot be fabricated by steady state deposition or ALD. The modeling tools developed in this work may be employed to aid the design and fabrication of nanostructures through pulsed PECVD.

4.5 Acknowledgements

The authors gratefully acknowledge the financial support from the National Science Foundation through award CBET-1033203. Support materials were provided through the Center for Nanophase Materials Sciences at Oak Ridge National Laboratory. We thank Dr. Rakhi Patel and Mr. Sterling Parks for fabrication and characterization of some of the structures studied in this work.

CHAPTER 5

DESIGN AND FABRICATION OF ASYMMETRIC MEMBRANES FOR SIMULTANEOUS OPTIMIZATION OF FLUX AND SELECTIVITY

The following chapter is a reproduction of a manuscript in preparation for submission to a peer-reviewed journal for publication.

Design and Evaluation of Vapor Deposition Techniques for Pore Size Modification

*Sanket S. Kelkar, David Chiavetta and Colin A. Wolden**
Department of Chemical and Biological Engineering, Colorado School of Mines, Golden, CO 80401

Abstract

The suitability of three vapor deposition techniques for pore size modification was evaluated using polycarbonate track etched membranes as model supports. A feature scale model was employed to predict the pore geometry after modification and the resulting pure water flux. Physical vapor deposition (PVD) and pulsed plasma-enhanced chemical vapor deposition (PECVD) naturally form asymmetric nanopores that retain high flux as pore size is reduced, but PVD-modified supports exhibited poor control and reproducibility. In contrast, pulsed PECVD and plasma-enhanced atomic layer deposition (PEALD) were shown to deliver digital control over pore size, and good agreement was obtained between model predictions and flux measurements. Exposure limitations during PEALD introduce a degree of asymmetry, though net growth rates were 1-2 orders of magnitude smaller than pulsed PECVD and PVD. Filtration experiments using bovine serum albumin as a model solute showed that pulsed PECVD-modified membranes can be engineered to simultaneously deliver both high flux and high

* Electronic mail: cwolden@mines.edu

selectivity. For example, pulsed PECVD-modified supports were demonstrated to deliver high retention (~ 75%) while maintaining 70% of their initial pure water flux.

5.1 Introduction

Pore size modification is an important tool for engineering the flux and selectivity of both polymeric and inorganic membranes[31, 68, 69]. Solution based techniques such as polymer grafting[70] and electroless gold deposition[71] have been employed to modify the pore size and surface properties of membranes. These modification processes employ multiple time-consuming processing steps involving exposure to hazardous chemicals, which limits their application on a larger scale. In contrast, vapor deposition techniques such as chemical vapor deposition (CVD)[72, 73], physical vapor deposition (PVD)[74] and atomic layer deposition (ALD)[44, 75, 76] are better alternatives for pore modification as they are not specific to chemistry of the membrane material, and the thickness of the coating layer can be controlled over a wide range. A drawback is that optimization of these techniques largely relies on empirical studies of performance as a function of deposited material. Plan view scanning electron micrograph (SEM)images are often used to document the degree of pore closure[75, 76], but these images can be highly misleading when there is curvature in the pore opening, and due to challenges with focusing at nanoscale dimensions. In this work a feature scale model is used to design pore geometries and predict their performance. The model is validated by experimental measurement of flux and selectivity for three different vapor deposition techniques: PVD, plasma-enhanced ALD (PEALD), and pulsed plasma-enhanced chemical vapor deposition (PECVD).

Polymeric track-etched (TE) membranes are used in this work as model supports due to their well-defined size and geometry, and narrow pore size distribution[77, 78]. These

membranes are fabricated by bombarding polymeric films with heavy nuclei to create damaged track, which are subsequently etched to create micro- and nano- sized pores[18]. Approaches which can tailor the pore size and surface properties of TE membranes would be an enabling innovation for extending the application spectrum of these membranes[31, 76, 79]. For example, it has been shown that post-modification of polymeric TE membranes can drastically improve their hydrophilicity[80], anti-fouling properties[81] and selectivity[31]. In principle, it should be possible to modify these membranes with a thin selective layer, which shouldn't adversely affect the flux but drastically improve the selectivity due to reduction in pore size[82].

PVD techniques such as thermal evaporation and sputtering have been commonly used for surface modification[80], as well as for creating catalytic membrane surfaces[83]. The simplicity of this high rate deposition method makes PVD appealing for membrane modification. PVD techniques produce asymmetric nanopores since deposition does not penetrate significantly inside the pores[74]. Such non-conformal coatings could potentially help overcome the trade-off between maintaining high flux and good selectivity. Here thermal evaporation of aluminum was used as a benchmark for comparing PVD with the other pore size modification techniques described below.

ALD has emerged as a leading approach for precise pore size reduction and surface modification of TE membranes[69, 75, 76, 79]. ALD provides digital control over the thickness due to its self-limiting nature, and the thickness of the material can be tuned precisely by simply varying the number of deposition cycles. In this work, PEALD of titania (TiO_2) was employed as one of the techniques for tailoring pore size of track-etched membrane supports. PEALD is a variation of ALD in which plasma is employed during one of the exposure steps of the ALD

cycle to drive the chemistry[84]. The application of plasma allows for the deposition to be carried out at a significantly lower temperature in comparison to thermal ALD.

Despite its elegant nature, the ALD route for pore size modification has a few drawbacks. First, the conformal nature of ALD leads to densification of the pore interior, which can lead to severe flux reduction[46, 75]. Second, practical application of ALD for coating larger pores could be problematic due to the extremely low growth rates in ALD, which severely limits the throughput. Lastly, it is often assumed that ALD provides perfect conformality throughout the structure, but this requires that both the precursor dose and the purge times be sufficiently large to ensure complete delivery/removal of reactants/products. The original TE membrane supports are very high aspect ratio structures, and the aspect ratio increases dramatically as pore closure is approached[36]. In practice, it is unlikely that sufficient exposure and purge times are used to ensure conformal coverage throughout deposition. This can be advantageous in that exposure-limited ALD process can be exploited in membrane applications to fabricate non-conformal pores for high flux applications. The feature scale model tool is applied to analyze the consequences of operating ALD in an exposure-limited mode.

The novel pore modification technique used in this work is pulsed PECVD. Pulsed PECVD is an alternative that provides the throughput and asymmetry of PVD while retaining the digital control offered by ALD. Our group has developed pulsed PECVD as an alternative to ALD for digital control over deposition on planar surfaces for a number of oxides including SiO_2[26], TiO_2[27], Al_2O_3[85], and ZnO[28]. In this technique, a metal precursor highly diluted in oxygen is continuously delivered to the reactor and the plasma is pulsed using square wave modulation at low frequency (~1 Hz). Under certain conditions pulsed PECVD can be operated in a self-limiting fashion. First, it requires that no thermal CVD occurs when the plasma is off

since the reactants are inert at the temperature employed. This condition is met because molecular oxygen is unreactive with many precursors at low temperature. The second requirement is that no deposition occurs under continuous plasma operation. This occurs when the diluted precursor is fully consumed or sacrificially deposited before it can reach the substrate[25]. However, under pulsed operation at low frequency (~1 Hz) deposition is readily observed, and the growth per cycle can be adjusted over a reasonable range (0.5 – 5 Å/pulse) through control of parameters such as precursor flowrate and duty cycle. The elimination of purge steps leads to higher net deposition rates[24], while the use of plasma enables high quality metal oxides to be deposited at temperatures compatible with polymeric substrates[86].

In the present work, PVD, PEALD and pulsed PECVD were evaluated for pore size and shape modification of TE membranes having a nominal pore opening ~ 100 nm. A feature scale model was used to predict the geometry of the PVD-, PEALD- and pulsed PECVD- modified pores as well as their resulting flux behavior. SEM imaging was employed to investigate the pore opening and surface morphology of the coated pores. Membrane performance was evaluated using measurements of pure water flux and solute rejection through these modified supports using a stirred cell ultrafiltration apparatus.

5.2 Experimental

5.2.1 Materials

Commercial polycarbonate track-etched membranes, known as Isopore^{TM}, were purchased from EMD Milipore Corporation. Figure 5.1 displays top view and cross sectional micrographs of the hydrophilic pristine support. The support openings are tightly distributed around the nominal 100 nm (± 3 nm) pore size, but a few "doublets" are also present where two

pores have fused together. These doublets account for ~7.5 % of the total number of pores in the supplied membrane filter. The cross-section image shows the vertical alignment of the features extending throughout the nominal 25 µm thick support.

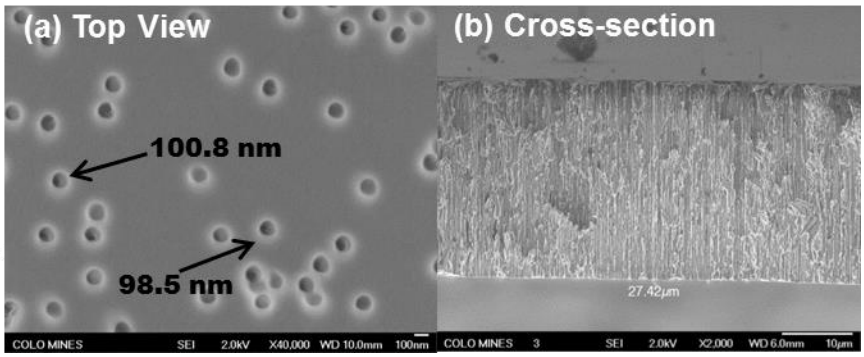


Figure 5.1: (a) Top view and (b) cross-section SEM micrographs of uncoated TE membrane supports.

Titanium tetrachloride, 99% pure was purchased from Sigma Aldrich, and used as a precursor in pulsed PECVD and PEALD modifications. Ultrahigh purity grade argon and oxygen were used as the carrier gas and oxidant respectively. Bovine serum albumin (BSA, molecular weight 66 kDa, Sigma Aldrich) was used to test the separation efficiency of the pristine and modified membranes.

5.2.2 Membrane Fabrication

Pristine TE membranes were modified using 3 deposition techniques: PVD of aluminum, PEALD and pulsed PECVD of titania. Aluminum evaporation was chosen for its simplicity while titania was chosen for a number of reasons. It is a stable material that may be easily functionalized, and it is commonly used for membrane modification[87]. In addition, it maintains a hydrophilic surface[76], so that the changes in membrane performance observed in this work should be primarily due to geometrical effects and not due to changes in surface energetics.

Thermal evaporation of aluminum onto TE membranes was performed in a diffusion-pumped bell jar with a base pressure of 10^{-7} torr. The membranes were positioned at normal incidence to the evaporation boat, and a shutter and quartz crystal microbalance were used to control the thickness of the aluminum coating. Pulsed PECVD and PEALD of TiO_2 was performed in a capacitively coupled plasma reactor described previously[27]. The samples were mounted to the grounded electrode which was resistively heated to 70 °C, well below the maximum operating temperature of the polycarbonate TE membranes used in this study. During pulsed PECVD operation, titanium tetrachloride, Ar diluent, and O_2 were supplied continuously in the reactor without the need of any intermediate purge steps. The precursor was stored in a temperature-controlled bubbler at T = 15 °C, and delivered using Ar as the carrier gas. The plasma power was 50 W, and a square wave modulation was applied to plasma power using a LabVIEW program. The duration of on and off times was 0.5 s each, and the resulting TiO_2 growth per cycle (GPC) was 1.2 Å/pulse. During PEALD operation, the process parameters like plasma power, substrate temperature and gas flow rates were kept the same as in the pulsed PECVD process. The oxygen and diluent argon were flown continuously in the reactor, serving as the purge gas. The precursor flow was alternately directed to the reactor or directly to the vacuum pump through LabVIEW-controlled solenoid valves. For modification of TE membranes the PEALD process employed 17 s purges, a $TiCl_4$ dose time of 8 s, and 6 s of plasma exposure. The desired degree of pore closure in PEALD and pulsed PECVD was achieved by varying the number of deposition cycles.

5.2.3 Membrane Characterization

Variable angle spectroscopic ellipsometry (VASE, J. A. Woollam WVASE32) was employed to measure the thickness of the pulsed PECVD and PEALD TiO_2 coatings, whereas the thickness of the Al coating was determined using profilometry. Field emission scanning

electron microscopy (FESEM) (JEOL JSM-7000 F) was used to study the surface morphology of the modified TE membranes. PEALD- and pulsed PECVD- modified TE membranes were sputter-coated with a thin layer of gold before FESEM imaging to reduce charging, whereas no such coating was required for the Al-coated samples. The pure water flux of PVD-, PEALD-, and pulsed PECVD- modified TE membranes was measured using a stirred ultrafiltration cell (Amicon, Millipore Co) under 10 psi overhead pressure, and the resulting flux is reported normalized to the flux of unmodified TE membranes. BSA was used to determine the solute rejection using a 1 g/L solution prepared in a phosphate buffered saline to maintain the pH at 7.4. During solute rejection measurements, the retentate solution was continuously stirred at 400 rpm using a magnetic stirrer. The concentration of BSA in the filtrate was determined by measuring the absorbance values at 280 nm with a Cary 5G UV-Vis-NIR spectrophotometer.

5.3 Design and Analysis of Asymmetric Pores

Transport properties of nanopores are closely linked to their geometry. As mentioned above, the use of plan view microscopy to characterize the pore size of modified membranes can have limitations. Figure 5.2 compares a plan view micrograph, a cross-section micrograph, and a feature scale simulation of silicon wafers patterned with ~125 nm contact holes and modified by pulsed PECVD of alumina. Patterned wafers were used as surrogates to enable cross-sectional imaging, which is very difficult to achieve from polymeric TE supports. The plan view image (Figure 5.2 (a)) suggests that the average pore opening is ~ 30 nm. However, the cross-sectional image of the nanopore (Figure 5.2 (b)) reveals that the minimum pore opening is much smaller, approximately 10 nm. When these pores are coated there is significant curvature as the pore is

closed, and with plan view imaging it is difficult, if not impossible, to focus on the position of the minimum pore opening.

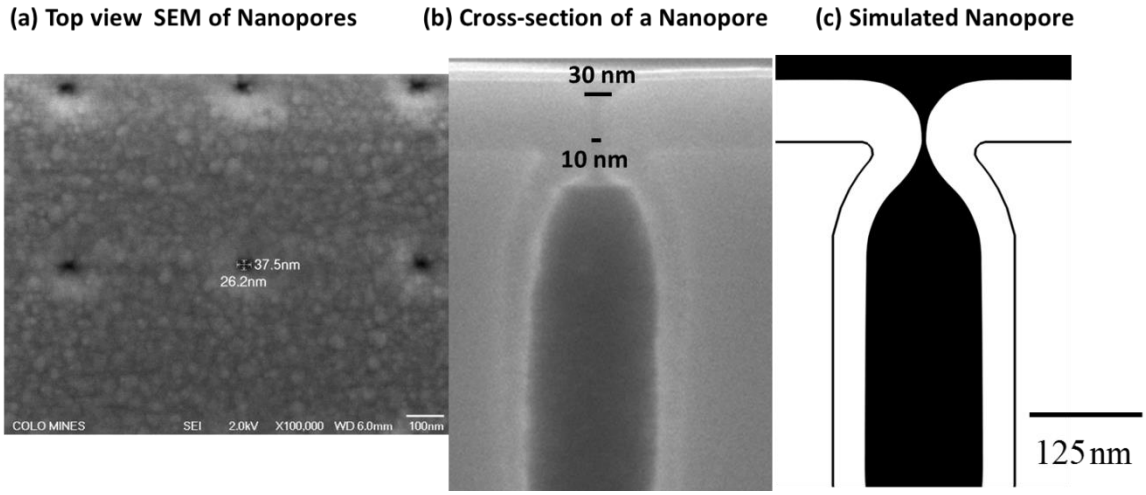


Figure 5.2: (a) Top view SEM micrograph of nanopores fabricated using pulsed PECVD; (b) Cross-section SEM of a nanopore; (c) model prediction of the nanopore geometry using the simulation procedure described in this work.

In order to engineer membrane performance, it is imperative to be able to predict the geometry of the modified pores. Though seldom applied in membrane modification, the microelectronics community has employed feature scale models for decades[32, 54, 57, 88] to understand and control the deposition of films on non-planar substrates. Recently, we developed a feature scale model that can be used to simulate PVD, ALD, and the transient growth modes that contribute to deposition in pulsed PECVD[23]. The model employs a diffusion reaction framework in which steady state deposition is modeled based on surface reaction probability (γ), with PVD ($\gamma = 1$) and ALD ($\gamma \rightarrow 0$) representing the two limits.

Pulsed PECVD is a transient deposition process that involves two growth modes as discussed previously[25]. The first growth mode is analogous to ALD. During the plasma off state, the precursor adsorbs on the substrate surface, and these adsorbed molecules then react with oxygen radicals during the plasma on step to contribute to conformal film growth. The

second growth mode is due to reactive species that are formed at plasma ignition, and then deposit with near unity sticking probability (γ =1) in a manner analogous to PVD. To capture the two growth modes of pulsed PECVD the model simply alternates between conditions used to simulate ALD and PVD, using the single adjustable parameter 'R', which is the ratio of the PVD growth component to the ALD growth component. This value can be determined experimentally using the GPC values measured for both PEALD and pulsed PECVD. For example, if the PEALD GPC is 1 Å/cycle and the pulsed PECVD rate is 2 Å/cycle then R =1, which means there are equal contributions from both growth modes. This model has been validated for both cylindrical pores and Cartesian trenches, with Figure 5.2 (c) providing further validation of its capabilities. The nanopore geometries predicted by the feature scale model are then employed to predict pure water flux using COMSOL.

Precursor diffusion limitations can occur while coating very high aspect ratio features. The feature scale model utilized in this work accounts for exposure limitations that can limit the extent of deposition in high aspect ratio features in both ALD and pulsed PECVD. For a given precursor exposure there is a critical aspect ratio (a*) that can be coated conformally during ALD, and its value can be determined from the scaling relationships developed by Gordon and coworkers[36]. In the model the local aspect ratio (a (z, t)) is calculated as deposition proceeds, and once the local aspect ratio exceeds a*, no ALD growth is allowed.

One utility of this model is that it can be used to design and analyze the performance of membrane supports modified by vapor deposition. Figure 5.3 compares simulated profiles of 100 nm diameter nanopores modified by ALD, pulsed PECVD at R = 1, and PVD. The white area represents the material deposited, whereas the black region represents the surrounding gas phase. In these examples the simulations were performed on cylindrical pores with an initial opening of

100 nm, and in each case deposition was allowed to proceed until the minimum pore opening was reduced to 20 nm. Figure 5.3 (a) shows an ALD-modified pore assuming no exposure limitations, which is perfectly conformal and results in densification of the underlying support. The other extreme, Figure 5.3 (c), shows the feature predicted for an ideal PVD process with unity sticking coefficient. Very little deposition is observed within the feature, creating a highly asymmetric pore structure that would be ideal for membrane applications. A drawback of this technique is that it requires considerably more deposition to achieve the same degree of pore closure. Finally, Figure 5.3 (b) shows the simulation for pulsed PECVD at R = 1, in which the contributions of the two growth modes are equal. The pore closure is asymmetric reflecting the benefits of PVD, but the total amount of material required is closer to the ALD case.

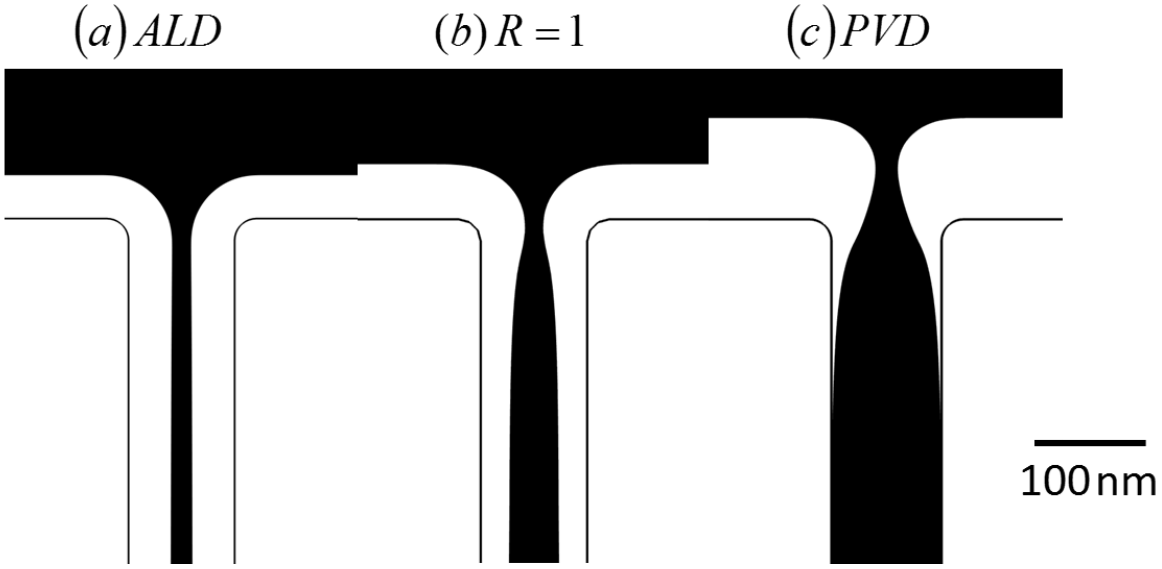


Figure 5.3: Simulated deposition profiles on 100 nm features coated by (a) ALD, (b) pulsed PECVD, and (c) PVD for a final pore opening of 20 nm.

In the results below the feature scale model is used to simulate the nanopore geometries formed by vapor deposition on 100 nm diameter isopore supports. Membranes coated by

aluminum evaporation employed the PVD simulation described above. The pore geometry of the TE membranes modified by PEALD was simulated by superimposing precursor diffusion limitations on the ideal ALD case shown in Figure 5.3 (a). The critical aspect ratio during these depositions was estimated to be around a* = 36, based on the 8 s $TiCl_4$ exposure. This means that deposition initially extends ~3.6 μm into the 25 μm pore, and this depth will continue to decrease as the pore shrinks.

The model parameters for pulsed PECVD reflected the experimental conditions. Based on the $TiCl_4$ exposure provided during the ½ second plasma off step, a critical aspect ratio of a* = 8.2 was estimated. Again, this implies that initially the ALD growth component extends 820 nm into the pore, and this value diminishes as growth proceeds. Note that this value of a* represents an upper limit, and the simulations were not significantly sensitive to this parameter. Using identical precursor doses the measured GPC for PEALD and pulsed PECVD were 0.56 Å/cycle and 1.2 Å/cycle, respectively. Hence, the corresponding PVD/ALD ratio or R was determined to be ~1. The net planar growth rate in pulsed PECVD was 7.2 nm/min, over 35 times faster than the 0.2 nm/min obtained with the PEALD process.

5.4 Results and Discussion

The left panel of Figure 5.4 shows the top view SEM micrographs of TE membranes modified by different vapor deposition techniques employed in this work namely PVD, PEALD and pulsed PECVD as a function of thickness. The labels report the planar thickness of the deposited film, and the arrows in the micrographs point out the apparent diameter of the resulting pore openings. The right panel of Figure 5.4 displays simulated cross-sections of the resulting pore geometries at these same conditions, and the labels indicate the minimum pore diameter

under these conditions. The specific conditions were chosen to provide examples of low, intermediate, and high degrees of pore closure for each deposition technique.

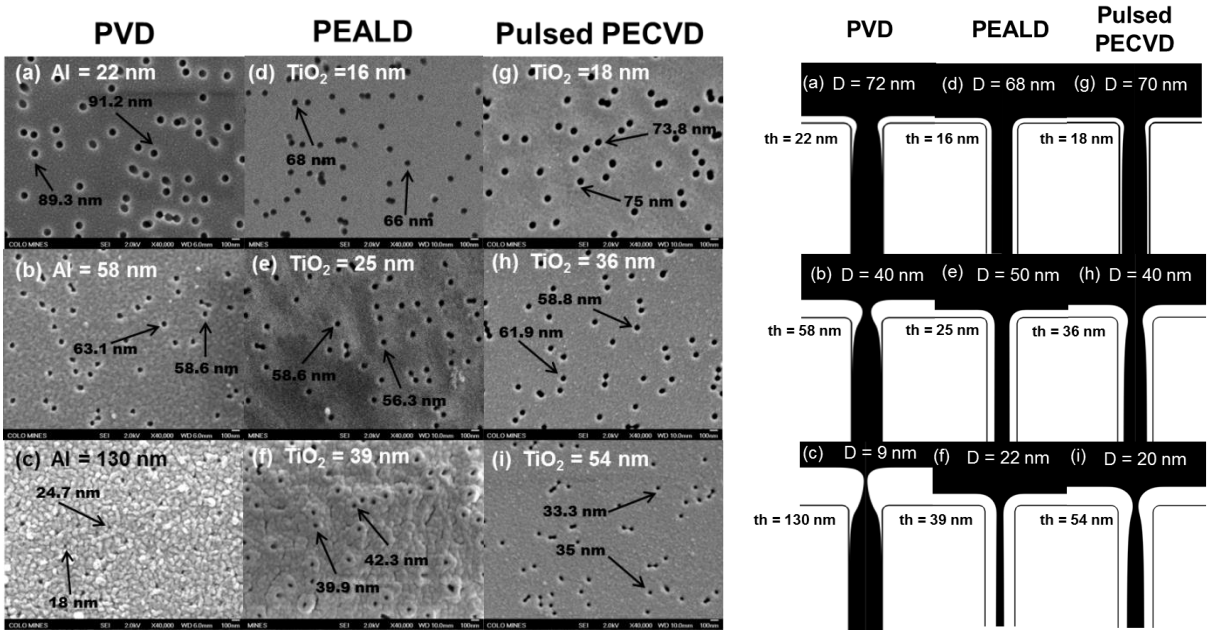


Figure 5.4: The left panel displays top view micrographs of TE membranes modified by PVD of aluminum (a-c), PEALD of TiO_2 (d-f), and pulsed PECVD of TiO_2 (g-i) as a function of planar film thickness. The right panel displays the corresponding feature scale simulation of the resulting geometries noting the minimum pore diameter for these 9 cases.

There a number of important observations to take away from this figure. First, the micrographs confirm that the amount of deposited material required to achieve the same degree of pore closure varies by techniques in the descending order PVD > pulsed PECVD > PEALD as predicted in Figure 5.3. For example, to reduce the minimum pore diameter to 40 nm requires 30 nm of PEALD deposition, 36 nm of pulsed PECVD, and 58 nm of PVD. Moreover differences become more pronounced as the degree of pore closure increases. Second, this figure confirms the limitations of using top view microscopy for evaluation of pore closure. At low levels of deposition (Figure 5.4 a/d/g) the pore diameter estimated from SEM images is in good agreement with model predictions. However, the disparity between these values gets worst with increasing

deposition. At a high degree of pore closure (Figure 5.4 c/f/i) the SEM image overestimates the minimum pore size by a factor of ~2 for all three deposition techniques. Finally, it is observed that the morphology of the three films are quite different. In the case of evaporated aluminum the coatings are rough, reflecting the Volmer–Weber growth mode that results in a polycrystalline morphology[89]. These films would fall into zone 1 of the Thornton diagram[90], which consists of columnar growth with voided growth defects due to atomic shadowing. The diffusion-reaction model does not capture these features, but as shown below it has a significant impact on membrane performance. At low deposition thickness, both pulsed PECVD and PEALD display a smooth surface morphology. However at a coating thicknesses > 30 nm the PEALD becomes rough and appears to become polycrystalline (Figure 5.4 (f)) whereas the pulsed PECVD film remains smooth and amorphous. This behavior reflects the unique feature of TiO_2. It has been observed that TiO_2 ALD initially produced amorphous material, and there is a critical thickness at which point it transforms into the anatase phase, the exact value of this transition depends on deposition conditions[27, 91, 92]. Due to its slower growth rate the PEALD films likely have better quality and transform at a lower thickness than the pulsed PECVD films.

Figure 5.5 compares the membrane flux as a function of the planar thickness for the three different modification methods. Uncoated supports had a pure water flux (PWF) of 7360±294 $L/(m^2.h.bar)$. Relative flux is defined as the pure water flux (PWF) of a coated TE membrane normalized with respect to that of the uncoated TE membranes. The solid black lines represent the flux predicted by the feature scale model, which were obtained by exporting the simulated geometries of the modified pores into another COMSOL module and modeling Hagen-Poiseuille flow through the resulting pores. In addition, the flux expected from a perfectly conformal coated pore is included as the dashed red lines for comparison. The flux of a conformally coated

membrane is predicted to drop sharply due to densification of the pores. In contrast, the techniques used in this work that lead to asymmetric pore closure allow the flux to remain largely unchanged until the pore diameter is reduced < 20 nm.

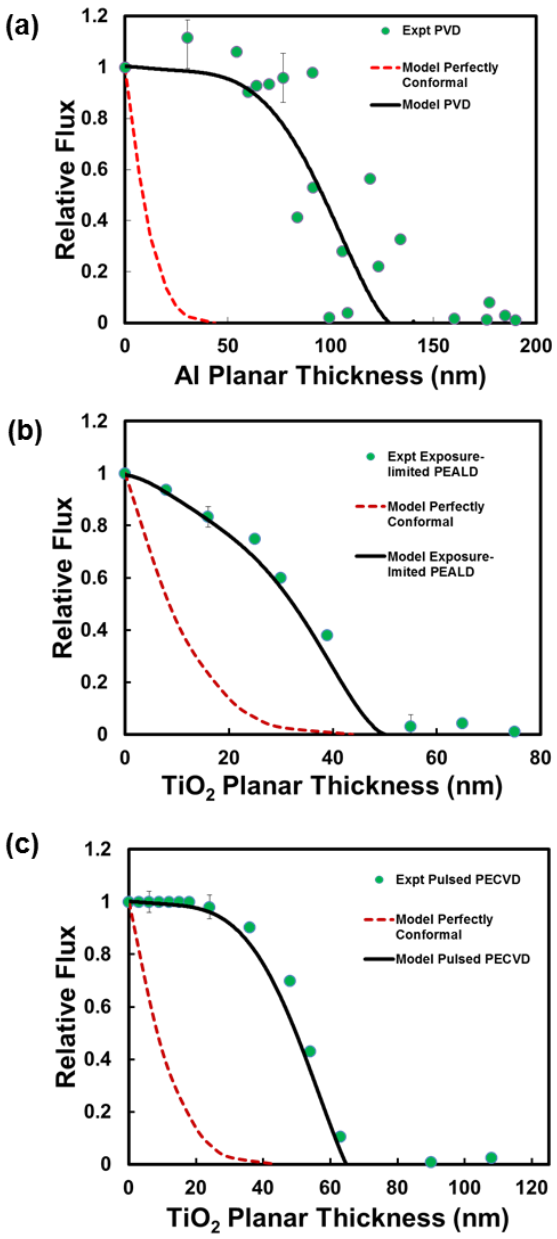


Figure 5.5: Comparison of experimentally measured (points) and predicted flux (black lines) as a function of deposition thickness for TE membranes modified by (a) aluminum PVD, (b) PEALD of titania, and (c) pulsed PECVD of titania. The dashed red line is the prediction for perfectly conformal modification.

Figure 5.5(a) shows the results for the PVD-modified membrane. There is generally good agreement between the measured and predicted flux. However, there is significant scatter in the data and poor reproducibility, which is attributed to the roughness and morphological instabilities associated with the columnar growth mode. As expected, the asymmetric pore geometry allows the flux of PVD-modified supports to remain nominally unchanged up to a thickness of 75 nm. The flux of the membranes drops to 0 only for coating thicknesses > 125 nm. In the range of 75 -125 nm, where pore closure is approached, there is great variability with similarly coated pores delivering high flux or no flux. This makes PVD unsuitable for nanoscale control of performance.

In contrast, both PEALD and pulsed PECVD provided excellent reproducibility and control over the degree of pore closure. In the case of PEALD (Figure 5.5 (b)) the flux declines approximately linearly with the amount of TiO_2 deposited, and the agreement with the model is excellent. The measured flux is slightly greater than model predictions in the transition regime, and there is a very small but non-negligible flow measured for membrane modified with >50 nm of material, where pore closure is predicted. Both of these minor deviations are attributed to the presence of the doublets (Figure 5.1 (a)) that are not accounted for in the model. The stark contrast between the conformal prediction and the observed performance highlights the importance of operating ALD in the exposure limited regime in order to maintain significant flux.

Pulsed PECVD (Figure 5.5 (c)) combines the asymmetry of the PVD modification with the control and reproducibility of ALD. The flux is unchanged up to 30 nm of deposited material, and then it begins to attenuate as pore closure is reached. The flux drop off in this regime is steep, and the digital control and smooth morphology enables precise control over membrane

properties. The amount of material for complete pore closure is just slightly greater than PEALD, but less than half the material required by PVD. For all three deposition techniques, the experimentally measured flux is well captured by the model, validating its utility for this application.

The selectivity of the modified membranes was evaluated using BSA as a model solute in a stirred ultrafiltration cell. These results were not significantly impacted by protein adsorption as it was found that both the pristine TE membranes and all of the modified supports exhibited excellent anti-fouling characteristics. The membranes exhibited a static BSA adsorption value < 10 $\mu g/cm^2$ after immersion in a 1 g/L BSA solution for 24 hours. This is attributed to the hydrophilic nature of the original TE membranes. The hydrophilicity, and hence the anti-fouling nature, of the membranes is maintained even after modification. Hydrophilicity of the membranes was tracked using a simple home-built contact angle measurement apparatus[93]. The contact angle of the pristine TE membranes, TiO_2-modified membranes, and Al-modified membranes were 44±3°, 52±5°, and 65±7°, respectively. It should be noted that the TiO_2-modified TE membranes were initially very hydrophilic. However, the hydrophilicity is quickly lost upon prolonged exposure to the atmosphere due to hydrocarbon contamination.

Figure 5.6 compares the solute rejection and the modeled flux of the modified TE membranes as a function of the planar thickness of the deposited coatings. BSA (molecular size ~ 7 nm) was used as the model solute. Figure 5.6 (a) displays the solute rejection of the PVD-modified supports. Solute rejection scales linearly with thickness, and reaches a maximum of ~70% only after the evaporation of 200 nm of aluminum, at which point the flux is negligible. As with measurement of flux, the solute rejection data is also very noisy, reflecting the rough

morphology of these layers. The optimal value for PVD modification was achieved at 100 nm of coating thickness. In this membrane the solute rejection was just 44%, and though the model

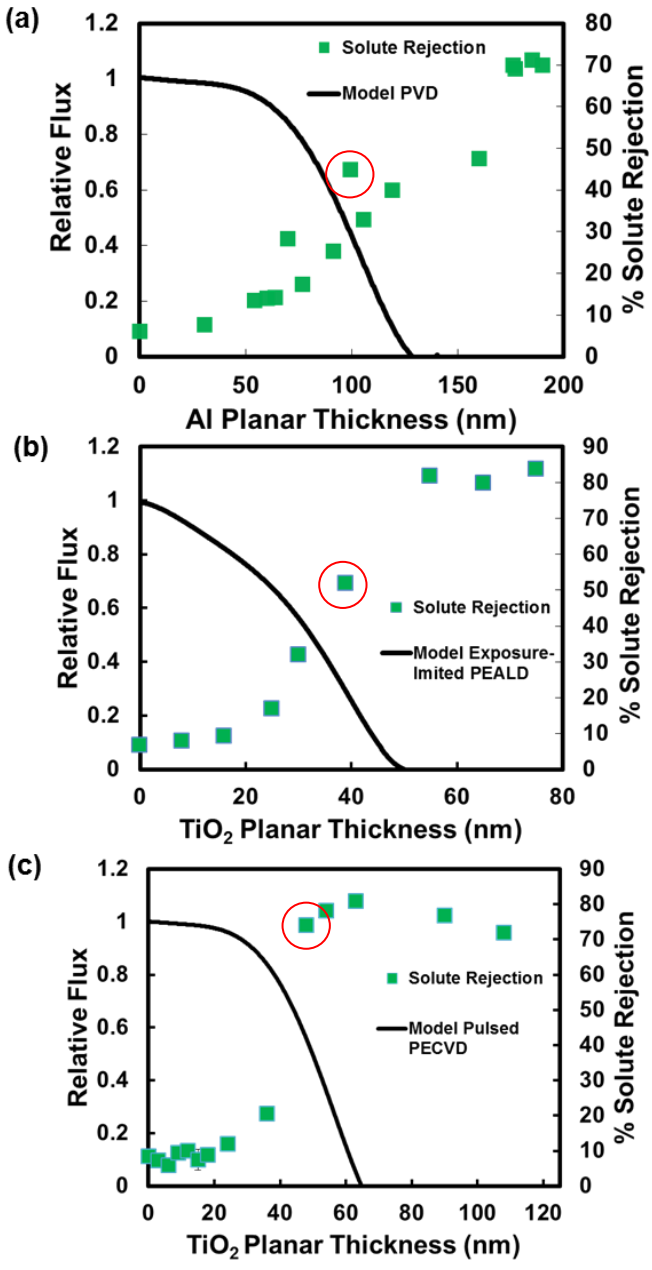


Figure 5.6: Solute rejection and predicted flux as a function of film thickness for (a) PVD-modified membranes; (b) PEALD-modified membranes and (c) Pulsed PECVD-modified membranes. Circled values indicate membranes that displayed the best combination of flux and selectivity for each technique as discussed in the text.

predicts 45% of the original flux the measured value was just 29%. With the PVD-modified supports >50% solute rejection was only achieved when the flux approaches zero.

In the case of PEALD, the solute rejection was negligible (<10 %) and unchanged through 20 nm of deposition. The rejection then increases linearly between 20 and 50 nm, where the rejection saturates at ~80%. At this point the 100 nm pores are completely closed, and the very small flux of BSA solutes is due to doublets. Optimal performance was achieved with the membrane coated with 39 nm of TiO_2 film. At this point the 50% solute rejection was achieved while retaining 40% of the initial membrane flux. So, although the control and reproducibility was significantly improved relative to PVD modification, only modest improvements in selectivity/flux were obtained.

In contrast to PEALD, the retention behavior of membranes modified by pulsed PECVD exhibit step function behavior as shown in Figure 5.6 (c). For <25 nm of TiO_2 deposition the membranes display negligible solute rejection (~7%) that is unchanged from the uncoated support. The rejection level increases sharply between 40-50 nm of deposited material to a value of ~75%, that remains essentially unchanged with additional coating and is attributed to the presence of doublets. The membrane modified by 48 nm of TiO_2 deposition retained ~70% of the original flux, and the BSA solute rejection approaches the saturation threshold (~ 75%). This is a tremendous improvement over both PVD and PEALD modification. The window for optimal performance is narrow, and thus the digital control over deposition provided by pulsed PECVD is important in achieving this level of performance.

5.5 Conclusions

Track-etched membrane supports were modified using PVD of aluminum, PEALD and pulsed PECVD of titania. A feature scale model was used to design the resulting pore geometries, successfully predicting the flux behavior of modified membranes. PVD modification results created highly asymmetric nanopores that in principle should lead to high flux and good selectivity. However, PVD requires much more material for comparable pore closure, and the rough, columnar growth morphology limits reproducibility and solute retention. PEALD was shown to deliver precise pore size reduction, requiring significantly less film deposition in comparison to PVD. By operating in a precursor exposure limited regime, the PEALD-modified membranes exhibited higher flux than would be achieved with perfectly conformal deposition. However, both flux and retention scaled linearly with deposition thickness, limiting the ability to simultaneously optimize both quantities. Pulsed PECVD produced asymmetric pores characteristic of PVD while displaying the precision and reproducibility of PEALD. Both flux and retention display step function behavior with respect to thickness, creating a small window to overcome the flux/selectivity tradeoff. The digital control of pulsed PECVD enabled access to this region, achieving maximum solute rejection while retaining 70% of the original flux.

5.6 Acknowledgements

The authors gratefully acknowledge the financial support from the National Science Foundation through award CBET-1033203.

CHAPTER 6

SURFACE FUNCTIONALIZTION OF AMORPHOUS ALUMINA SURFACES WITH OCTADECYLTRICHLOROSILANE SELF-ASSEMBLED MONOLAYERS

The following is a reproduction of a paper published in the Applied Surface Science. Volume 282, pp. 291-296, 2013. This chapter is reproduced as published except that section numbers, references, and figure labels were changed to conform to the thesis format.

Formation of octadecyltrichlorosilane (OTS) self-assembled monolayers on amorphous alumina

Sanket S. Kelkar, David Chiavetta, and Colin A. Wolden[*]
Department of Chemical and Biological Engineering, Colorado School of Mines, Golden, CO 80401

Abstract

The kinetics and thermodynamics of octadecyltrichlorosilane (OTS) self-assembled monolayers (SAMs) on vapor deposited alumina were quantified. Ozone cleaning serves to create well-defined hydrophilic surfaces for OTS attachment, and the use of heptane as a solvent enables the formation of high quality SAMs under ambient conditions. The kinetics were characterized as a function of OTS concentration using contact angle goniometry, ellipsometry and Fourier transform infrared (FTIR) spectroscopy. The kinetics of SAM formation and the saturation contact angle (~100 ^{o}) on alumina were comparable to what has been observed for OTS on silicon. The free energy of adsorption with ΔG_{ads} values ranged from -7.5 to -5.4 kcal/mol, and the SAMs were stable up to 230 °C. The critical surface tension of the OTS monolayer was found to be 21.4 dyne/cm.

[*] Electronic mail: cwolden@mines.edu

6.1 Introduction

Self-assembled monolayers are of great interest due to their ability to modify the physical and chemical properties of different surfaces and interfaces such as adhesion, corrosion and passivation[40, 94, 95]. These SAMs have important applications in sensors[96], advanced lithography[97], lubrication[98], and anti-stiction coatings for MEMS[95, 99]. Since the pioneering work by Whitesides and co-workers[100], octadecyltrichlorosilane (OTS, $CH_3(CH_2)_{17}SiCl_3$) is perhaps the mostly widely used reagent for generating SAMs on a variety of substrates[95, 101]. Adsorption of OTS on Si/SiO_2 substrates has been studied in depth, and the kinetics and mechanistic details of this process are fairly well-established[95, 99, 102]. The focus of this work is to examine OTS attachment to amorphous alumina, which is a proven to be an effective passivation layer[103] that may be deposited with high control using techniques like atomic layer deposition (ALD)[22]. Anodized alumina is commonly used directly as a membrane or as a membrane support[104, 105], while vapor-deposited alumina has also been used to tune pore size through techniques such as atomic layer deposition[43]. Since aluminum oxide is a biocompatible material[106], such structures are also promising for use in applications like biosensors and bioseparations[107]. A goal of this work was to develop a simple, effective approach to functionalize these types of surfaces.

There has been limited work reported for OTS attachment to alumina. A previous study examined the attachment of OTS to single crystal alumina (Al_2O_3)[108], as it was suggested that there was an epitaxial relationship with the (0001) surface. There have also been studies of SAM attachment to aluminum[109-111], an important industrial material which easily passivates in the presence of air to form a 4-6 nm thick layer of Al_2O_3. A number of factors influence the growth of monolayers[112], however substrate preparation and the availability of water are perhaps the

two most important. A hydrophilic surface is critical for SAM attachment[113, 114], and in the case of crystalline alumina[108] a piranha etch was used to prepare the substrates. In this work we assess the ability of UV-ozone treatments as a benign alternative to condition the substrates, and quantify the stability of the resulting surface.

A small amount of water is required to facilitate OTS attachment through the hydrolysis of chloro moieties, however excess water content leads to the polymerization of OTS molecules in the bulk solution[115]. The amount of water is controlled by the choice of solvent and the humidity level[116, 117]. In the case of OTS toluene has been the most commonly used solvent[40, 110, 116, 117] though numerous others have been explored including hexane[114, 117], chlorobenzene[118], hexadecane[119], cyclohexane[120], dodecane[102], bicyclohexyl[111], and mixtures of solvents[108, 121]. Rozlosnik and coworkers[102] first identified heptane as a superior solvent for OTS attachment on silicon. Heptane has lower solubility for water than toluene (0.01 vs. 0.033%), and this was observed to result in more homogeneous OTS monolayers. Rozlosnik and co-workers explored the effect of relative humidity on the attachment kinetics and found that complete OTS monolayers could be obtained for a wide concentration range under ambient conditions when using heptane. They reported that full monolayers were formed after 3 hours, but did not discuss the kinetics of the attachment process in detail.

In this work we quantify the attachment kinetics of OTS on amorphous alumina by sequentially immersing samples into OTS/heptane solutions and documenting the surface energy using contact angle goniometry. The sequential immersion technique has advantages over non-sequential immersion because it avoids deviations due to sample variability, and is also known to

have faster kinetics[40] and to form films with fewer defects[122]. The quality and stability of the resulting monolayers is assessed.

6.2 Experimental Details

6.2.1 Materials

OTS (95%) was procured from Gelest, inc. Isopropyl alcohol (min 99%) and absolute alcohol (200 proof) was obtained from PHARMO-AAPER. Heptane (typical 99 %) was bought from Mallinckrodt Chemicals. The chemicals were used as received.

6.2.2 Deposition of Aluminum Oxide

Aluminum oxide was deposited on *p*-type silicon wafers by pulsed plasma enhanced chemical vapor deposition (PECVD) as described in detail previously[85]. Pulsed PECVD is an alternative to atomic layer deposition (ALD) for self-limiting growth of alumina that enables higher net deposition rates while delivering comparable film quality[24, 25]. Alumina films nominally 100 nm in thickness deposited at a temperature of 101 ^{o}C served as the substrates for these investigations. These films displayed a refractive index of 1.63, which is comparable to the value obtained for alumina deposited using ALD. Since, refractive index can be taken to be an indicator of film density, our film quality is at par with the purest alumina film[24].

6.2.3 Pretreatment of Substrates

Sample cleaning and hydroxylation were accomplished using a commercial UV-ozone cleaner (UVO Cleaner 42). After the UV-ozone treatment the sample was rinsed successively by isopropyl alcohol, 1:1 water/ethanol and deionized water. Samples were dried thoroughly before

investigating SAM attachment. OTS solutions were prepared in heptane, with concentrations ranging from 25 μM to 2500 μM. Aluminum oxide coated substrates were immersed in the OTS solutions under ambient conditions for desired time intervals and after removal from solution they were sequentially washed with heptane, isopropyl alcohol, 1:1 water: ethanol mixtures, and deionized water. The contact angle was measured and then sample was dried and returned to the solution for the next time interval. This sequential process was continued until saturation in contact angle was observed. The reproducibility was assessed by performing a minimum of four measurements at each concentration level. Contact angle measurements were conducted using a custom-built apparatus to photograph the profile of a 2.5 μL water drop placed on the sample using a Canon Powershot SX110 IS at an optical zoom of 10X. The small drop size ensured that gravitational effects did not impact the findings. The images were digitized and analyzed using a ImageJ plugin developed by Brugnara et al.[123]. The contact angle was averaged at three different spots on the sample. The accuracy of these measurements is within $\pm 2^{o}$.

6.2.4 Characterization of OTS SAM

FTIR spectroscopy was also used to quantify OTS adsorption using a ThermoNicolet Nexus 870 FTIR spectrometer equipped with a DTGS detector and KBr beam splitter. The contribution of the underlying Al_2O_3 films was background subtracted, and the resolution was 4 cm^{-1}. The thickness of saturated OTS monolayers was estimated using ellipsometry (Woollam WVASE-32). The data was fitted using an isotropic three layer Cauchy model ($Si/Al_2O_3/OTS$), where the properties of the alumina were fixed at its measured value and the refractive index of the OTS film was assumed to be constant (n=1.465, k =0) at a wavelength of 580 nm. To study the thermal stability of the SAM, a fully saturated monolayer sample was annealed in an oven at

a fixed temperature for 30 minutes. The contact angle of the annealed surface was measured at three different spots after bringing it to ambient temperature. This process was repeated till we reached a temperature of 400 ^{o}C. The critical surface tension of saturated OTS monolayers was evaluated by measuring the contact angle as described above using a variety of solvents.

6.3 Results and Discussion

6.3.1 Preparation of Al_2O_3 Surfaces and their Stability

Figure 6.1 displays representative images of contact angle measurements made at various stages of the process. Alumina surface exposed to ambient conditions are relatively hydrophobic (Figure 6.1 (a)), and do not possess a sufficient density of hydroxyl groups to produce a high

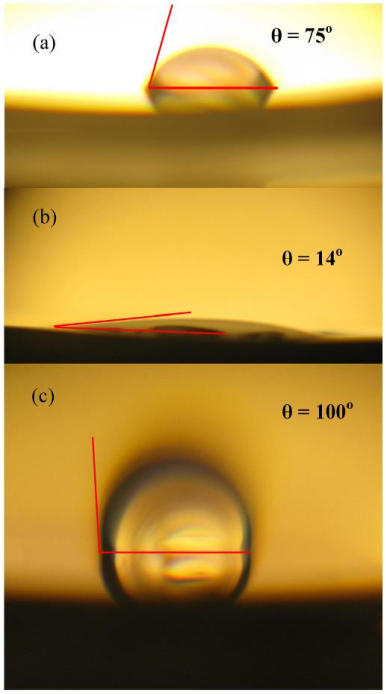


Figure 6.1: Photographs of water droplets used to quantify contact angles: (a) as-received aluminum oxide coated substrates; (b) Al_2O_3 after standard UV-Ozone treatment; (c) Al_2O_3 coated with an OTS monolayer.

quality OTS monolayer. Figure 6.1 (b) shows an image of the hydrophilic alumina surface produced by a standard UV-Ozone treatment of the Al_2O_3 surface. Finally, Figure 6.1 (c) displays an image obtained from a saturated OTS monolayer which displays a contact angle of 100 ^{o}. This tool was used to quantify the kinetics of the silanation process and stability of the resulting monolayers.

UV-Ozone treatments are widely used for removing organic contaminants and generating a hydrophilic surface[124]. It is simple to employ and much more benign than alternatives such as the use of strong acids such as Piranha. Figure 6.2 (a) shows the variation of water contact angle on alumina surface as a function of UV-Ozone exposure time. Upon exposure to UV-Ozone, the alumina surface undergoes a rapid decrease in contact angle before achieving a

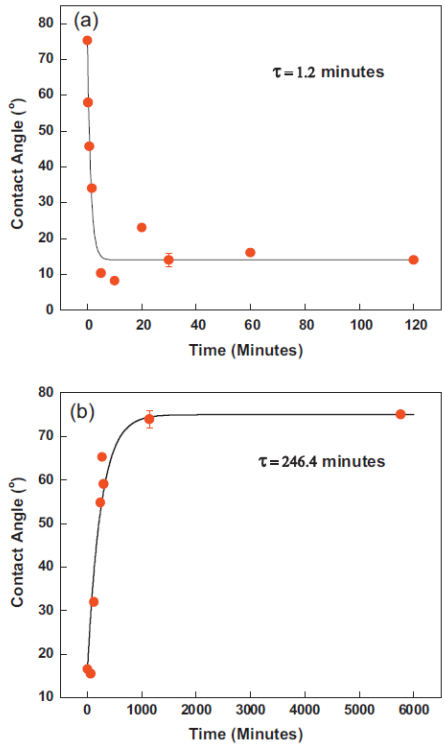


Figure 6.2: Evolution of water contact angle on alumina: (a) as a function of UV-Ozone exposure time; and (b) as a function of time after UV-ozone exposure.

steady state value of around 14^{o}. The mechanism of organic removal involves a complicated set of photochemical oxidation reactions[125]. The trendline is an exponential fit to the data, and the time constant for the process ($1/k_d$) is 1.2 minutes. Although the contact angle achieves a minimum value in the first 5 minutes, a treatment time of 30 minutes was employed on all samples described below to ensure sufficient hydroxyl density on the alumina surface. Upon exposure to ambient conditions the hydrophilic nature of the surface is gradually lost, due to contamination with hydrocarbons in the air[124]. Figure 6.2 (b) displays the dynamics of this process, which has a time constant of around 4 hours. This highlights the need to use these substrates as soon as possible after doing UV-Ozone treatment, which was the procedure adopted in this work.

6.3.2 Kinetics of OTS attachment

These hydrophilic surfaces created by the ozone treatment were immediately deployed in OTS adsorption experiments. The attachment kinetics was studied as a function of OTS concentration under ambient conditions. Figure 6.3 displays the contact angle variation observed as a function of increasing immersion time for different concentrations of OTS. The increase in contact angle is initially rapid before leveling off as complete monolayer coverage is approached[126]. The kinetics increased with OTS concentration, but the saturated contact angle was ~ 100^{o} for the range of OTS concentrations investigated. This saturation contact angle agrees with the value reported in the previous study on OTS adsorption on sapphire[108]. That work was carried out in a glove box, and it required 24-48 hours to form a complete monolayer. Using heptane under ambient conditions the time required to form saturated monolayers was reduced to 1 – 2 hours.

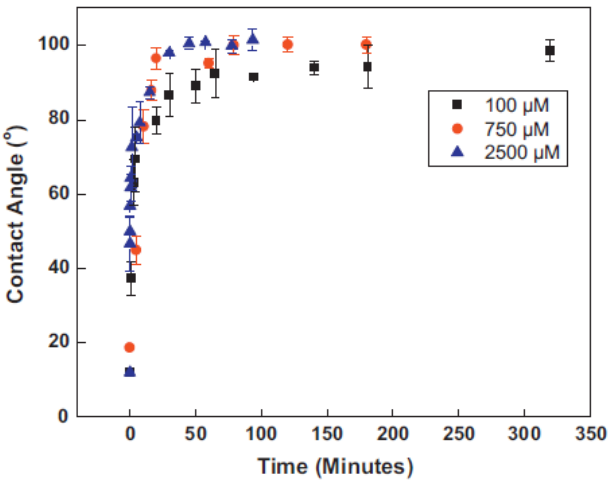


Figure 6.3: Plot of water contact angle vs. immersion time for 3 different OTS concentrations.

FTIR spectroscopy was used to confirm the presence of adsorbed OTS layer on aluminum oxide. Figure 6.4 shows the FTIR spectra of OTS films as a function of immersion time at an OTS concentration of 250 µM. Methylene peaks due to symmetric and asymmetric

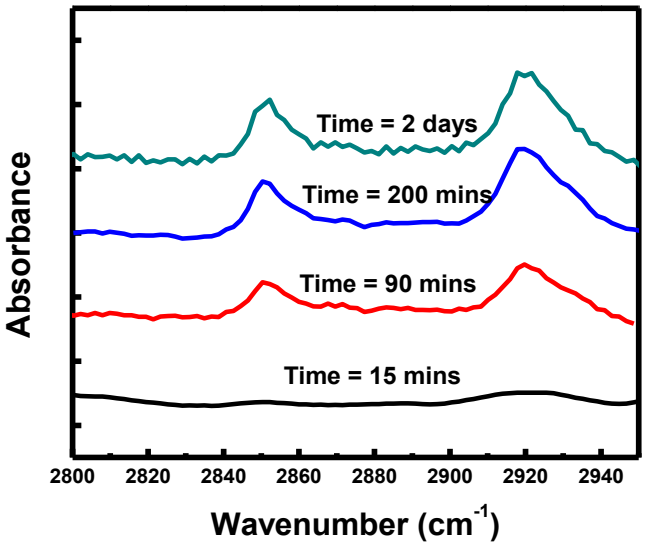


Figure 6.4: FTIR spectra of Al_2O_3 substrates as a function of immersion time in a 250 µM OTS solution.

stretching of the C-H group were observed at around 2850 and 2920 cm^{-1} respectively[99]. The time dependence recorded by FTIR was in agreement with contact angle measurements. While little absorbance is observed at short times, approximately 70% of the signal is in place after 90 minutes, and by around 3 hours the spectra saturate. Leaving the sample in the OTS solution for up to 2 days results in no further changes to the spectra. This confirms that the monolayer is indeed saturated, and that there is no evidence of multilayer adsorption under these conditions.

Ellipsometry was used to determine the thickness of saturated OTS monolayers after 24 hours exposure. Figure 6.5 displays the resulting values as a function of OTS concentration. For concentrations < 200 μM, ellipsometry measurements showed little variability across the substrate and the absolute value was quite close to the thickness of fully covering OTS

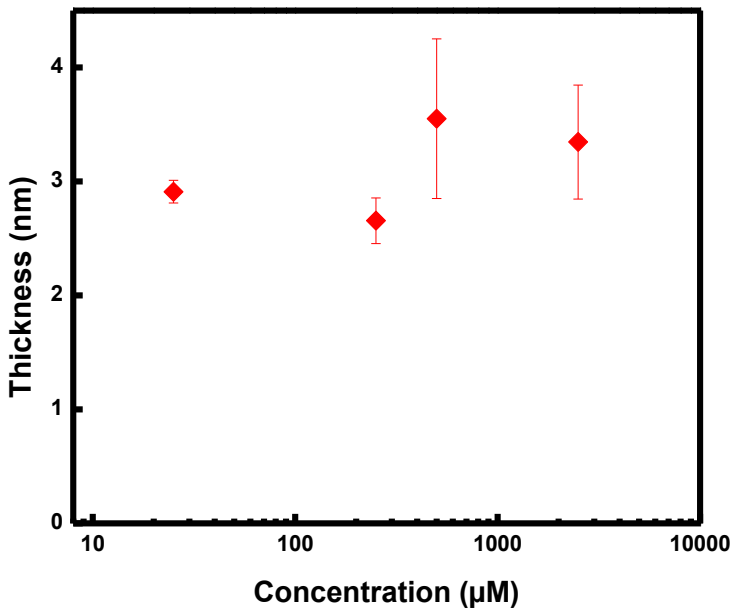


Figure 6.5: Thickness of saturated monolayers as a function of OTS concentration.

monolayer on silicon oxide substrates[102]. At higher concentrations the average thickness was higher than expected for a monolayer and there was significant variability across the substrate,

suggesting that existence of additional adsorption beyond one monolayer. As the attachment times are not significantly different, it implies that use of lower OTS concentration would be most desirable.

To quantify the kinetic and thermodynamic parameters, the contact angle data was converted to fractional coverage. It has been shown previously that non-dimensional contact angle, which is defined as the ratio of the contact angle at any time to the saturation contact angle value, is a close approximation of the fractional surface coverage[40]. If we neglect adsorbate-adsorbate interactions, silanation kinetics can be described by the following first order differential equation.

$$\frac{d\theta}{dt} = k_a(1-\theta)C - k_d\theta \qquad (6.1)$$

where θ is the fractional surface coverage, k_a and k_d are the adsorption and desorption constants respectively. The equilibrium constant and the associated Gibbs free energy of the OTS monolayer formation on alumina may then be extracted from the adsorption and desorption rate constants. A systematic description of these calculations has been given by Kulkarni et al.[99].

Figure 6.6 displays the adsorption (k_a) and desorption (k_d) rate constants as a function of OTS concentration. The adsorption constant decreases with increasing OTS concentration, approaching a value of $k_a \sim 25$ $M^{-1}s^{-1}$ at higher concentrations. In contrast, the desorption rate constant was found to be nearly independent of OTS concentration at $k_d \sim 0.002$ s^{-1}. This behavior is qualitatively similar to what has been reported in the literature[40]. The absolute values of the rate constants are approximately an order of magnitude lower than those reported by Mirji, who employed toluene as the solvent[40]. The finding illustrates the important role of solvents in influencing the kinetics of OTS attachment. Figure 6.7 displays the concentration

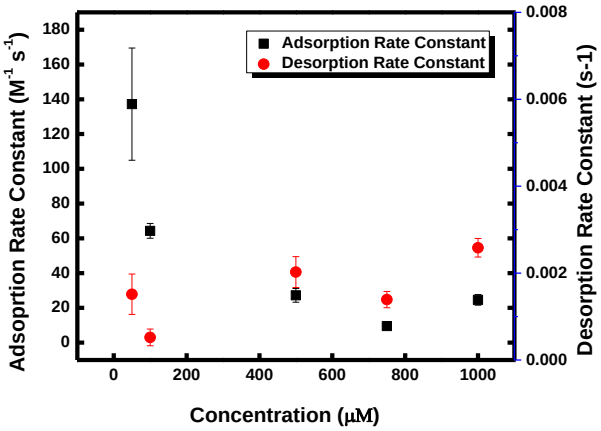


Figure 6.6: The rate constants for adsorption (squares, left axis) and desorption (circles, right axis) as a function of OTS concentration.

dependence of the Gibbs free energy, which mirrors that of the adsorption rate constant, rising from a minimum value of -7.5 kcal/mol and approaching a value of around -5.4 kcal/mol at higher OTS concentrations. This value is comparable to the free energy of SAMs in other systems such as alkanethiols on gold surface (-5.5 kcal/mol)[127] and OTS on Si/SiO_2 (-4.2

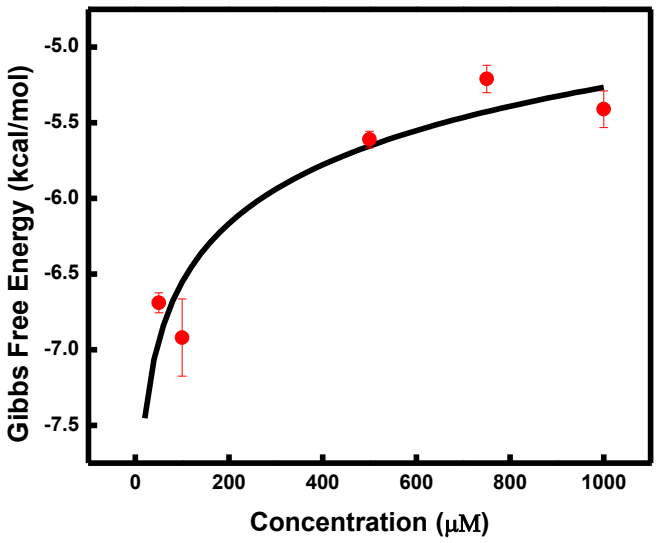


Figure 6.7: The Gibbs free energy of OTS SAMs as a function of OTS concentration.

kcal/mol)[99]. Note that the solvent choice typically influences the kinetics, but not the thermodynamics. For example, in toluene the Gibbs free energy parameters remain similar, but the attachment kinetics are considerably faster, reflecting the importance of water in OTS attachment.

6.3.3 Properties and Stability of OTS monolayers

The critical surface tension of the SAM was deduced from the Zisman plot which is shown in Figure 6.8. To obtain a Zisman plot the contact angle obtained from different solvents with a wide range of surface tension (γ) was measured on saturated OTS surfaces. Low surface tension (dyne/cm) solvents included ethanol (21.5), methanol (22.5), cyclohexane (25.5), hexadecane (27.47), o-xylene (28.9), and toluene (28.5). Ethylene glycol (47.3) and water (72.1) provide solvents with moderate and high surface tension, respectively. The cosine of the contact angle is

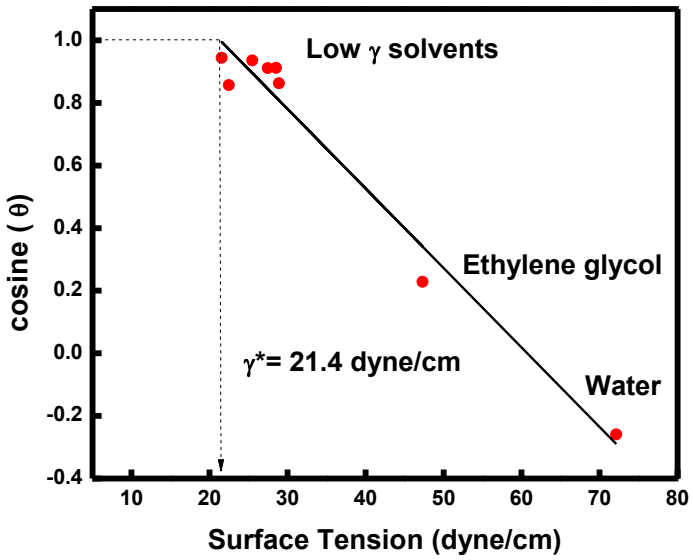


Figure 6.8: Zisman plot obtained from saturated OTS SAMs on Al_2O_3.

plotted as a function of the surface tension of the solvent. A linear fit was used and the critical surface tension is defined by intersection of this line with cosine (θ) = 1, perfect wetting. The critical surface tension of OTS SAMs on aluminum oxide produced in this study was found to be around 21.4 dyne/cm. Again this is quite close to the value reported for close packed OTS SAM on Si substrates (20.2 dyne/cm)[128].

Finally, the thermal stability of the OTS SAMs was determined by annealing OTS/Al_2O_3 samples in an oven and measuring the resulting contact angle as a function of the annealing temperature. All the samples were annealed for 30 minutes and the contact angle was measured at 3 different spots on the sample after bringing them to ambient temperature[129]. The contact angle does not show any significant change until the annealing temperature reaches 230^{o}C.

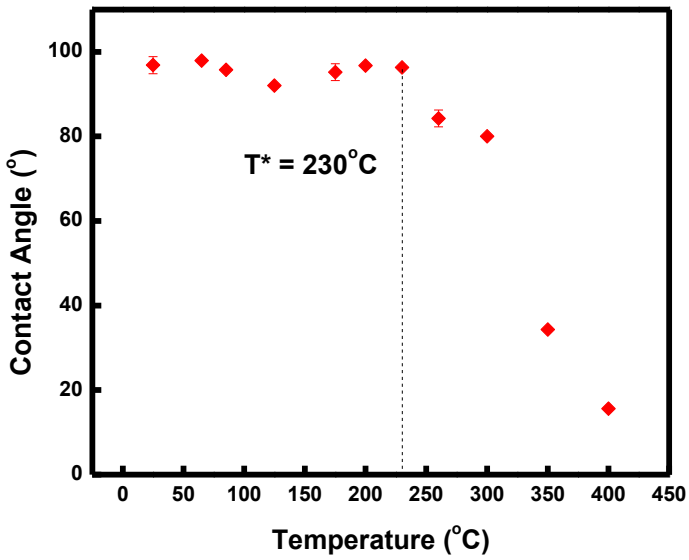


Figure 6.9: The water contact angle on a saturated monolayer as a function of annealing temperature.

Beyond 230^{o}C, the contact angle gradually decreases to a value of around 18 ^{o} at the annealing temperature of 400^{o}C. This decrease at elevated temperature has been attributed to cleavage of

the C-C bond in the OTS chain[129]. The behavior exhibited here is in good agreement with reports for OTS SAMs on Si/SiO_2 substrates[40].

6.4 Conclusions

A simple and robust process was reported for the formation of OTS self-assembled monolayers on vapor-deposited amorphous aluminum oxide surfaces. The alumina surface was rendered hydrophilic using UV-ozone treatments, and the kinetics of OTS attachment in heptane solutions under ambient conditions were quantified using time dependent contact angle measurements. The OTS attachment kinetics to alumina were found to follow a Langmuir adsorption model. Both the kinetics and thermodynamics of attachment to alumina were very similar to what has been reported for SiO_2. Moreover the resulting layers were nominally identical in terms of thickness (~ 3 nm), thermal stability (230 ^{o}C) and critical surface tension (21.4 dyne/cm).

6.5 Acknowledgements

The authors gratefully acknowledge the financial support from the National Science Foundation through award no. CBET 1033203.

CHAPTER 7

SUMMARY OF RESULTS AND RECOMMENDATIONS

This section includes summary of important results presented in this thesis and recommendations for future work.

7.1 Summary of Results

Precise fabrication of nanopores with controlled size, geometry and surface is important for realizing applications such as ionic transistors and DNA sequencing. In this work, application of pulsed PECVD was extended to coat high aspect ratio- features in order to fabricate asymmetric nanopores. In contrast to ALD, pulsed PECVD has two growth contributions which can be manipulated to tune the geometry of the nanopore, but predicting the final nanopore geometry is complicated and requires input from a deposition simulator. A feature scale model was developed in COMSOL to simulate deposition profiles in pulsed PECVD. In the next stage, precise fabrication of asymmetric pores was demonstrated using pulsed PECVD for simultaneous optimization of flux and selectivity. PVD and PEALD were used as alternate pore modification strategies to compare the performance of pulsed PECVD-modified membrane supports. Finally, surface functionalization protocol for attaching octadecyltrichlorsilane (OTS) monolayers to metal oxide surfaces was developed in order to create stable hydrophobic interfaces.

Accurate determination of nanopore geometry is essential for studying hindered transport at the nanoscale as the transport properties strongly depend on the pore geometry. A feature scale model was first developed for steady state deposition processes like chemical vapor deposition (CVD). The deposition profiles were characterized using a parameter known as the

step coverage modulus (ϕ). It was demonstrated that the model can simulate the entire spectrum of deposition profiles ranging from perfectly conformal (characterized by low values of (ϕ)) to highly non-conformal PVD-like profiles (characterized by very high values of (ϕ)). The transient nature of pulsed PECVD was taken into account by assuming the film growth to consist of two growth modes- ALD-like mode when the plasma is off and a PVD-like mode when the plasma is on. The model parameter for pulsed PECVD simulations was 'R' which is the relative contribution of the two growth modes in pulsed PECVD, and is determined experimentally. The feature scale model enables us to rigorously predict the geometry of the nanopores as a function of the planar thickness and the growth per cycle. The model was initially developed by assuming that the ALD growth mode in pulsed PECVD results in perfectly conformal films. This is unlikely to be the case, especially as the aspect ratio of the feature tends to ∞ as the feature opening shrinks during the course of deposition. Simple scaling relationships were employed to take into account the effect of precursor exposure on the conformality of the deposition profiles produced in ALD. Finally, the model was validated by comparing the deposition profiles on patterned trenches and cylinders with the model predictions. The model shows that pulsed PECVD can give rise to novel structures that cannot be fabricated using steady state deposition techniques like CVD or conventional ALD.

The next portion of this thesis focused on tailoring of model supports to form asymmetric pores for simultaneous optimization of flux and selectivity. Three different procedures were adopted in this work for pore modification- physical vapor deposition (PVD) of aluminum (Al), PEALD and pulsed PECVD of titanium oxide (TiO_2). PVD modification inherently results in asymmetric pores which should, in theory, demonstrate simultaneous optimization in flux and selectivity. However, it was difficult to control the pore size precisely in PVD, and this was

found to limit reproducibility and solute rejection. Pulsed PECVD, on the other hand, exhibits digital control over the final pore size which resulted in improved flux behavior of the modified membrane. Also significantly less material deposition was required in pulsed PECVD to shrink the pore size to nanometric levels. Membrane testing showed that there is a narrow window of coating thickness where the membrane retains high flux while showing significantly enhanced selectivity. For example, pulsed PECVD- modified TE membranes showed 75% solute rejection for bovine serum albumin (BSA) protein while retaining 70% of the pure water flux (PWF) of the pristine TE membrane support. Exposure limited PEALD was employed as the third pore modification technique in this work. PEALD modification was shown to deliver some flux enhancement in comparison to conformal ALD modification. This was attributed to precursor diffusion limitations inside the high aspect ratio track-etched pore which leads to non-conformal deposition profiles.

A feature scale deposition simulator was employed to predict geometry of the modified pores. Subsequently, a flux simulator was used to predict the flux behavior of the PVD, PEALD and pulsed PECVD- modified TE membranes using the predicted geometry of the deposition simulator as an input. In general, the model does an excellent job of simulating the flux trends for all types of pore modification techniques, and can be used to design and engineer membrane performance.

Finally, self-assembly protocol was developed for attaching a SAM of OTS on metal oxide surfaces. The motivation behind this study was to create stable hydrophobic nanopore walls for hydrophobicity-based separations. The protocol was first developed for planar aluminum oxide surfaces as a test case, and subsequently this procedure was to be extended to nanopores fabricated using pulsed PECVD. The aluminum oxide surface was first cleaned using

UV-Ozone treatment to remove organic contaminants and to create sufficient hydroxyl groups for further reactions. UV-Ozone treatment was shown to be a very effective, quick and benign surface cleaning technique. The contact angle measurements showed that the UV-ozone cleaned surface loses its hydrophilicity on exposure to atmosphere, and has to be used as soon as possible in the next modification step. The kinetics and thermodynamics of OTS attachment was explored as a function of OTS concentration in heptane using contact angle goniometry, FTIR spectroscopy and ellipsometry. Langmuir adsorption model was found to be sufficient to explain the OTS attachment kinetics.

OTS SAM thickness was monitored using ellipsometry, and higher OTS concentrations were shown to result in additional adsorption beyond the monolayer stage and higher variability in the coating thickness. OTS concentrations < 500 μM were found to form coatings with excellent uniformity and a consistent thickness of 2.8 nm. The OTS SAM demonstrated excellent thermal stability, and were stable up to temperatures as high as 230 ^{o}C. The critical surface tension of the OTS monolayer was found to be 21.4 dyne/cm, which is close to the value of close packed OTS SAM. However, attempts to extend this recipe to modified TE membranes were not successful because of pronounced degeneration of the underlying TE membranes in the heptane solution used for dissolving OTS.

7.2 Recommendations for Future Work

In this section, recommendations for future work pertaining to investigation of ion transport and surface functionalization of nanopores are included.

7.2.1 Future Work: Investigation of Ion Transport through Asymmetric Nanopores

The phenomenon of ion current rectification in nanopores is attracting a lot of attention in the growing area of nanofluidics[5, 6]. As shown in Figure 7.1 (a), the effect of ion current rectification in nanopores is observed in the form of asymmetry in the current-voltage curves[130]. This behavior is similar to a semiconductor diode in the sense that the ion current through the nanopore for a voltage of a particular polarity is much higher than the current for the voltage of the opposite polarity. This is due to the fact that depending on the direction of the applied electric field, the space inside the nanopore is either enriched or depleted of charge carriers. Previous investigations have shown that the pore opening should be of the order of few nanometers, and that the pore shape should be asymmetric for the ionic current to be rectified[130]. Presence of charged pore walls is also essential for the nanopore to rectify current[131].

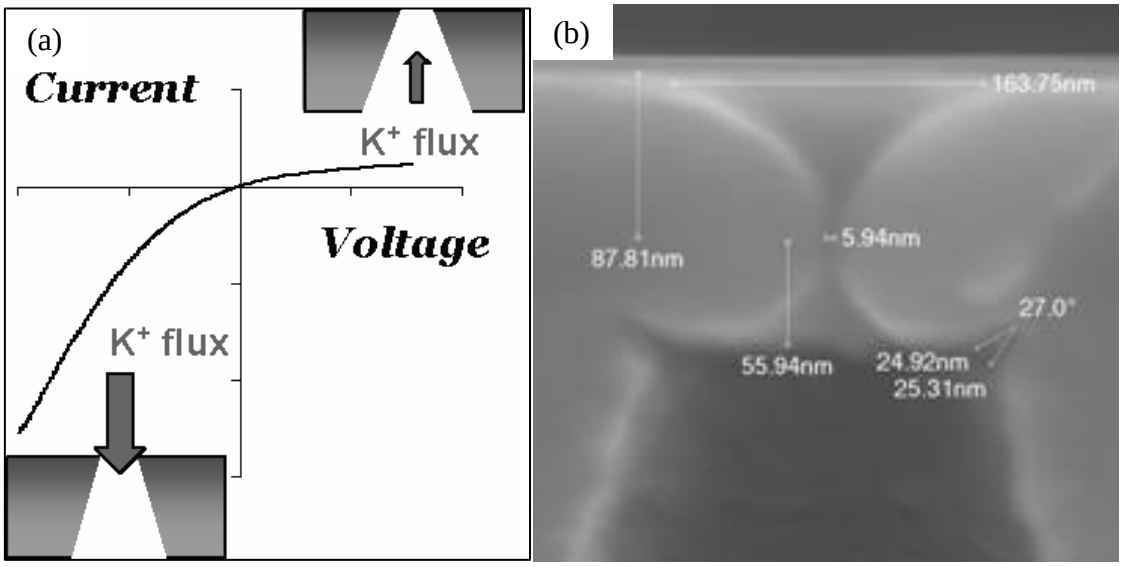


Figure 7.1: (a) Ion current rectification in an asymmetric nanopore (b) An asymmetric nanopore with a pore opening ~ 6 nm fabricated using pulsed PECVD. Figure 7.1 (a) adapted by permission from John Wiley and Sons Publishers Ltd: Advanced Functional Materials[5], copyright (2006).

Due to presence of two distinct growth modes in pulsed PECVD, it is possible to tune the geometry to fabricate asymmetric nanopores. In addition, the self-limiting nature of this deposition technique means that high degree of precision can be obtained over the final pore size. Figure 7.1 (b) shows an asymmetric nanopore fabricated in our laboratory using pulsed PECVD. For fabricating this nanopore, the relative contribution of the PVD-like growth mode ('*R*') was kept much higher in comparison to the contribution of the ALD-like growth mode. This leads to deposition predominantly near the pore mouth with very little deposition inside the feature. As discussed below, it is expected that such a 'bullet-shaped' nanopore would yield very high current rectification ratios.

The electrostatic potential inside a nanopore containing charged pore walls can be modeled by assuming Debye-like interactions between the ions[5]. Figure 7.2 displays a plot comparing the calculated electrostatic potential inside a conical track-etched pore (Figure 7.1(a)) with that inside an asymmetric nanopore fabricated using pulsed PECVD (Figure 7.1(b)). In case of the conical track-etched pore, the potential minimum is located at the pore tip and it gradually tapers to zero along the length of the pore. However, in case of the asymmetric nanopore shown in Figure 7.1(b), the electrostatic potential inside the pore is a step function due to the highly non-conformal step coverage in pulsed PECVD. This step-like electrostatic potential behavior inside a nanopore is expected to lead to much improved diode-like properties.

In majority of the studies, geometry of the nanopores is never rigorously determined. It is usually presumed to be either cylindrical or conical, or in other cases it is deduced semi-empirically from electrical conductivity measurements. The feature scale model developed in this research would be very useful for systematically correlating geometry of the nanopores to their rectification properties. The nanopore geometry can be systematically varied by changing

the growth per cycle and precursor exposure levels in pulsed PECVD. Finally, it is expected that metal oxides like aluminum oxide used for modifying model pores will automatically create charged pore walls. Alternatively, surface of the nanopore can be functionalized with groups such as 3-aminopropyltriethoxysilane (APTS) to anchor charged amino groups on the nanopore walls, which would yield positively charged pore walls at low pH.

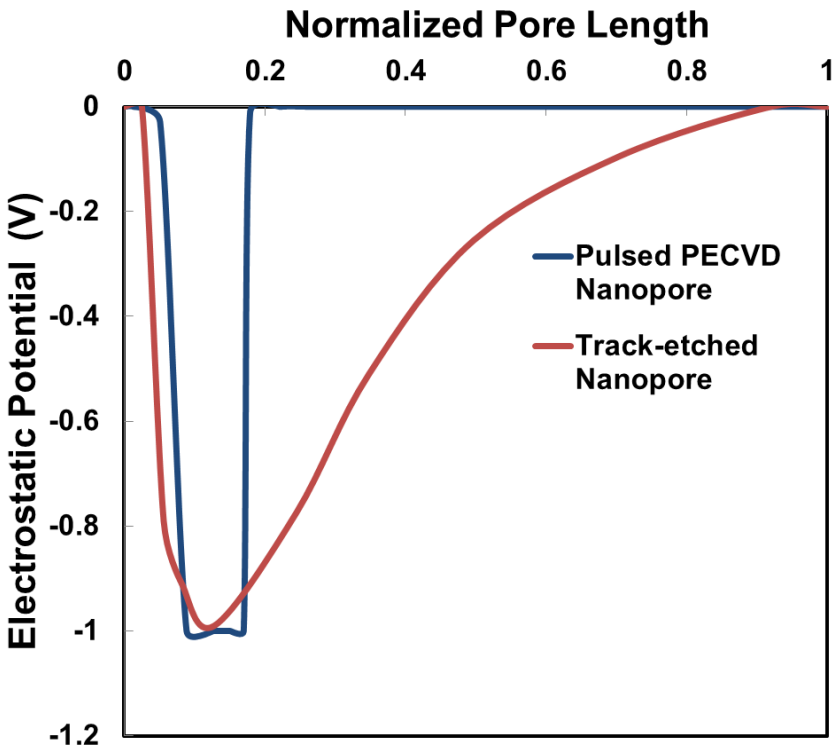


Figure 7.2: (a) Estimated electrostatic potential as a function of normalized pore length in a conical track-etched pore[5] and an asymmetric nanopore fabricated using pulsed PECVD.

7.2.2 Future Work: Surface Functionalization of Nanopores

Many techniques have been devised to control the surface characteristics of membrane supports in an effort to manipulate transport properties of macromolecules inside the membrane pores. In pores modified by self-assembled monolayers (SAMs), the transport of species inside

the pore can be controlled by the functional headgroups of the SAM. We propose to combine precise pore size control of model supports with surface modification using SAMs to fabricate membranes tailored for different applications. Our previous work explored the attachment of OTS SAMs on planar metal oxide surfaces. Subsequently, this protocol was to be extended to membranes fabricated in this work in order to create hydrophobic pore walls. However, the underlying polymeric TE membrane supports were found to degenerate in the heptane solvent used during the silanation process.

It is suggested in this work to employ anodized aluminum oxide (AAO) membrane supports as starting templates for the pore modification work. Like TE membrane supports, AAO membranes contain high aspect ratio pores with a narrow pore size distribution. These membrane supports are stable in a variety of organic solvents, and a variety of polymeric molecules can be immobilized on the pore surface by using grafting techniques[132]. Grafting is a solution-based process, and it occurs by immersing a membrane into a grafting solution which usually contains polymer chains, a linking molecule and a catalyst. Grafting techniques have been used in previous studies to attach polyethylene glycol (PEG)[133] and poly (acrylic acid) (PAA) to the pore walls[134]. PEG is commonly used to construct hydrophilic and protein- resistant surfaces. This is critical in order to prevent membrane fouling in membrane supports that contact biological fluids. In addition, PEG-modified nanopores can be used to separate proteins based on their hydrophilic nature as these hydrophilic protein solutes would diffuse at a much higher rate as compared to their hydrophobic counterparts.

PAA is another molecule that can be easily attached to the pore walls using grafting. At high pH conditions, PAA-coated pore walls would be negatively charged due to carboxyl groups. These charged nanopores should demonstrate ion current rectification characteristics described

previously. These nanopores can also be used to separate charged solutes based on their interactions with charged pore walls. In the absence of electric field, the transport of a charged solute through the pores is governed by diffusion which drives the solute from a region of high concentration to a region of low concentration. In the presence of an applied electric field electro-osmotic and electrophoretic forces will contribute to the flux of the charged solute.

REFERENCES

1. Li, J., et al., *Ion-beam sculpting at nanometre length scales.* Nature, 2001. **412**(6843): p. 166-169.

2. Dekker, C., *Solid-state nanopores.* Nature nanotechnology, 2007. **2**(4): p. 209-215.

3. Storm, A., et al., *Fabrication of solid-state nanopores with single-nanometre precision.* Nature materials, 2003. **2**(8): p. 537-540.

4. Deamer, D.W. and M. Akeson, *Nanopores and nucleic acids: prospects for ultrarapid sequencing.* Trends in biotechnology, 2000. **18**(4): p. 147-151.

5. Siwy, Z.S., *Ion-Current Rectification in Nanopores and Nanotubes with Broken Symmetry.* Advanced Functional Materials, 2006. **16**(6): p. 735-746.

6. Nam, S.-W., et al., *Ionic field effect transistors with sub-10 nm multiple nanopores.* Nano letters, 2009. **9**(5): p. 2044-2048.

7. Ali, M., et al., *Biosensing with functionalized single asymmetric polymer nanochannels.* Macromolecular bioscience, 2010. **10**(1): p. 28-32.

8. Venkatesan, B.M. and R. Bashir, *Nanopore sensors for nucleic acid analysis.* Nature nanotechnology, 2011. **6**(10): p. 615-624.

9. Velleman, L., J. Shapter, and D. Losic, *Gold nanotube membranes functionalised with fluorinated thiols for selective molecular transport.* Journal of Membrane Science, 2009. **328**(1): p. 121-126.

10. Ku, J.-R., et al., *pH and ionic strength effects on amino acid transport through Au-nanotubule membranes charged with self-assembled monolayers.* The Journal of Physical Chemistry C, 2007. **111**(7): p. 2965-2973.

11. Lee, S.B., et al., *Antibody-based bio-nanotube membranes for enantiomeric drug separations.* Science, 2002. **296**(5576): p. 2198-2200.

12. Kasianowicz, J.J., et al., *Characterization of individual polynucleotide molecules using a membrane channel.* Proceedings of the National Academy of Sciences, 1996. **93**(24): p. 13770-13773.

13. Derrington, I.M., et al., *Nanopore DNA sequencing with MspA.* Proceedings of the National Academy of Sciences, 2010. **107**(37): p. 16060-16065.

14. Stein, D.M., et al., *Feedback-controlled ion beam sculpting apparatus.* Review of Scientific Instruments, 2004. **75**(4): p. 900-905.

15. Howorka, S. and Z. Siwy, *Nanopore analytics: sensing of single molecules.* Chemical Society Reviews, 2009. **38**(8): p. 2360-2384.

16. Bayley, H., O. Braha, and L.Q. Gu, *Stochastic sensing with protein pores.* Advanced Materials, 2000. **12**(2): p. 139-142.

17. Van den Hout, M., et al., *Controlling nanopore size, shape and stability.* Nanotechnology, 2010. **21**(11): p. 115304.

18. Apel, P., *Track etching technique in membrane technology.* Radiation Measurements, 2001. **34**(1): p. 559-566.

19. George, S.M., *Atomic layer deposition: an overview.* Chemical reviews, 2009. **110**(1): p. 111-131.

20. Ritala, M. and M. Leskela, *Atomic layer deposition.* Handbook of thin film materials, 2001. **1**: p. 103-159.

21. Leskelä, M. and M. Ritala, *Atomic layer deposition chemistry: recent developments and future challenges.* Angewandte Chemie International Edition, 2003. **42**(45): p. 5548-5554.

22. Groner, M., et al., *Low-temperature Al_2O_3 atomic layer deposition.* Chemistry of Materials, 2004. **16**(4): p. 639-645.

23. Kelkar, S.S. and C.A. Wolden, *Feature scale modeling of pulsed plasma-enhanced chemical vapor deposition.* Journal of Vacuum Science & Technology B, 2014. **32**(5): p. 052001.

24. Seman, M.T., et al., *Enhancement of metal oxide deposition rate and quality using pulsed plasma-enhanced chemical vapor deposition at low frequency.* Journal of Vacuum Science & Technology A, 2008. **26**(5): p. 1213-1217.

25. Seman, M.T., et al., *An Analysis of the Deposition Mechanisms involved during Self-Limiting Growth of Aluminum Oxide by Pulsed PECVD.* Chemical Vapor Deposition, 2008. **14**(9-10): p. 296-302.

26. Rowlette, P.C., M. Canon, and C.A. Wolden, *Digital Control of SiO_2 Film Deposition at Room Temperature.* The Journal of Physical Chemistry C, 2009. **113**(17): p. 6906-6909.

27. Kubala, N.G., P.C. Rowlette, and C.A. Wolden, *Self-Limiting Deposition of Anatase TiO_2 at Low Temperature by Pulsed PECVD.* Electrochemical and Solid-State Letters, 2009. **12**(7): p. H259-H262.

28. Rowlette, P.C., et al., *Self-limiting deposition of semiconducting ZnO by pulsed plasma-enhanced chemical vapor deposition.* Journal of Vacuum Science & Technology A, 2009. **27**(4): p. 761-766.

29. Szymanski, S.F., M.T. Seman, and C.A. Wolden, *Plasma and gas-phase characterization of a pulsed plasma-enhanced chemical vapor deposition system engineered for self-limiting growth of aluminum oxide thin films.* Surface and Coatings Technology, 2007. **201**(22): p. 8991-8997.

30. Seman, M., et al., *Self-limiting growth of tantalum oxide thin films by pulsed plasma-enhanced chemical vapor deposition.* Applied physics letters, 2007. **90**(13).

31. Asatekin, A. and K.K. Gleason, *Polymeric nanopore membranes for hydrophobicity-based separations by conformal initiated chemical vapor deposition.* Nano letters, 2010. **11**(2): p. 677-686.

32. Ganguli, S., S.P. Costello, and W.N. Gill, *Theory of free boundary step coverage in chemical vapor deposition.* Industrial & engineering chemistry research, 1995. **34**(10): p. 3380-3391.

33. Raupp, G.B. and T. Cale, *Step coverage prediction in low-pressure chemical vapor deposition.* Chemistry of Materials, 1989. **1**(2): p. 207-214.

34. Sethian, J.A. and D. Adalsteinsson, *An overview of level set methods for etching, deposition, and lithography development.* Semiconductor Manufacturing, IEEE Transactions on, 1997. **10**(1): p. 167-184.

35. Donea, J., S. Giuliani, and J. Halleux, *An arbitrary Lagrangian-Eulerian finite element method for transient dynamic fluid-structure interactions.* Computer methods in applied mechanics and engineering, 1982. **33**(1): p. 689-723.

36. Gordon, R.G., et al., *A kinetic model for step coverage by atomic layer deposition in narrow holes or trenches.* Chemical Vapor Deposition, 2003. **9**(2): p. 73-78.

37. Rowlette, P., *Pulsed Plasma-Enhanced Chemical Vapor Deposition of Nanolaminates and Metal Oxide Alloys*. PhD Dissertation, Colorado School of Mines, 2009.

38. http://www.jawoollam.com/tutorial.

39. Lamour, G., et al., *Contact angle measurements using a simplified experimental setup.* Journal of chemical education, 2010. **87**(12): p. 1403-1407.

40. Mirji, S., *Octadecyltrichlorosilane adsorption kinetics on Si (100)/SiO_2 surface: contact angle, AFM, FTIR and XPS analysis.* Surface and interface analysis, 2006. **38**(3): p. 158-165.

41. Joachim, C., J. Gimzewski, and A. Aviram, *Electronics using hybrid-molecular and mono-molecular devices.* Nature, 2000. **408**(6812): p. 541-548.

42. Stupp, S.I. and P.V. Braun, *Molecular manipulation of microstructures: biomaterials, ceramics, and semiconductors.* Science, 1997. **277**(5330): p. 1242-1248.

43. Chen, P., et al., *Atomic layer deposition to fine-tune the surface properties and diameters of fabricated nanopores.* Nano Letters, 2004. **4**(7): p. 1333-1337.

44. Ott, A., et al., *Modification of porous alumina membranes using Al_2O_3 atomic layer controlled deposition.* Chemistry of materials, 1997. **9**(3): p. 707-714.

45. Li, J., et al., *DNA molecules and configurations in a solid-state nanopore microscope.* Nature materials, 2003. **2**(9): p. 611-615.

46. McCool, B.A. and W.J. Desisto, *Self-Limited Pore Size Reduction of Mesoporous Silica Membranes via Pyridine-Catalyzed Silicon Dioxide ALD.* Chemical Vapor Deposition, 2004. **10**(4): p. 190-194.

47. Xiong, G., et al., *Effect of atomic layer deposition coatings on the surface structure of anodic aluminum oxide membranes.* The Journal of Physical Chemistry B, 2005. **109**(29): p. 14059-14063.

48. Cervera, J., et al., *Asymmetric nanopore rectification for ion pumping, electrical power generation, and information processing applications.* Electrochimica Acta, 2011. **56**(12): p. 4504-4511.

49. Howorka, S. and Z.S. Siwy, *Nanopores as protein sensors.* Nature biotechnology, 2012. **30**(6): p. 506-507.

50. Cale, T. and G. Raupp, *A unified line-of-sight model of deposition in rectangular trenches.* Journal of Vacuum Science & Technology B, 1990. **8**(6): p. 1242-1248.

51. Hasper, A., et al., *Modeling and optimization of the step coverage of tungsten LPCVD in trenches and contact holes.* Journal of the Electrochemical Society, 1991. **138**(6): p. 1728-1738.

52. Musson, L.C., et al., *Feature length-scale modeling of LPCVD and PECVD MEMS fabrication processes.* Microsystem technologies, 2005. **12**(1-2): p. 137-142.

53. Cale, T. and G. Raupp, *Free molecular transport and deposition in cylindrical features.* Journal of Vacuum Science & Technology B, 1990. **8**(4): p. 649-655.

54. Cale, T., T. Gandy, and G. Raupp, *A fundamental feature scale model for low pressure deposition processes.* Journal of Vacuum Science & Technology A, 1991. **9**(3): p. 524-529.

55. Cale, T., G. Raupp, and T. Gandy, *Free molecular transport and deposition in long rectangular trenches.* Journal of applied physics, 1990. **68**(7): p. 3645-3652.

56. Ikegawa, M. and J. Kobayashi, *Deposition profile simulation using the direct simulation Monte Carlo method.* Journal of the Electrochemical Society, 1989. **136**(10): p. 2982-2986.

57. Cooke, M. and G. Harris, *Monte Carlo simulation of thin-film deposition in a rectangular groove.* Journal of Vacuum Science & Technology A, 1989. **7**(6): p. 3217-3221.

58. IslamRaja, M.M., et al., *A 3-dimensional model for low-pressure chemical-vapor-deposition step coverage in trenches and circular vias.* Journal of applied physics, 1991. **70**(11): p. 7137-7140.

59. Liao, H. and T.S. Cale, *Low-Knudsen-number transport and deposition.* Journal of Vacuum Science & Technology A, 1994. **12**(4): p. 1020-1026.

60. McVittie, J.P., et al. *SPEEDIE: A profile simulator for etching and deposition*. in *Santa Cl-DL tentative*. 1991. International Society for Optics and Photonics.

61. Donea, J., et al., *Arbitrary Lagrangian–Eulerian methods.* Encyclopedia of computational mechanics, 2004.

62. Elam, J., et al., *Conformal coating on ultrahigh-aspect-ratio nanopores of anodic alumina by atomic layer deposition.* Chemistry of Materials, 2003. **15**(18): p. 3507-3517.

63. Kucheyev, S., et al., *Mechanisms of atomic layer deposition on substrates with ultrahigh aspect ratios.* Langmuir, 2008. **24**(3): p. 943-948.

64. Gobbert, M.K., V. Prasad, and T.S. Cale, *Predictive modeling of atomic layer deposition on the feature scale.* Thin Solid Films, 2002. **410**(1): p. 129-141.

65. Adomaitis, R.A., *Development of a multiscale model for an atomic layer deposition process.* Journal of Crystal Growth, 2010. **312**(8): p. 1449-1452.

66. Adomaitis, R.A., *A Ballistic Transport and Surface Reaction Model for Simulating Atomic Layer Deposition Processes in High-Aspect-Ratio Nanopores.* Chemical Vapor Deposition, 2011. **17**(10-12): p. 353-365.

67. Dendooven, J., et al., *Modeling the conformality of atomic layer deposition: The effect of sticking probability.* Journal of The Electrochemical Society, 2009. **156**(4): p. P63-P67.

68. Pan, M., et al., *CVD modification and vapor/gas separation properties of nanoporous alumina membranes.* Journal of membrane science, 1999. **158**(1): p. 235-241.

69. Li, F., et al., *Modification of ceramic membranes for pore structure tailoring: The atomic layer deposition route.* Journal of Membrane Science, 2012. **397**: p. 17-23.

70. Ito, T., et al., *Development of a molecular recognition ion gating membrane and estimation of its pore size control.* Journal of the American Chemical Society, 2002. **124**(26): p. 7840-7846.

71. Jirage, K.B., J.C. Hulteen, and C.R. Martin, *Nanotubule-based molecular-filtration membranes.* Science, 1997. **278**(5338): p. 655-658.

72. Li, Y.-Y., et al., *Fabrication of carbon coated ceramic membranes by pyrolysis of methane using a modified chemical vapor deposition apparatus.* Journal of membrane science, 2002. **197**(1): p. 23-35.

73. Araki, S., et al., *Synthesis, characterization and gas permeation properties of a silica membrane prepared by high-pressure chemical vapor deposition.* Journal of membrane science, 2007. **290**(1): p. 138-145.

74. Grigoras, K., V.-M. Airaksinen, and S. Franssila, *Coating of nanoporous membranes: atomic layer deposition versus sputtering.* Journal of nanoscience and nanotechnology, 2009. **9**(6): p. 3763-3770.

75. Li, F., et al., *Precise pore size tuning and surface modifications of polymeric membranes using the atomic layer deposition technique.* Journal of Membrane Science, 2011. **385**: p. 1-9.

76. Wang, Q., et al., *PVDF membranes with simultaneously enhanced permeability and selectivity by breaking the tradeoff effect via atomic layer deposition of TiO_2.* Journal of Membrane Science, 2013. **442**: p. 57-64.

77. Deen, W., M. Bohrer, and N. Epstein, *Effects of molecular size and configuration on diffusion in microporous membranes.* AIChE Journal, 1981. **27**(6): p. 952-959.

78. Deen, W., *Hindered transport of large molecules in liquid-filled pores.* AIChE Journal, 1987. **33**(9): p. 1409-1425.

79. Xu, Q., et al., *Hydrophilization of porous polypropylene membranes by atomic layer deposition of TiO_2 for simultaneously improved permeability and selectivity.* Journal of Membrane Science, 2013. **448**: p. 215-222.

80. Tavakolmoghadam, M., et al., *Surface modification of PVDF membranes by sputtered TiO_2: fouling reduction potential in membrane bioreactors.* Desalination and Water Treatment, 2014(ahead-of-print): p. 1-11.

81. Tang, C.Y., Y.-N. Kwon, and J.O. Leckie, *Effect of membrane chemistry and coating layer on physiochemical properties of thin film composite polyamide RO and NF*

membranes: II. Membrane physiochemical properties and their dependence on polyamide and coating layers. Desalination, 2009. **242**(1): p. 168-182.

82. Ulbricht, M., *Advanced functional polymer membranes.* Polymer, 2006. **47**(7): p. 2217-2262.

83. Cha, S. and W. Lee, *Performance of proton exchange membrane fuel cell electrodes prepared by direct deposition of ultrathin platinum on the membrane surface.* Journal of the Electrochemical Society, 1999. **146**(11): p. 4055-4060.

84. Profijt, H., et al., *Plasma-assisted atomic layer deposition: Basics, opportunities, and challenges.* Journal of Vacuum Science & Technology A, 2011. **29**(5): p. 050801.

85. Szymanski, S.F., P. Rowlette, and C.A. Wolden, *Self-limiting deposition of aluminum oxide thin films by pulsed plasma-enhanced chemical vapor deposition.* J. Vac. Sci. Technol., A, 2008. **26**: p. 1079-1084.

86. Patel, R.P. and C.A. Wolden, *Defect analysis and mechanical performance of plasma-deposited thin films on flexible polycarbonate substrates.* Applied Surface Science, 2013. **268**: p. 416-424.

87. Jun, Y., et al., *Functionalized titania nanotube composite membranes for high temperature proton exchange membrane fuel cells.* International Journal of Hydrogen Energy, 2011. **36**(10): p. 6073-6081.

88. Jain, M.K., T.S. Cale, and T.H. Gandy, *Comparison of LPCVD Film Conformalities Predicted by Ballistic Transport-Reaction and Continuum Diffusion-Reaction Models.* Journal of The Electrochemical Society, 1993. **140**(1): p. 242-247.

89. Seel, S.C., et al., *Tensile stress evolution during deposition of Volmer–Weber thin films.* Journal of Applied Physics, 2000. **88**(12): p. 7079-7088.

90. Thornton, J.A., *The microstructure of sputter-deposited coatings.* Journal of Vacuum Science & Technology A, 1986. **4**(6): p. 3059-3065.

91. Cheng, H.-E. and C.-C. Chen, *Morphological and photoelectrochemical properties of ALD TiO_2 films.* Journal of the electrochemical society, 2008. **155**(9): p. D604-D607.

92. Ritala, M., et al., *Growth of titanium dioxide thin films by atomic layer epitaxy.* Thin Solid Films, 1993. **225**(1): p. 288-295.

93. Kelkar, S.S., D. Chiavetta, and C.A. Wolden, *Formation of octadecyltrichlorosilane (OTS) self-assembled monolayers on amorphous alumina.* Applied Surface Science, 2013. **282**: p. 291-296.

94. Liu, J., et al., *Hybrid mesoporous materials with functionalized monolayers.* Advanced Materials, 1998. **10**(2): p. 161-165.

95. Onclin, S., B.J. Ravoo, and D.N. Reinhoudt, *Engineering silicon oxide surfaces using Self-Assembled monolayers.* Angewandte Chemie International Edition, 2005. **44**(39): p. 6282-6304.

96. Midwood, K.S., et al., *Easy and efficient bonding of biomolecules to an oxide surface of silicon.* Langmuir, 2004. **20**(13): p. 5501-5505.

97. Lercel, M., et al., *Pattern transfer of electron beam modified self-assembled monolayers for high-resolution lithography.* Journal of Vacuum Science & Technology B, 1995. **13**(3): p. 1139-1143.

98. Clear, S.C. and P.F. Nealey, *Lateral force microscopy study of the frictional behavior of self-assembled monolayers of octadecyltrichlorosilane on silicon/silicon dioxide immersed in n-alcohols.* Langmuir, 2001. **17**(3): p. 720-732.

99. Kulkarni, S.A., et al., *Growth kinetics and thermodynamic stability of octadecyltrichlorosilane self-assembled monolayer on Si (100) substrate.* Materials Letters, 2005. **59**(29): p. 3890-3895.

100. Wasserman, S.R., Y.T. Tao, and G.M. Whitesides, *Structure and reactivity of alkylsiloxane monolayers formed by reaction of alkyltrichlorosilanes on silicon substrates.* Langmuir, 1989. **5**(4): p. 1074-1087.

101. Stevens, M.J., *Thoughts on the structure of alkylsilane monolayers.* Langmuir, 1999. **15**(8): p. 2773-2778.

102. Rozlosnik, N., M.C. Gerstenberg, and N.B. Larsen, *Effect of solvents and concentration on the formation of a self-assembled monolayer of octadecylsiloxane on silicon (001).* Langmuir, 2003. **19**(4): p. 1182-1188.

103. Li, C.P., et al., *Improved durability of WO_3 nanocomposite films using atomic layer and vapor deposited coatings.* ECS Electrochemistry Letters, 2012. **1**(5): p. H24-H27.

104. Furneaux, R., W. Rigby, and A. Davidson, *The formation of controlled-porosity membranes from anodically oxidized aluminium.* Nature, 1989. **337**(6203): p. 147-149.

105. Hsieh, H., R. Bhave, and H.L. Fleming, *Microporous alumina membranes.* Journal of membrane science, 1988. **39**(3): p. 221-241.

106. Finch, D.S., et al., *Biocompatibility of atomic layer-deposited alumina thin films.* Journal of Biomedical Materials Research Part A, 2008. **87**(1): p. 100-106.

107. Adiga, S.P., et al., *Nanoporous materials for biomedical devices.* Jom, 2008. **60**(3): p. 26-32.

108. Mitchon, L.N. and J. White, *Growth and analysis of octadecylsiloxane monolayers on Al_2O_3 (0001).* Langmuir, 2006. **22**(15): p. 6549-6554.

109. Allara, D.L. and R.G. Nuzzo, *Spontaneously organized molecular assemblies. 1. Formation, dynamics, and physical properties of n-alkanoic acids adsorbed from solution on an oxidized aluminum surface.* Langmuir, 1985. **1**(1): p. 45-52.

110. Thompson, W.R. and J.E. Pemberton, *Characterization of octadecylsilane and stearic acid layers on Al_2O_3 surfaces by Raman spectroscopy.* Langmuir, 1995. **11**(5): p. 1720-1725.

111. Houssiau, L. and P. Bertrand, *ToF–SIMS study of organosilane self-assembly on aluminum surfaces.* Applied surface science, 2001. **175**: p. 351-356.

112. Brzoska, J., I.B. Azouz, and F. Rondelez, *Silanization of solid substrates: a step toward reproducibility.* Langmuir, 1994. **10**(11): p. 4367-4373.

113. Angst, D.L. and G.W. Simmons, *Moisture absorption characteristics of organosiloxane self-assembled monolayers.* Langmuir, 1991. **7**(10): p. 2236-2242.

114. Poda, A., A. Anderson, and W. Ashurst, *Self-assembled octadecyltrichlorosilane monolayer formation on a highly hydrated silica film.* Applied Surface Science, 2010. **256**(22): p. 6805-6813.

115. Bunker, B.C., et al., *The impact of solution agglomeration on the deposition of self-assembled monolayers.* Langmuir, 2000. **16**(20): p. 7742-7751.

116. Yang, S.-R. and B.O. Kolbesen, *A comparative study of the growth of octadecyltrichlorosilane and 3-mercaptopropyltrimethoxysilane self-assembled monolayers on hydrophilic silicon surfaces.* Applied Surface Science, 2008. **255**(5): p. 1726-1735.

117. Manifar, T., et al., *Formation of uniform self-assembly monolayers by choosing the right solvent: OTS on silicon wafer, a case study.* Applied Surface Science, 2008. **254**(15): p. 4611-4619.

118. Devynck, M., et al., *Organic field-effect transistor with octadecyltrichlorosilane (OTS) self-assembled monolayers on gate oxide: effect of OTS quality.* The European Physical Journal Applied Physics, 2011. **56**(03): p. 34106.

119. Cha, K.-H. and D.-E. Kim, *Investigation of the tribological behavior of octadecyltrichlorosilane deposited on silicon.* Wear, 2001. **251**(1): p. 1169-1176.

120. Hancer, M., *The effect of humidity on the stability of octadecyltrichlorosilane for the self-assembled monolayer coating applications.* Progress in Organic Coatings, 2008. **63**(4): p. 395-398.

121. Almanza-Workman, A.M., et al., *Characterization of highly hydrophobic coatings deposited onto pre-oxidized silicon from water dispersible organosilanes.* Thin Solid Films, 2003. **423**(1): p. 77-87.

122. Mathauer, K. and C.W. Frank, *Binary self-assembled monolayers as prepared by successive adsorption of alkyltrichlorosilanes.* Langmuir, 1993. **9**(12): p. 3446-3451.

123. Brugnara, M., *Contact Angle Plugin (for ImageJ software)*. 2006.

124. Luo, S. and C. Wong, *Effect of UV/ozone treatment on surface tension and adhesion in electronic packaging.* Components and Packaging Technologies, IEEE Transactions on, 2001. **24**(1): p. 43-49.

125. Zhang, Y., R.H. Terrill, and P.W. Bohn, *Ultraviolet photochemistry and ex situ ozonolysis of alkanethiol self-assembled monolayers on gold.* Chemistry of materials, 1999. **11**(8): p. 2191-2198.

126. Jung, M.-H. and H.-S. Choi, *Characterization of octadecyltrichlorosilane self-assembled monolayers on silicon (100) surface.* Korean journal of chemical engineering, 2009. **26**(6): p. 1778-1784.

127. Karpovich, D. and G. Blanchard, *Direct measurement of the adsorption kinetics of alkanethiolate self-assembled monolayers on a microcrystalline gold surface.* Langmuir, 1994. **10**(9): p. 3315-3322.

128. Tillman, N., et al., *Incorporation of phenoxy groups in self-assembled monolayers of trichlorosilane derivatives. Effects on film thickness, wettability, and molecular orientation.* Journal of the American Chemical Society, 1988. **110**(18): p. 6136-6144.

129. Kim, H.K., et al., *Thermal decomposition of alkylsiloxane self-assembled monolayers in air.* The Journal of Physical Chemistry B, 2003. **107**(18): p. 4348-4351.

130. Apel, P.Y., et al., *Effect of nanopore geometry on ion current rectification.* Nanotechnology, 2011. **22**(17): p. 175302.

131. Jiang, Z. and D. Stein, *Charge regulation in nanopore ionic field-effect transistors.* Physical Review E, 2011. **83**(3): p. 031203.

132. Aramesh, M. and J. Cervenka, *Surface Modification of Porous Anodic Alumina for Medical and Biological Applications.*

133. Popat, K.C., et al., *Surface modification of nanoporous alumina surfaces with poly (ethylene glycol).* Langmuir, 2004. **20**(19): p. 8035-8041.

134. Nagale, M., B.Y. Kim, and M.L. Bruening, *Ultrathin, hyperbranched poly (acrylic acid) membranes on porous alumina supports.* Journal of the American Chemical Society, 2000. **122**(47): p. 11670-11678.

APPENDIX A

FABRICATION OF SILICON MODEL SUPPORTS

The pore modification strategy employed in this work was predicated by the availability of well-defined model supports. The initial plan was to fabricate model supports in silicon on insulator (SOI) wafers at the Center for Nanophase Materials Sciences, a user facility at the Oak Ridge National Laboratory.

The device envisaged in this work has been described in Figure 3.1. Briefly, it consists of an active region containing all the holes. This active region opens up into a much larger window region. The final device is built in the form of 25 mm discs which could easily fit into our membrane testing apparatus. The active region comprises of well-defined holes with a desired pore opening between 100 to 200 nm. The depth of the active region was about 2 μm, and during fabrication, circles with different diameters ~ 100, 134, 170 and 200 nm were patterned on the wafer. The final device was built on a SOI wafer where the oxide insulator served as an etch stop for windows to the active region.

Figure A.1 shows the steps involved in fabricating these silicon supports. As mentioned before, the device was fabricated on a SOI wafer. The first step is depositing a mask on the silicon device layer. Masks employed in this work included the electron-beam resist itself, PECVD oxide and chrome. Due to pinhole defects in the PECVD oxide layer and poor pattern transfer in the chrome layer, the resist was used as a mask for fabricating majority of these devices. The next processing step involved spin-coating about 400 nm of resist on the wafer. Subsequently, e-beam writer is used to pattern an array of regularly spaced circles on the resist.

The resist is developed and the mask is subsequently etched to transfer the pattern from the resist to the underlying mask layer. In case, the resist itself acts as a mask, this step is redundant.

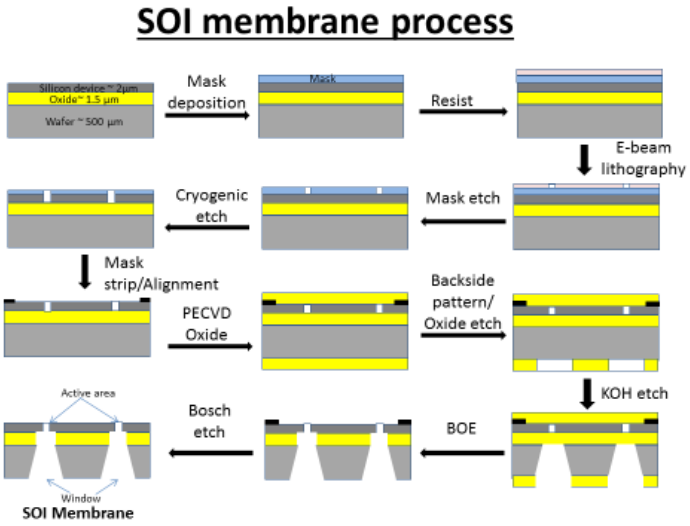


Figure A.1: Processes involved in fabrication of model supports in a SOI wafer.

The next process is the most crucial fabrication step, and involves transfer of pattern from the mask to the underlying silicon layer using cryogenic etch. Deep cryogenic etch has been developed as a promising alternative to Bosch etch in many applications. The substrate is cooled to cryogenic temperatures as low as -100 °C, and etching takes place in SF_6/O_2 plasma. The sidewalls of the feature are passivated by a layer of SiO_xF_y, while the bottom of the feature is etched by fluorine radicals. The main etching reactions consist of spontaneous etching and ion-assisted reactions.

In contrast to Bosch process, scalloping of the etch profile is avoided in cryogenic etch leading to smooth etch profiles. However, cryogenic etch process is very sensitive to temperature shifts which can cause either the passivation or etch processes to dominate.

The objective of optimizing a cryogenic etch process is to obtain high etch rates for silicon while maintaining the correct etch profile. There are many parameters which can be tuned

to optimize the etch profile. In this work, oxygen flowrate and capactively coupled plasma (CCP) power were varied to optimize the etch profile and etch rate. Increasing CCP power produces almost vertical sidewalls. However, this is accompanied by increase in the etch rate of the mask which makes it very difficult to achieve the target depth of 2 µm. Oxygen is responsible for formation of the SiO_xF_y passivation layer, and increasing the oxygen flowrate decreases the etch rate and also reduces undercutting near the feature mouth. Figure A.2 shows the parameter space explored during our study. Oxygen flow rate was varied from 12 to 22 sccm and the CCP power was varied from 10 to 55 W. The best etch profile was obtained at high oxygen flowrate and CCP power. The etch profile does display some undercutting near the feature mouth but the sidewalls were perfectly vertical inside the feature.

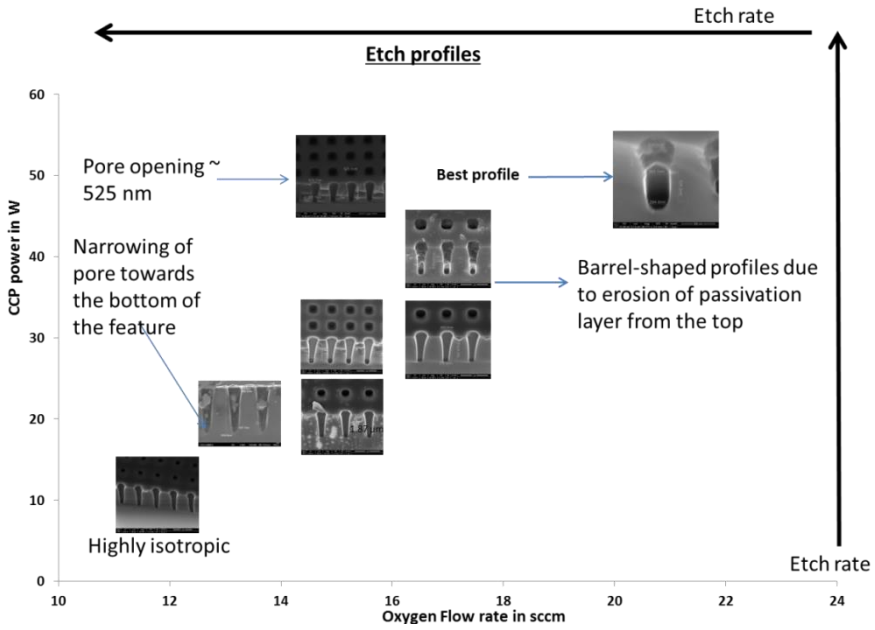


Figure A.2: Etch profiles as a function of CCP power and oxygen flowrate. Best profile is obtained at conditions of high CCP power and oxygen flowrate.

The next steps are related to the opening of the window region. This involves deposition of PECVD oxide layer to protect the active region while the window region is being formed. Finally, Bosch etch is used to go through 300 µm thick silicon wafer to create the final device.

Another phenomenon explored during this study was aspect ratio dependent etching (ARDE). In high aspect ratio etch applications in MEMS and NEMS, features with a wide variation in size have to be etched simultaneously. In this study, 4 different hole sizes were desired. Figure A.3 shows a plot of the etch rate as a function of design aspect ratio. Design aspect ratio is based on the desired etch depth of 2 µm and the diameter of the circle patterned using the electron beam lithography process. The etch rate is maximum for a planar substrate (aspect ratio = 0), and rate steadily decreases for features with higher design aspect ratio.

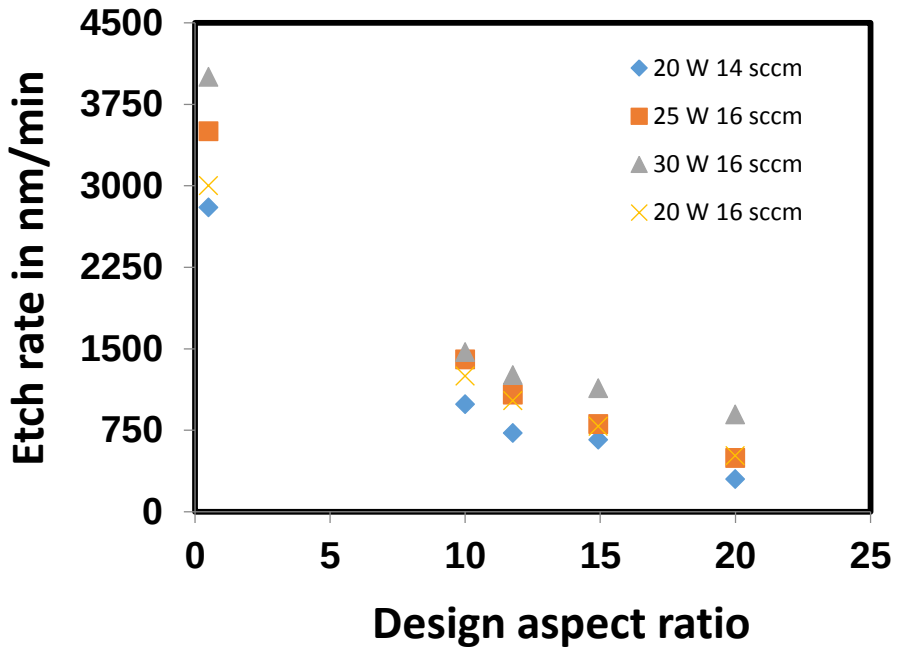


Figure A.3: Etch rate (nm/min) as a function of design aspect ratio. Etch rate decreases as the aspect ratio of the feature increases.

ARDE is a result of Knudsen transport phenomenon, and depletion of fluorine radicals at the bottom of the cylinder is the main cause of ARDE. Higher the aspect ratio more difficult it is for the fluorine radicals to reach the feature bottom. Figure A.4 shows the cross-section micrographs of the etch profiles obtained for features with different aspect ratios. For features with patterned diameter ~ 100 nm, the etch depth is less than 0.5 µm. But an etch depth of ~ 1.5 µm is achieved for a sample with patterned circles with diameters ~ 200 nm.

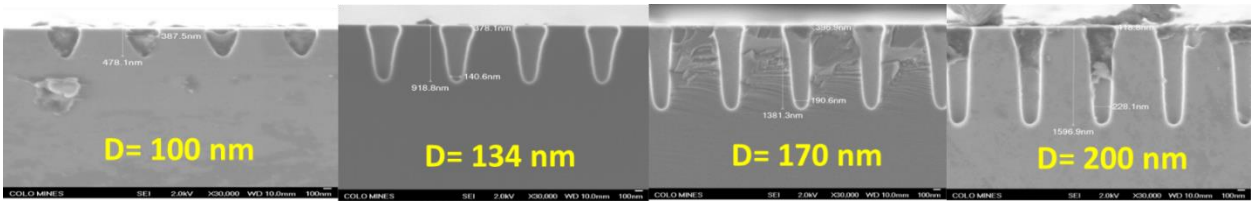


Figure A.4: Cross-section micrographs of etch profiles illustrating ARDE phenomenon.

APPENDIX B

MODELING OF STEADY STATE DEPOSITION PROCESSES

This section contains instructions for simulating the non-conformal deposition profile shown in Figure 2.2 (c). This model can be easily altered to simulate the remaining CVD profiles shown in Figure 2.2 by simply changing the reaction rate employed in this model. The transient pulsed PECVD and non-ideal ALD cases employ the same geometry and physics with a few additions as described in Chapter 2. The modeling instructions for those cases have not been included to avoid repetition.

Modeling Instructions for Simulating PVD-like Deposition Profile shown in Figure 2.2 (c)

New

1. Open COMSOL. In the **New** window, click **Blank**.

Model Wizard

1. In the **Model Builder** window, right click on untitled.mph to create a new model.
2. Select '**2D Axisymmetric**' using the '**Add Component**' option.
3. In the Select Physics tree, select **Chemical Species Transport**>'**Transport of Diluted Species**'.
4. Click Add.
5. In the Select Physics tree, select '**Mathematics**'> '**Deformed Mesh'>'Moving Mesh (ale)**'
6. Click Add.
7. Create another model 'Model2' by choosing 'Add Model' option.

8. Select ‘1 D’ model using the ‘Add Component’ option.
9. Click Study.
10. In the Select Study tree, select ‘**Time Dependent**’.
11. Click Done.

Parameters and Variables

1. On the ‘Home’ toolbar, click on ‘Global Definitions’ and select ‘Parameters’.
2. Enter the following in the textfields.

Name	Expression	Description
cint	7.6/5*10^ - 6[mol/m^3]	Initial Concentration
vcap	101.96*0.25*10^ - 6[m^3/mol]	Molar Volume of Deposition Film
r1	50*10^ - 9[m]	Initial Pore Radius
r2	5*r1	Bulk Domain Radius
h1	400*10^ - 9 [m]	Initial Pore Height
h2	2*h1	Bulk Domain Height
a	h1/(2*r1)	Initial Aspect Ratio
Db	0.0039[m^2/s]	Bulk Diffusion Coefficient
k	82.583[m/s]	Surface Reaction Rate Constant

3. Select ‘Model 1’ > ‘Definitions’ > ‘Variables’.
4. Create a variable ‘pore2d’. Enter mod2.genext1 (pore1d) in the ‘expression’ text-field.
5. Also, create another variable Dk (Knudsen Diffusion coefficient), and enter the following expression in the text field-

‘330[m/s]*(h1*0.25)*((20+8*(h1/(2*pore2d)))/(20+19*(h1/(2*pore2d))+3*(h1/(2*pore2d))^2))+Db*(pore2d>10^-7)’

6. Select general projection operator from ‘component couplings’ which can be found under ‘Definitions’.
7. In the geometric entity level, enter ‘Domain’ and in the ‘Selection’ field enter ‘Manual’.
8. In the ‘Source Map’, enter z and r in the x-expression and y-expression respectively.
9. In the destination map, enter x in the x-expression field.

Geometry

1. In the **‘Geometry’** window, select the length unit ‘m’.

Rectangle (r1)

1. Expand the geometry window and choose ‘rectangle’ from the options.
2. Locate rectangle **‘type’** at the top, and select **‘solid’**.
3. In the settings window, locate **‘size’** and enter ‘**width’** as r1, and **‘height’** as h1.
4. Locate the setting for **‘position’** and select **‘corner’**. Enter 0 for **‘r’** and **‘z’**.

Rectangle (r2)

1. Expand the geometry window and choose **‘rectangle’** from the options.
2. Locate rectangle **‘type’** at the top, and select ‘solid’.
3. In the settings window, locate **‘size’** and enter **‘width’** as r2, and **‘height’** as h2.
4. Locate the setting for ‘position’ and select ‘corner’. Enter 0 and h1 for ‘r’ and ‘z’ respectively.

Fillet and Union

1. Right click on the geometry toolbar and select ‘Boolean operations’> ‘Union’.
2. Select r1 and r2 from the ‘Input objects’

3. Uncheck the ‘Keep Interior boundaries’ option.
4. Right click on the geometry and select ‘Fillet’ option.
5. Add vertices ‘4’ and ‘5’ to the window ‘vertices to fillet’.
6. Enter 20*10^-9 [m] as the ‘radius’. Click ‘Build All Objects’ to complete constructing the model geometry.

Transport of Diluted Species

1. In the Model Builder window, expand the component 1> Transport of Diluted Species, then click ‘Convection and Diffusion 1’. Enter 0 in the velocity field entries.
2. Under ‘Diffusion’ enter ‘Dk’ defined previously as the diffusion coefficient. The ‘if condition’ in the expression is used to include the diffusion coefficient in the bulk domain in the same expression as that of the ‘feature domain’.
3. On the physics toolbar, click ‘Axial Symmetry1’ and select boundaries ‘1’ and ‘3’ only.

Inlet

1. Right click on ‘Transport of Diluted Species’ and select ‘Inflow’ from the options.
2. Select boundary 4 only.
3. Expand the ‘Equation’ toolbar.
4. Enter ‘cint’ in the textfield for ‘concentration’.

Boundaries

4. On the physics toolbar, choose the ‘No Flux’ condition.
5. Select boundary ‘7’ only.
6. On the physics toolbar choose the ‘Flux’ option.
7. Select boundaries 2, 5, 6, 8 and 9.
8. Locate the ‘Inward Flux’ option and check the option for ‘Species c’.

9. In the textfield for ‘Inward flux’ enter ‘-k*c’.

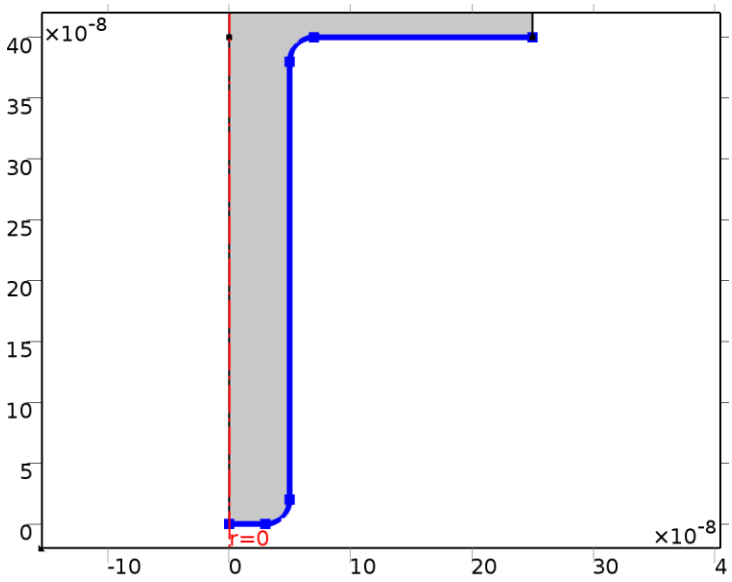


Figure B.1: Feature boundaries highlighted in blue.

Initial Conditions

1. On the physics toolbar, click ‘Initial Values’.
2. Make sure this condition is applicable to the entire domain.
3. Locate the ‘concentration’ section and enter 0 in the textfield for concentration ‘c’.

Moving Mesh

1. On the ‘Moving Mesh’ toolbar, choose ‘Free Deformation’ and select the entire domain. This should over-ride the preselected ‘Fixed Mesh’ option in the ‘Model Builder’ window.
2. Choose ‘Zero Normal Mesh Displacement’ by right-clicking on the ‘Moving Mesh’ option. Apply this option to boundaries 1 and 3 only.
3. Choose ‘Zero Normal Mesh Displacement’ and select the boundaries 4 and 7 only.

4. Choose ‘Prescribed Normal Mesh Velocity’ by right-clicking on ‘Moving Mesh’ toolbar. Select the feature surface by selecting the following boundaries 2, 5, 6, 8 and 9.
5. Locate ‘Normal Mesh velocity’ and enter –(k*c* vcap) in the textfield.
6. Locate the ‘Enable Moving Boundary Smoothing’ field and enable by checking the option.
7. In the ‘Moving boundary smoothing’ parameter enter 0.1.

Mesh

1. Right Click on ‘Meshes’ and select ‘Add Mesh’. Choose ‘Free Triangular’ option.
2. Right click on ‘Free Triangular1’ and choose ‘Size’ from the dropdown options.
3. From the ‘Size’ option select ‘Custom’ option.
4. Enter 2.4 *10^-7, 1.92*10^-8, 1.8, 0.1 and 20 in the textfields for ‘Maximum element size’, ‘Minimum element size’, ‘Maximum element growth rate’, ‘Curvature factor’ and ‘Resolution of narrow regions’ respectively.
5. Click the ‘Build All’ button.

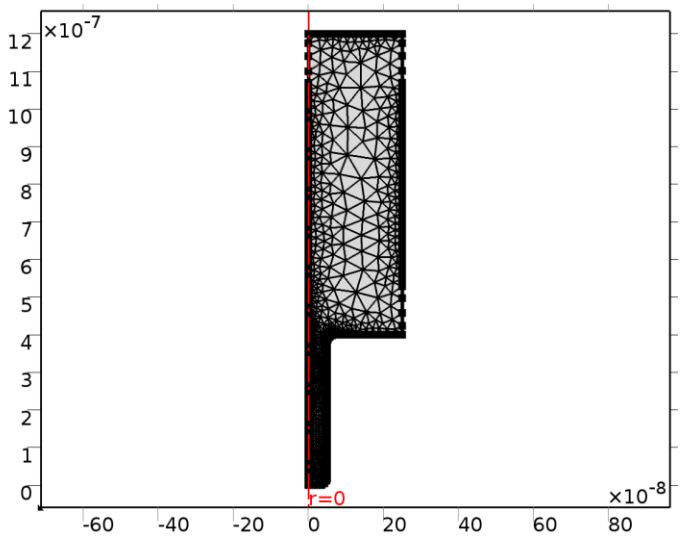


Figure B.2: Initial mesh structure employed in the model.

Model 2

1. Right click on ‘Definitions’ and select ‘variables’.
2. Select ‘Domain’ in the ‘Geometric entity level’, and make sure it is active.
3. Under the variables window, enter ‘pore1d’ in the ‘Name’ field. In the expression field, enter the following ‘mod1.genproj1(1).
4. Select Definitions > Component Coupling > General Extrusion 1.
5. Select ‘Domain’ in the ‘Geometric entity level’, and make sure it is active.
6. In the destination map, enter ‘z’ in the x-expression text-field.
7. Select ‘Spatial (x, y, z)’ in the source frame field.
8. Enter ‘x’ in the x-expression textfield.

Geometry 2

1. Select Model 2 > ‘Geometry 2’>’Interval’.
2. Input 0 in the textfield entry for ‘Left endpoint’.
3. Input (h1+h2) in the textfield entry for ‘Right endpoint’ entry.

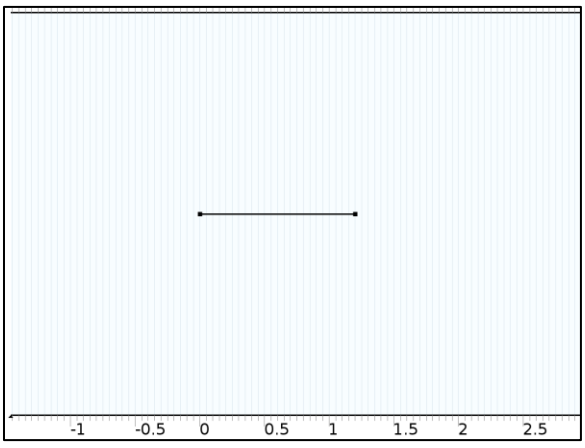


Figure B.3: Geometry employed in model 2. Pore1d is defined in this 1D domain, and is subsequently ‘extruded’ to the 2D model.

Mesh 3

1. Choose ‘Add Mesh’ option from ‘Model 2’ window.
2. Choose ‘Physics-Controlled Mesh’ from the dropdown menu. In the ‘Element Size’ setting, select ‘Extra fine’.

Study

1. In the ‘Model Builder’ window, expand the ‘Study 1’ node, then click Step 1: Time Dependent’
2. In the settings window for ‘Time Dependent’, locate the ‘Study Settings’ section.
3. In the ‘Times’ text field, type range (0, 0.1, 500).
4. Enter 0.00001 in the text-field for tolerance.

Results and Plotting Results

1. On the ‘Home’ toolbar, click ‘Add 2 D Plot Group’.
2. Right click on ‘2D Plot Group 1’ and select ‘Surface’
3. In the ‘Surface Settings’ window, enter ‘c’ in the ‘Expression’ window.
4. Select ‘Solution 1’ from the ‘Data set’.
5. Locate the ‘Coloring’ option, and select ‘Uniform’. In the ‘Color’ option below it, select ‘Black’.
6. Choose the final time step.
7. Click ‘Plot’.

APPENDIX C

HINDERED DIFFUSION STUDIES

This section includes details of the experimental protocol developed in our laboratory by David Chiavetta for studying diffusion of macromolecules in nanopores. Hindered diffusion was studied experimentally by using a stirred diffusion cell. Brilliant Blue FCF dye was used as the solute, and its transport was recorded in real time using UV-Vis spectroscopy. Figure C.1 displays the schematic of the experimental apparatus used for carrying out diffusion experiments. Cell 1 contains a dye solution and cell 2 contains DI water. The solutions in both the half cells are separated by a membrane. Typically track-etched membranes modified using techniques like PVD and pulsed PECVD were used for these experiments. Magnetic stirrers were used to ensure uniform concentrations in each half cell. Due to concentration gradients, dye diffuses through the membrane into cell 2. The absorbance of cell 2 is measured with a UV-vis spectrometer.

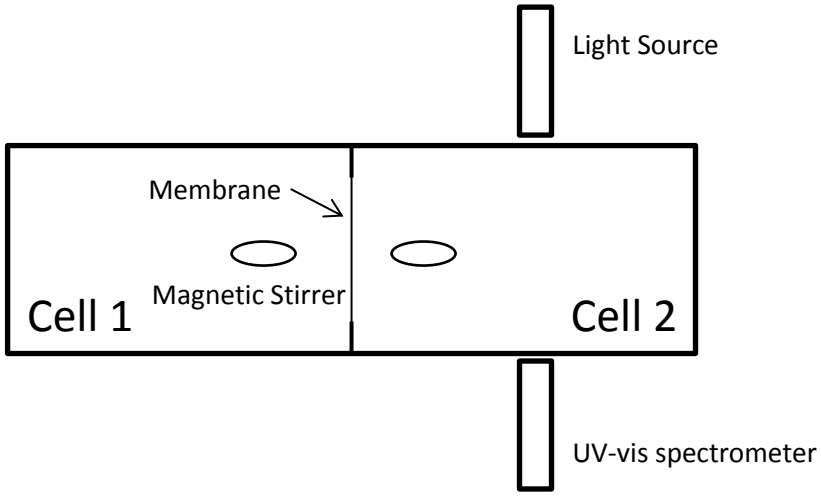


Figure C.1: Schematic of diffusion cell.

The equations below describe the mass transfer process occurring during transport of dye through the pores.

Fick's law governs diffusion in one dimension and is given by Equation C.1:

$$\frac{V}{A_d}\frac{dC}{dt} = D\frac{\partial C}{\partial x}\Big|_{membrane} \qquad \text{(C.1)}$$

where A_d is the cross sectional area through which diffusion occurs, D is the diffusion coefficient, and V is the volume of solution in each half cell. Therefore, the mole balance for each cell is

$$V_1\frac{dC_1}{dt} = -A_d D\frac{\partial C}{\partial x}\Big|_{membrane}; V_2\frac{dC_2}{dt} = A_d D\frac{\partial C}{\partial x}\Big|_{membrane} \qquad \text{(C.2)}$$

and the total mole balance for the system is

$$V_1\frac{dC_1}{dt} + V_2\frac{\partial C_2}{\partial x} = 0 \qquad \text{(C.3)}$$

In this experiment, $V_1 = V_2 = V$. The change in concentration within the membrane is approximated as

$$\frac{dC_1}{dx} \approx \frac{C_2 - C_1}{L_{pore}} \qquad \text{(C.4)}$$

where L_{pore} is the pore length.

D is the hindered diffusion coefficient and determined by two parameters:

$$D = D_\infty h \qquad \text{(C.5)}$$

D_∞ is the bulk diffusion coefficient, i.e. the diffusivity of the solute in bulk solution. h is the hindrance factor. The value of h is unity in bulk solution and goes to zero as the diameter of the solute approaches the diameter of the pore.

D_∞ is calculated from the Stokes-Einstein equation:

$$D_\infty = \frac{kT}{6\pi\mu r_s} \qquad \text{(C.6)}$$

where k is the Boltzmann constant, T is the absolute temperature, μ is the solvent viscosity, and r_s is the Stokes-Einstein radius of a solute molecule. The solute radisu r_s of Brilliant Blue FCF dye was estimated to be 1 nm based on the compound's molecular weight of 793 g/mol.

The hindrance factor, h is calculated using the Renkin equation[78]. The Renkin equation is

$$h = (1-\lambda)^2\left(1 - 2.1044\lambda + 2.089\lambda^3 - 0.948\lambda^5\right) \qquad \text{(C.7)}$$

Where $\lambda = r_s / r_{pore}$ .The hindrance factor depends on the pore geometry, and requires input from the feature scale simulator.

A_d is the area across which diffusion occurs.

$$A_d = n_{pores}A_{pore} = A_{membrane}\phi \qquad \text{(C.8)}$$

where n_{pores} is the number of pores exposed to diffusion and A_{pore} is the cross sectional area of a single pore. Alternatively, A_d can be calculated from $A_{membrane}$, the area of membrane exposed to diffusion, and the membrane porosity ϕ.

The system can therefore be completely described by the following two coupled first order ordinary differential equations:

$$\frac{dC_2}{dt} = \frac{1}{RV}(C_2 - C_1) \qquad \text{(C.9)}$$

$$\frac{dC_1}{dt} = -\frac{dC_2}{dt} \qquad \text{(C.10)}$$

where R is the membrane resistance

$$R = \frac{L_{pore}}{A_{membrane}\phi D_\infty h} \qquad \text{(C.11)}$$

The boundary conditions are C_1 (t=0) = $C_{1,0}$ and C_2 (t=0) = 0. The solution to the system is

$$C_2 = \frac{C_{1,0}}{2}\left(1 - e^{\frac{-2t}{RV}}\right) \qquad \text{(C.12)}$$

$$C_1 = C_{1,0} - C_2 \qquad \text{(C.13)}$$

The membrane resistance or '*R*' values were determined from a hindered diffusion model as well as from diffusion experiments using the following analytical expression:

$$R = \left[\ln\left(\frac{-2C_2}{C_{1,t=0}} + 1\right)\left(\frac{-V}{2t}\right)\right]^{-1} \qquad \text{(C.14)}$$

The hindered diffusion model was built in COMSOL and employed "Transport of Diluted Physics" physics node. The pore geometries were imported into this diffusion model from the feature scale model described earlier.

The experimental membrane resistance was determined by tracking dye concentrations continuously in one of the half cells. The dye employed for investigation of hindered transport can be easily detected using UV-Vis spectroscopy. Figure C.2 shows the absorption spectra for different concentrations of Brilliant Blue FCF dye. The absorption peak for this dye is observed at a wavelength of 628 nm.

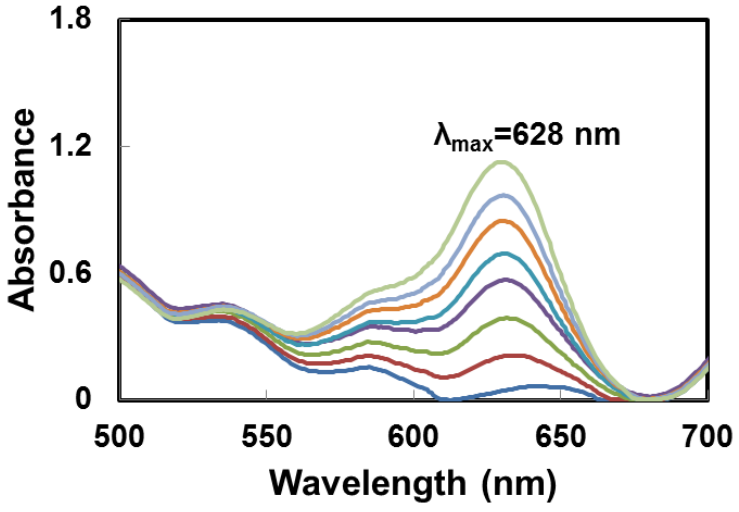


Figure C.2: Absorption spectra for various dye concentrations.

The determination of the dye concentration is based on Beer-Lambert law which implies that the absorbance linearly depends on the analyte concentration. However, when the concentration exceeds a certain value, the absorbance values begin to saturate, and Beer Lambert's law is no longer valid. To find the linear region where Beer Lambert's law is valid, the absorbance at 628 nm was measured for different concentrations of dye in the diffusion cell. The results are shown in Figure C.3.

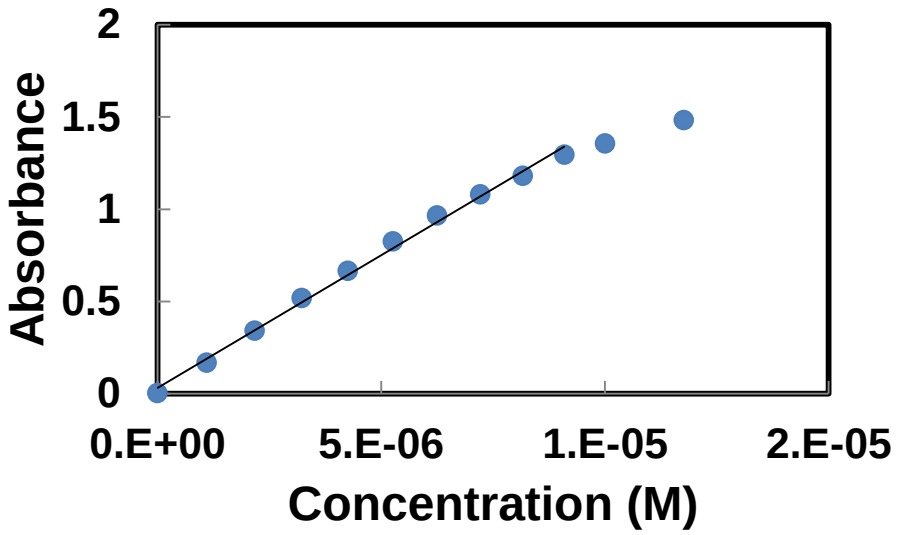


Figure C.3: Plot of absorbance as a function of dye concentration.

APPENDIX D

COPYRIGHT PERMISSIONS

This Appendix includes license agreements granting permission from the copyright holders for reproduction of the material in Chapters 1-6. Written permission from the coauthor to reproduce the work in Chapters 5 and 6 is also included.

AIP PUBLISHING LLC LICENSE TERMS AND CONDITIONS

Aug 29, 2015

All payments must be made in full to CCC. For payment instructions, please see information listed at the bottom of this form.

License Number	3698540820755
Order Date	Aug 29, 2015
Publisher	AIP Publishing LLC
Publication	Journal of Vacuum Science & Technology B
Article Title	Feature scale modeling of pulsed plasma-enhanced chemical vapor deposition
Author	Sanket S. Kelkar,Colin A. Wolden
Online Publication Date	Jul 31, 2014
Volume number	32
Issue number	5
Type of Use	Thesis/Dissertation
Requestor type	Author (original article)
Format	Print and electronic
Portion	Excerpt (> 800 words)
Will you be translating?	No
Title of your thesis / dissertation	DESIGN AND FABRICATION OF ASYMMETRIC NANOPORES USING PULSED PECVD
Expected completion date	Aug 2015
Estimated size (number of pages)	150
Customer Tax ID	USCO
Total	0.00 USD

Terms and Conditions

American Vacuum Society -- Terms and Conditions: Permissions Uses

American Vacuum Society ("AVS") hereby grants to you the non-exclusive right and license to use and/or distribute the Material according to the use specified in your order, on a one-time basis, for the specified term, with a maximum distribution equal to the number that you have ordered. Any links or other content accompanying the Material are not the subject of this license.

1. You agree to include the following copyright and permission notice with the reproduction of the Material:"Reprinted with permission from [FULL CITATION]. Copyright [PUBLICATION YEAR], American Vacuum Society." For an article, the copyright and permission notice must be printed on the first page of the article or book chapter. For photographs, covers, or tables, the copyright and permission notice may appear with the Material, in a footnote, or in the reference list.
2. If you have licensed reuse of a figure, photograph, cover, or table, it is your responsibility to ensure that the material is original to AVS and does not contain the copyright of another entity, and that the copyright notice of the figure, photograph, cover, or table does not indicate that it was reprinted by AVS, with permission, from another source. Under no circumstances does AVS, purport or intend to grant permission to reuse material to which it does not hold copyright.

3. You may not alter or modify the Material in any manner. You may translate the Material into another language only if you have licensed translation rights. You may not use the Material for promotional purposes. AVS reserves all rights not specifically granted herein.
4. The foregoing license shall not take effect unless and until AVS or its agent, Copyright Clearance Center, receives the Payment in accordance with Copyright Clearance Center Billing and Payment Terms and Conditions, which are incorporated herein by reference.
5. AVS or the Copyright Clearance Center may, within two business days of granting this license, revoke the license for any reason whatsoever, with a full refund payable to you. Should you violate the terms of this license at any time, AVS, American Vacuum Society, or Copyright Clearance Center may revoke the license with no refund to you. Notice of such revocation will be made using the contact information provided by you. Failure to receive such notice will not nullify the revocation.
6. AVS makes no representations or warranties with respect to the Material. You agree to indemnify and hold harmless AVS, American Vacuum Society, and their officers, directors, employees or agents from and against any and all claims arising out of your use of the Material other than as specifically authorized herein.
7. The permission granted herein is personal to you and is not transferable or assignable without the prior written permission of AVS. This license may not be amended except in a writing signed by the party to be charged.
8. If purchase orders, acknowledgments or check endorsements are issued on any forms containing terms and conditions which are inconsistent with these provisions, such inconsistent terms and conditions shall be of no force and effect. This document, including the CCC Billing and Payment Terms and Conditions, shall be the entire agreement between the parties relating to the subject matter hereof.

This Agreement shall be governed by and construed in accordance with the laws of the State of New York. Both parties hereby submit to the jurisdiction of the courts of New York County for purposes of resolving any disputes that may arise hereunder.

Questions? customercare@copyright.com or +1-855-239-3415 (toll free in the US) or +1-978-646-2777.

AIP PUBLISHING LLC LICENSE TERMS AND CONDITIONS

Aug 29, 2015

All payments must be made in full to CCC. For payment instructions, please see information listed at the bottom of this form.

License Number	3698540964912
Order Date	Aug 29, 2015
Publisher	AIP Publishing LLC
Publication	Journal of Vacuum Science & Technology B
Article Title	Feature scale modeling of pulsed plasma-enhanced chemical vapor deposition
Author	Sanket S. Kelkar,Colin A. Wolden
Online Publication Date	Jul 31, 2014
Volume number	32
Issue number	5
Type of Use	Thesis/Dissertation
Requestor type	Author (original article)
Format	Print and electronic
Portion	Figure/Table
Number of figures/tables	9
Title of your thesis / dissertation	DESIGN AND FABRICATION OF ASYMMETRIC NANOPORES USING PULSED PECVD
Expected completion date	Aug 2015
Estimated size (number of pages)	150
Customer Tax ID	USCO
Total	0.00 USD

Terms and Conditions

American Vacuum Society -- Terms and Conditions: Permissions Uses

American Vacuum Society ("AVS") hereby grants to you the non-exclusive right and license to use and/or distribute the Material according to the use specified in your order, on a one-time basis, for the specified term, with a maximum distribution equal to the number that you have ordered. Any links or other content accompanying the Material are not the subject of this license.

1. You agree to include the following copyright and permission notice with the reproduction of the Material:"Reprinted with permission from [FULL CITATION]. Copyright [PUBLICATION YEAR], American Vacuum Society." For an article, the copyright and permission notice must be printed on the first page of the article or book chapter. For photographs, covers, or tables, the copyright and permission notice may appear with the Material, in a footnote, or in the reference list.
2. If you have licensed reuse of a figure, photograph, cover, or table, it is your responsibility to ensure that the material is original to AVS and does not contain the copyright of another entity, and that the copyright notice of the figure, photograph, cover, or table does not indicate that it was reprinted by AVS, with permission, from another source. Under no circumstances does AVS, purport or intend to grant permission to reuse material to which it does not hold copyright.

3. You may not alter or modify the Material in any manner. You may translate the Material into another language only if you have licensed translation rights. You may not use the Material for promotional purposes. AVS reserves all rights not specifically granted herein.
4. The foregoing license shall not take effect unless and until AVS or its agent, Copyright Clearance Center, receives the Payment in accordance with Copyright Clearance Center Billing and Payment Terms and Conditions, which are incorporated herein by reference.
5. AVS or the Copyright Clearance Center may, within two business days of granting this license, revoke the license for any reason whatsoever, with a full refund payable to you. Should you violate the terms of this license at any time, AVS, American Vacuum Society, or Copyright Clearance Center may revoke the license with no refund to you. Notice of such revocation will be made using the contact information provided by you. Failure to receive such notice will not nullify the revocation.
6. AVS makes no representations or warranties with respect to the Material. You agree to indemnify and hold harmless AVS, American Vacuum Society, and their officers, directors, employees or agents from and against any and all claims arising out of your use of the Material other than as specifically authorized herein.
7. The permission granted herein is personal to you and is not transferable or assignable without the prior written permission of AVS. This license may not be amended except in a writing signed by the party to be charged.
8. If purchase orders, acknowledgments or check endorsements are issued on any forms containing terms and conditions which are inconsistent with these provisions, such inconsistent terms and conditions shall be of no force and effect. This document, including the CCC Billing and Payment Terms and Conditions, shall be the entire agreement between the parties relating to the subject matter hereof.

This Agreement shall be governed by and construed in accordance with the laws of the State of New York. Both parties hereby submit to the jurisdiction of the courts of New York County for purposes of resolving any disputes that may arise hereunder.

Questions? customercare@copyright.com or +1-855-239-3415 (toll free in the US) or +1-978-646-2777.

ELSEVIER LICENSE
TERMS AND CONDITIONS

Aug 29, 2015

This is a License Agreement between Sanket S Kelkar ("You") and Elsevier ("Elsevier") provided by Copyright Clearance Center ("CCC"). The license consists of your order details, the terms and conditions provided by Elsevier, and the payment terms and conditions.

All payments must be made in full to CCC. For payment instructions, please see information listed at the bottom of this form.

Supplier	Elsevier Limited The Boulevard,Langford Lane Kidlington,Oxford,OX5 1GB,UK
Registered Company Number	1982084
Customer name	Sanket S Kelkar
Customer address	2212, Ford Street GOLDEN, CO 80401
License number	3698470113406
License date	Aug 29, 2015
Licensed content publisher	Elsevier
Licensed content publication	Applied Surface Science
Licensed content title	Formation of octadecyltrichlorosilane (OTS) self-assembled monolayers on amorphous alumina
Licensed content author	Sanket S. Kelkar,David Chiavetta,Colin A. Wolden
Licensed content date	1 October 2013
Licensed content volume number	282
Licensed content issue number	n/a
Number of pages	6
Start Page	291
End Page	296
Type of Use	reuse in a thesis/dissertation
Intended publisher of new work	other
Portion	full article
Format	both print and electronic
Are you the author of this Elsevier article?	Yes
Will you be translating?	No

Title of your thesis/dissertation	DESIGN AND FABRICATION OF ASYMMETRIC NANOPORES USING PULSED PECVD
Expected completion date	Aug 2015
Estimated size (number of pages)	150
Customer Tax ID	USCO
Elsevier VAT number	GB 494 6272 12
Permissions price	0.00 USD
VAT/Local Sales Tax	0.00 USD / 0.00 GBP
Total	0.00 USD
Terms and Conditions	

INTRODUCTION

1. The publisher for this copyrighted material is Elsevier. By clicking "accept" in connection with completing this licensing transaction, you agree that the following terms and conditions apply to this transaction (along with the Billing and Payment terms and conditions established by Copyright Clearance Center, Inc. ("CCC"), at the time that you opened your Rightslink account and that are available at any time at http://myaccount.copyright.com).

GENERAL TERMS

2. Elsevier hereby grants you permission to reproduce the aforementioned material subject to the terms and conditions indicated.

3. Acknowledgement: If any part of the material to be used (for example, figures) has appeared in our publication with credit or acknowledgement to another source, permission must also be sought from that source. If such permission is not obtained then that material may not be included in your publication/copies. Suitable acknowledgement to the source must be made, either as a footnote or in a reference list at the end of your publication, as follows:

"Reprinted from Publication title, Vol /edition number, Author(s), Title of article / title of chapter, Pages No., Copyright (Year), with permission from Elsevier [OR APPLICABLE SOCIETY COPYRIGHT OWNER]." Also Lancet special credit - "Reprinted from The Lancet, Vol. number, Author(s), Title of article, Pages No., Copyright (Year), with permission from Elsevier."

4. Reproduction of this material is confined to the purpose and/or media for which permission is hereby given.

5. Altering/Modifying Material: Not Permitted. However figures and illustrations may be altered/adapted minimally to serve your work. Any other abbreviations, additions, deletions and/or any other alterations shall be made only with prior written authorization of Elsevier Ltd. (Please contact Elsevier at permissions@elsevier.com)

6. If the permission fee for the requested use of our material is waived in this instance, please be advised that your future requests for Elsevier materials may attract a fee.

7. Reservation of Rights: Publisher reserves all rights not specifically granted in the combination of (i) the license details provided by you and accepted in the course of this licensing transaction, (ii) these terms and conditions and (iii) CCC's Billing and Payment terms and conditions.

8. License Contingent Upon Payment: While you may exercise the rights licensed immediately upon issuance of the license at the end of the licensing process for the transaction, provided that you have disclosed complete and accurate details of your proposed use, no license is finally effective unless and until full payment is received from you (either by publisher or by CCC) as provided in CCC's Billing and Payment terms and conditions. If full payment is not received on a timely basis, then any license preliminarily granted shall be deemed automatically revoked and shall be void as if never granted. Further, in the event that you breach any of these terms and conditions or any of CCC's Billing and Payment terms and conditions, the license is automatically revoked and shall be void as if never granted. Use of materials as described in a revoked license, as well as any use of the materials beyond the scope of an unrevoked license, may constitute copyright infringement and publisher reserves the right to take any and all action to protect its copyright in the materials.

9. Warranties: Publisher makes no representations or warranties with respect to the licensed material.

10. Indemnity: You hereby indemnify and agree to hold harmless publisher and CCC, and their respective officers, directors, employees and agents, from and against any and all claims arising out of your use of the licensed material other than as specifically authorized pursuant to this license.

11. No Transfer of License: This license is personal to you and may not be sublicensed, assigned, or transferred by you to any other person without publisher's written permission.

12. No Amendment Except in Writing: This license may not be amended except in a writing signed by both parties (or, in the case of publisher, by CCC on publisher's behalf).

13. Objection to Contrary Terms: Publisher hereby objects to any terms contained in any purchase order, acknowledgment, check endorsement or other writing prepared by you, which terms are inconsistent with these terms and conditions or CCC's Billing and Payment terms and conditions. These terms and conditions, together with CCC's Billing and Payment terms and conditions (which are incorporated herein), comprise the entire agreement between you and publisher (and CCC) concerning this licensing transaction. In the event of any conflict between your obligations established by these terms and conditions and those established by CCC's Billing and Payment terms and conditions, these terms and conditions shall control.

14. Revocation: Elsevier or Copyright Clearance Center may deny the permissions described in this License at their sole discretion, for any reason or no reason, with a full refund payable to you. Notice of such denial will be made using the contact information provided by you. Failure to receive such notice will not alter or invalidate the denial. In no event will Elsevier or Copyright Clearance Center be responsible or liable for any costs, expenses or damage incurred by you as a result of a denial of your permission request, other than a refund of the amount(s) paid by you to Elsevier and/or Copyright Clearance Center for denied permissions.

LIMITED LICENSE

The following terms and conditions apply only to specific license types:

15. **Translation**: This permission is granted for non-exclusive world **English** rights only unless your license was granted for translation rights. If you licensed translation rights you may only translate this content into the languages you requested. A professional translator must perform all translations and reproduce the content word for word preserving the integrity of the article. If this license is to re-use 1 or 2 figures then permission is granted for non-exclusive world rights in all languages.

16. **Posting licensed content on any Website**: The following terms and conditions apply as follows: Licensing material from an Elsevier journal: All content posted to the web site must maintain the copyright information line on the bottom of each image; A hyper-text must be included to the Homepage of the journal from which you are licensing at http://www.sciencedirect.com/science/journal/xxxxx or the Elsevier homepage for books at http://www.elsevier.com; Central Storage: This license does not include permission for a scanned version of the material to be stored in a central repository such as that provided by Heron/XanEdu.

Licensing material from an Elsevier book: A hyper-text link must be included to the Elsevier homepage at http://www.elsevier.com . All content posted to the web site must maintain the copyright information line on the bottom of each image.

Posting licensed content on Electronic reserve: In addition to the above the following clauses are applicable: The web site must be password-protected and made available only to bona fide students registered on a relevant course. This permission is granted for 1 year only. You may obtain a new license for future website posting.

17. **For journal authors:** the following clauses are applicable in addition to the above:

Preprints:

A preprint is an author's own write-up of research results and analysis, it has not been peer-reviewed, nor has it had any other value added to it by a publisher (such as formatting, copyright, technical enhancement etc.).

Authors can share their preprints anywhere at any time. Preprints should not be added to or enhanced in any way in order to appear more like, or to substitute for, the final versions of articles however authors can update their preprints on arXiv or RePEc with their Accepted Author Manuscript (see below).

If accepted for publication, we encourage authors to link from the preprint to their formal publication via its DOI. Millions of researchers have access to the formal publications on ScienceDirect, and so links will help users to find, access, cite and use the best available version. Please note that Cell Press, The Lancet and some society-owned have different preprint policies. Information on these policies is available on the journal homepage.

Accepted Author Manuscripts: An accepted author manuscript is the manuscript of an article that has been accepted for publication and which typically includes author-incorporated changes suggested during submission, peer review and editor-author

communications.

Authors can share their accepted author manuscript:

- immediately
  - via their non-commercial person homepage or blog
  - by updating a preprint in arXiv or RePEc with the accepted manuscript
  - via their research institute or institutional repository for internal institutional uses or as part of an invitation-only research collaboration work-group
  - directly by providing copies to their students or to research collaborators for their personal use
  - for private scholarly sharing as part of an invitation-only work group on commercial sites with which Elsevier has an agreement
- after the embargo period
  - via non-commercial hosting platforms such as their institutional repository
  - via commercial sites with which Elsevier has an agreement

In all cases accepted manuscripts should:

- link to the formal publication via its DOI
- bear a CC-BY-NC-ND license - this is easy to do
- if aggregated with other manuscripts, for example in a repository or other site, be shared in alignment with our hosting policy not be added to or enhanced in any way to appear more like, or to substitute for, the published journal article.

Published journal article (JPA): A published journal article (PJA) is the definitive final record of published research that appears or will appear in the journal and embodies all value-adding publishing activities including peer review co-ordination, copy-editing, formatting, (if relevant) pagination and online enrichment.

Policies for sharing publishing journal articles differ for subscription and gold open access articles:

Subscription Articles: If you are an author, please share a link to your article rather than the full-text. Millions of researchers have access to the formal publications on ScienceDirect, and so links will help your users to find, access, cite, and use the best available version.

Theses and dissertations which contain embedded PJAs as part of the formal submission can be posted publicly by the awarding institution with DOI links back to the formal publications on ScienceDirect.

If you are affiliated with a library that subscribes to ScienceDirect you have additional

private sharing rights for others' research accessed under that agreement. This includes use for classroom teaching and internal training at the institution (including use in course packs and courseware programs), and inclusion of the article for grant funding purposes.

Gold Open Access Articles: May be shared according to the author-selected end-user license and should contain a CrossMark logo, the end user license, and a DOI link to the formal publication on ScienceDirect.

Please refer to Elsevier's posting policy for further information.

18. **For book authors** the following clauses are applicable in addition to the above: Authors are permitted to place a brief summary of their work online only. You are not allowed to download and post the published electronic version of your chapter, nor may you scan the printed edition to create an electronic version. **Posting to a repository:** Authors are permitted to post a summary of their chapter only in their institution's repository.

19. **Thesis/Dissertation**: If your license is for use in a thesis/dissertation your thesis may be submitted to your institution in either print or electronic form. Should your thesis be published commercially, please reapply for permission. These requirements include permission for the Library and Archives of Canada to supply single copies, on demand, of the complete thesis and include permission for Proquest/UMI to supply single copies, on demand, of the complete thesis. Should your thesis be published commercially, please reapply for permission. Theses and dissertations which contain embedded PJAs as part of the formal submission can be posted publicly by the awarding institution with DOI links back to the formal publications on ScienceDirect.

Elsevier Open Access Terms and Conditions

You can publish open access with Elsevier in hundreds of open access journals or in nearly 2000 established subscription journals that support open access publishing. Permitted third party re-use of these open access articles is defined by the author's choice of Creative Commons user license. See our open access license policy for more information.

Terms & Conditions applicable to all Open Access articles published with Elsevier:

Any reuse of the article must not represent the author as endorsing the adaptation of the article nor should the article be modified in such a way as to damage the author's honour or reputation. If any changes have been made, such changes must be clearly indicated.

The author(s) must be appropriately credited and we ask that you include the end user license and a DOI link to the formal publication on ScienceDirect.

If any part of the material to be used (for example, figures) has appeared in our publication with credit or acknowledgement to another source it is the responsibility of the user to ensure their reuse complies with the terms and conditions determined by the rights holder.

Additional Terms & Conditions applicable to each Creative Commons user license:

CC BY: The CC-BY license allows users to copy, to create extracts, abstracts and new works from the Article, to alter and revise the Article and to make commercial use of the

Article (including reuse and/or resale of the Article by commercial entities), provided the user gives appropriate credit (with a link to the formal publication through the relevant DOI), provides a link to the license, indicates if changes were made and the licensor is not represented as endorsing the use made of the work. The full details of the license are available at http://creativecommons.org/licenses/by/4.0.

CC BY NC SA: The CC BY-NC-SA license allows users to copy, to create extracts, abstracts and new works from the Article, to alter and revise the Article, provided this is not done for commercial purposes, and that the user gives appropriate credit (with a link to the formal publication through the relevant DOI), provides a link to the license, indicates if changes were made and the licensor is not represented as endorsing the use made of the work. Further, any new works must be made available on the same conditions. The full details of the license are available at http://creativecommons.org/licenses/by-nc-sa/4.0.

CC BY NC ND: The CC BY-NC-ND license allows users to copy and distribute the Article, provided this is not done for commercial purposes and further does not permit distribution of the Article if it is changed or edited in any way, and provided the user gives appropriate credit (with a link to the formal publication through the relevant DOI), provides a link to the license, and that the licensor is not represented as endorsing the use made of the work. The full details of the license are available at http://creativecommons.org/licenses/by-nc-nd/4.0. Any commercial reuse of Open Access articles published with a CC BY NC SA or CC BY NC ND license requires permission from Elsevier and will be subject to a fee.

Commercial reuse includes:

- Associating advertising with the full text of the Article
- Charging fees for document delivery or access
- Article aggregation
- Systematic distribution via e-mail lists or share buttons

Posting or linking by commercial companies for use by customers of those companies.

20. **Other Conditions**:

v1.7

Questions? customercare@copyright.com or +1-855-239-3415 (toll free in the US) or +1-978-646-2777.

Gmail by Google

Sanket Kelkar <sanketskelkar@gmail.com>

Request for permission to reproduce manuscripts in thesis

David Chiavetta <dchiavetta@gmail.com> Tue, Sep 1, 2015 at 10:09 AM
To: Sanket Kelkar <sanketskelkar@gmail.com>

Hi Sanket,

I hereby permit you (Sanket Kelkar) to reproduce the following works as part of your thesis:

" Formation of octadecyltrichlorosilane (OTS) self-assembled monolayers on amorphous alumina" published in the Journal of Applied Surface Science, (2013), 282, 291-296 as part of your thesis.

"Design and Evaluation of Vapor Deposition Techniques for Pore Size Modification" under preparation.

Regards,

David Chiavetta
dchiavetta@gmail.com

NATURE PUBLISHING GROUP LICENSE TERMS AND CONDITIONS

Sep 08, 2015

This is a License Agreement between Sanket S Kelkar ("You") and Nature Publishing Group ("Nature Publishing Group") provided by Copyright Clearance Center ("CCC"). The license consists of your order details, the terms and conditions provided by Nature Publishing Group, and the payment terms and conditions.

All payments must be made in full to CCC. For payment instructions, please see information listed at the bottom of this form.

License Number	3700411363259
License date	Sep 01, 2015
Licensed content publisher	Nature Publishing Group
Licensed content publication	Nature Nanotechnology
Licensed content title	Nanopore sensors for nucleic acid analysis
Licensed content author	Bala Murali Venkatesan, Rashid Bashir
Licensed content date	Sep 18, 2011
Volume number	6
Issue number	10
Type of Use	reuse in a dissertation / thesis
Requestor type	academic/educational
Format	print and electronic
Portion	figures/tables/illustrations
Number of figures/tables/illustrations	1
High-res required	no
Figures	2
Author of this NPG article	no
Your reference number	None
Title of your thesis / dissertation	DESIGN AND FABRICATION OF ASYMMETRIC NANOPORES USING PULSED PECVD
Expected completion date	Sep 2015
Estimated size (number of pages)	150
Customer Tax ID	USCO
Total	0.00 USD
Terms and Conditions	

Terms and Conditions for Permissions

NATURE PUBLISHING GROUP LICENSE TERMS AND CONDITIONS

Sep 08, 2015

This is a License Agreement between Sanket S Kelkar ("You") and Nature Publishing Group ("Nature Publishing Group") provided by Copyright Clearance Center ("CCC"). The license consists of your order details, the terms and conditions provided by Nature Publishing Group, and the payment terms and conditions.

All payments must be made in full to CCC. For payment instructions, please see information listed at the bottom of this form.

License Number	3700540204780
License date	Sep 01, 2015
Licensed content publisher	Nature Publishing Group
Licensed content publication	Nature
Licensed content title	Ion-beam sculpting at nanometre length scales
Licensed content author	Jiali Li, Derek Stein, Ciaran McMullan, Daniel Branton, Michael J. Aziz et al.
Licensed content date	Jul 12, 2001
Volume number	412
Issue number	6843
Type of Use	reuse in a dissertation / thesis
Requestor type	academic/educational
Format	print and electronic
Portion	figures/tables/illustrations
Number of figures/tables/illustrations	2
Figures	1,2
Author of this NPG article	no
Your reference number	None
Title of your thesis / dissertation	DESIGN AND FABRICATION OF ASYMMETRIC NANOPORES USING PULSED PECVD
Expected completion date	Sep 2015
Estimated size (number of pages)	150
Customer Tax ID	USCO
Total	0.00 USD
Terms and Conditions	

Terms and Conditions for Permissions



RightsLink®

Home | Create Account | Help | Live Chat



Title: Ionic Field Effect Transistors with Sub-10 nm Multiple Nanopores
Author: Sung-Wook Nam, Michael J. Rooks, Ki-Bum Kim, et al
Publication: Nano Letters
Publisher: American Chemical Society
Date: May 1, 2009

Copyright © 2009, American Chemical Society

LOGIN

If you're a copyright.com user, you can login to RightsLink using your copyright.com credentials. Already a RightsLink user or want to learn more?

PERMISSION/LICENSE IS GRANTED FOR YOUR ORDER AT NO CHARGE

This type of permission/license, instead of the standard Terms & Conditions, is sent to you because no fee is being charged for your order. Please note the following:

- Permission is granted for your request in both print and electronic formats, and translations.
- If figures and/or tables were requested, they may be adapted or used in part.
- Please print this page for your records and send a copy of it to your publisher/graduate school.
- Appropriate credit for the requested material should be given as follows: "Reprinted (adapted) with permission from (COMPLETE REFERENCE CITATION). Copyright (YEAR) American Chemical Society." Insert appropriate information in place of the capitalized words.
- One-time permission is granted only for the use specified in your request. No additional uses are granted (such as derivative works or other editions). For any other uses, please submit a new request.

If credit is given to another source for the material you requested, permission must be obtained from that source.

BACK | CLOSE WINDOW

Copyright © 2015 Copyright Clearance Center, Inc. All Rights Reserved. Privacy statement. Terms and Conditions.
Comments? We would like to hear from you. E-mail us at customercare@copyright.com

JOHN WILEY AND SONS LICENSE TERMS AND CONDITIONS

Sep 08, 2015

This Agreement between Sanket S Kelkar ("You") and John Wiley and Sons ("John Wiley and Sons") consists of your license details and the terms and conditions provided by John Wiley and Sons and Copyright Clearance Center.

License Number	3704111402368
License date	Sep 08, 2015
Licensed Content Publisher	John Wiley and Sons
Licensed Content Publication	Angewandte Chemie International Edition
Licensed Content Title	Atomic Layer Deposition Chemistry: Recent Developments and Future Challenges
Licensed Content Author	Markku Leskelä,Mikko Ritala
Licensed Content Date	Nov 18, 2003
Pages	7
Type of use	Dissertation/Thesis
Requestor type	University/Academic
Format	Print and electronic
Portion	Figure/table
Number of figures/tables	1
Original Wiley figure/table number(s)	Figure 1
Will you be translating?	No
Title of your thesis / dissertation	DESIGN AND FABRICATION OF ASYMMETRIC NANOPORES USING PULSED PECVD
Expected completion date	Sep 2015
Expected size (number of pages)	150
Requestor Location	Sanket S Kelkar 2212, Ford Street Apt # 17 GOLDEN, CO 80401 United States Attn: Sanket S Kelkar
Billing Type	Invoice
Billing Address	Sanket S Kelkar 2212, Ford Street Apt # 17 GOLDEN, CO 80401

AIP PUBLISHING LLC LICENSE TERMS AND CONDITIONS

Sep 08, 2015

All payments must be made in full to CCC. For payment instructions, please see information listed at the bottom of this form.

License Number	3700420221502
Order Date	Sep 01, 2015
Publisher	AIP Publishing LLC
Publication	Journal of Vacuum Science & Technology A
Article Title	Enhancement of metal oxide deposition rate and quality using pulsed plasma-enhanced chemical vapor deposition at low frequency
Author	Michael T. Seman,David N. Richards,Pieter C. Rowlette, et al.
Online Publication Date	Aug 6, 2008
Volume number	26
Issue number	5
Type of Use	Thesis/Dissertation
Requestor type	Student
Format	Print and electronic
Portion	Figure/Table
Number of figures/tables	1
Title of your thesis / dissertation	DESIGN AND FABRICATION OF ASYMMETRIC NANOPORES USING PULSED PECVD
Expected completion date	Sep 2015
Estimated size (number of pages)	150
Customer Tax ID	USCO
Total	0.00 USD

Terms and Conditions

American Vacuum Society -- Terms and Conditions: Permissions Uses

American Vacuum Society ("AVS") hereby grants to you the non-exclusive right and license to use and/or distribute the Material according to the use specified in your order, on a one-time basis, for the specified term, with a maximum distribution equal to the number that you have ordered. Any links or other content accompanying the Material are not the subject of this license.

1. You agree to include the following copyright and permission notice with the reproduction of the Material:"Reprinted with permission from [FULL CITATION]. Copyright [PUBLICATION YEAR], American Vacuum Society." For an article, the copyright and permission notice must be printed on the first page of the article or book chapter. For photographs, covers, or tables, the copyright and permission notice may appear with the Material, in a footnote, or in the reference list.
2. If you have licensed reuse of a figure, photograph, cover, or table, it is your responsibility to ensure that the material is original to AVS and does not contain the copyright of another entity, and that the copyright notice of the figure, photograph, cover, or table does not indicate that it was reprinted by AVS, with permission, from another source. Under no circumstances does AVS, purport or intend to grant permission to reuse material to which it does not hold copyright.

Copyright Clearance Center RightsLink®

Home | Create Account | Help | Live Chat

ACS Publications
Most Trusted. Most Cited. Most Read.

Title: Contact Angle Measurements Using a Simplified Experimental Setup
Author: Guillaume Lamour, Ahmed Hamraoui, Andrii Buvailo, et al
Publication: Journal of Chemical Education
Publisher: American Chemical Society
Date: Dec 1, 2010
Copyright © 2010, American Chemical Society

LOGIN
If you're a copyright.com user, you can login to RightsLink using your copyright.com credentials. Already a RightsLink user or want to learn more?

PERMISSION/LICENSE IS GRANTED FOR YOUR ORDER AT NO CHARGE

This type of permission/license, instead of the standard Terms & Conditions, is sent to you because no fee is being charged for your order. Please note the following:

- Permission is granted for your request in both print and electronic formats, and translations.
- If figures and/or tables were requested, they may be adapted or used in part.
- Please print this page for your records and send a copy of it to your publisher/graduate school.
- Appropriate credit for the requested material should be given as follows: "Reprinted (adapted) with permission from (COMPLETE REFERENCE CITATION). Copyright (YEAR) American Chemical Society." Insert appropriate information in place of the capitalized words.
- One-time permission is granted only for the use specified in your request. No additional uses are granted (such as derivative works or other editions). For any other uses, please submit a new request.

If credit is given to another source for the material you requested, permission must be obtained from that source.

JOHN WILEY AND SONS LICENSE TERMS AND CONDITIONS

Sep 08, 2015

This Agreement between Sanket S Kelkar ("You") and John Wiley and Sons ("John Wiley and Sons") consists of your license details and the terms and conditions provided by John Wiley and Sons and Copyright Clearance Center.

License Number	3700430598783
License date	Sep 01, 2015
Licensed Content Publisher	John Wiley and Sons
Licensed Content Publication	Advanced Functional Materials
Licensed Content Title	Ion-Current Rectification in Nanopores and Nanotubes with Broken Symmetry
Licensed Content Author	Z.S. Siwy
Licensed Content Date	Mar 6, 2006
Pages	12
Type of use	Dissertation/Thesis
Requestor type	University/Academic
Format	Print and electronic
Portion	Abstract
Will you be translating?	No
Title of your thesis / dissertation	DESIGN AND FABRICATION OF ASYMMETRIC NANOPORES USING PULSED PECVD
Expected completion date	Sep 2015
Expected size (number of pages)	150
Requestor Location	Sanket S Kelkar 2212, Ford Street Apt # 17 GOLDEN, CO 80401 United States Attn: Sanket S Kelkar
Billing Type	Invoice
Billing Address	Sanket S Kelkar 2212, Ford Street Apt # 17 GOLDEN, CO 80401 United States Attn: Sanket S Kelkar
Total	0.00 USD